Periodic Segmented Waveguides in $Ti:LiNbO_3$

A Thesis Submited to the Faculty of Engineering of the University of Glasgow for the Degree of Doctor of Philosophy.

by

Daniel Ortega González

To those I love

Acknowledgements.

I would like to thank every one who made this work possible; those who worked with me and those who encouraged me outside the department.

I would like to thank my mother and grandmother for their continued support, and my friends for their understanding during the conception of this work. I would especially like to thank Sharon, Ryan, Mike, and my brother Javier, now living in Glasgow.

I would like to thank Stewart Aitchison for his supervision, for giving me the opportunity to work within a fine team and for providing me with friendship which went beyond the call of duty.

I would like to thank all the people in the department who contributed to this work. Richard De La Rue, Dave Hutchings, J. Arnold who all enlightened me in various aspects of integrated optics; Carlos Trevino-Palacios at CREOL in Central Florida who generated all the experimental results for second harmonic generation and with whom I had the pleasure to have virtual collaboration; Enrique Acha, Claudio Fuerte, Jesus Rico with whom I spent many hours writing the code for my programs; Mike Street, Neil Whitebread with whom I learned and discussed many aspects of nonlinear optics; Jose Aldariz who helped me to develop the BPM software; Andy McLaughlin, Fernando Camacho, Paulo Marques, Carolyn Mcewan, and Valentin Loyo, with whom I share my office and had many interesting conversations; Pablo Loza and Gordon Kennedy at St. Andrews, who provided me with outstanding laser light; Jim Bonar, Andy, Paulo, Jesus, Marcus from the Planar silica group with whom I now work; Kas Piechowiak for polishing and cutting the $LiNbO_3$ samples. I would also like to thank all the people in the clean room, furnace room, mechanical workshop and evaporating lab (Ian McNicholl, Lois Hobbs, Doogie Irons, Helen, Margaret, Joan ...), and all the people who provide us with the opportunity to carry out research in a fine institution. I am certain there are many people I have left out, I apologise to them and thank them all.

I would like to thank the Faculty of Engineering for the support of this work.

Contents.

Abstract

This aim of this thesis is to study the propagation of light in Periodic Segemented Waveguides (PSWs). The work focused on three main areas:

- Assessment of the accuracy of representing a PSW with an equivalent continuous waveguide, where the cut-off wavelength is a function of the PSW duty cycle. Experimental verification of the accuracy of this statement is reported, for the first time, through the fabrication and testing of Ti:$LiNbO_3$ PSWs. This is acheived by studying the cut-off wavelength of PSWs.

  Due to asymmetry, Ti:$LiNbO_3$ waveguides experience cut-off. This presents a problem in the fabrication of PSWs, where as a consequence of the segmentation, there is a reduction in the refractive index difference which reduces the cut-off wavelength. Due to the birefringence of the material the cut-off wavelength is different for the ordinary ray and the extraordinary ray. A model has been developed to obtain the cut-off wavelength as a function of the duty-cycle, as an aid to the fabrication of PSWs.

- The equivalent continuous waveguide model can describe some of the properties of PSWs, but does not account for the losses associated with the segmentation. For the first time light propagation in a PSW has been demonstrated using a 3D finite difference beam propagation method (3D FD BPM). The software has been specifically developed to study PSWs. This provides the possibility of observing the field distribution as it propagates over one period, and illustrates the segmentation losses in the waveguide. Careful control of the optical field at the edges of the computational window (to minimise errors) allowed an assessment of the radiation loss for different periods and duty-cycles. Previously published work only investigated the segmentation losses for 2D structures, with radiation towards the substrate only. We compared the mode size of PSWs and its equivalent continuous waveguide. The agreement between the two sets of results confirmed that the model can be used to describe PSWs, and indicated that the 3D BPM accurately simulates PSWs.

- Examination of the PSWs interaction in phase matching processes. In this thesis, PSWs were fabricated, and using the second order nonlinear properties of $LiNbO_3$, the linear propagation of PSWs were studied. In grating assisted coupling any difference between the propagation constants is compensated by the period. Grating assisted coupling with PSWs is not new, as it has been used previously in SHG, but at present the behaviour of the propagation constant as the PSW quasi-mode propagates is not evident. Some authors propose a change in the propagation constant as the wave progresses through areas with different indices. But no evidence of this has been found in this work or the literature. In this thesis the fabrication of chirped PSWs and the tuning curves for SHG are reported. All the software used to simulate SHG has been developed to take into consideration the dispersion of the material and some of the limitations imposed by fabrication.

Preface

$LiNbO_3$ is a well established material in the field of integrated optics, it possesses a very useful combination of properties and characteristics. In Chapter 2 we discuss some of the aspects of bulk $LiNbO_3$ and Ti:$LiNbO_3$ waveguides relevant to this thesis, in particular the birefringe, transmission and non-linear optical properties as well as the material changes which take place during the fabrication of the waveguides by Ti indiffusion. During the last 25 years a variety of active and passive integrated, high performance devices have been fabricated in $LiNbO_3$. Here we propose the use of periodic segmented waveguides (PSWs) to increase the functionality of integrated components. The use of PSWs can be extended to any material system, and such devices have been reported in $LiNbO_3$, KTP , InP , and glass. Initially, PSWs were used as Bragg-gratings and subsequently to obtain quasi-phase matching (QPM) second harmonic generation (SHG). Recently PSWs have been employed in asymmetric Y-junction wavelength demultiplexers, asymmetric couples wavelength filters and in tapers.

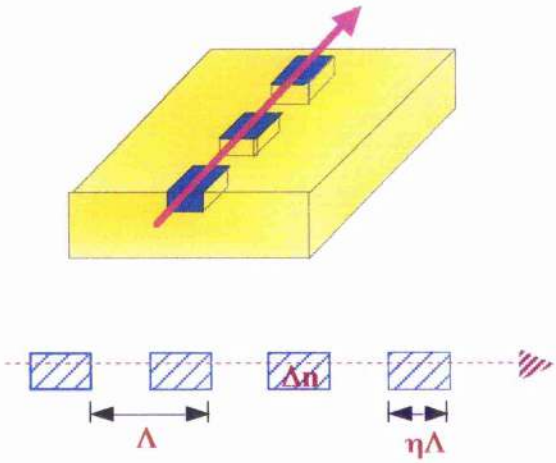

Fig 1. Index distribution of a PSW, where Λ is the period and η the duty-cycle.

In a PSW the increase in the refractive index (Δn) is modulated periodically during fabrication, this is shown schematically in Fig 1. As a consequence of the segmentation, the loss in the guide is increased and the effective refractive index is reduced when compared to a continuous waveguide. The application of PSWs in integrated optics rely on the possibility of controlling the effective index with the duty-cycle, and at the same time uses its period for phase matching applications. The combination of both opens the gates to a range of novel devices.

The aim of this thesis is to investigate the propagation of light in PSWs, in particular three points were of interest:

- Exploration of the accuracy of representing a PSW by an equivalent continuous waveguide and obtaining the cut-off wavelength as a function of the duty-cycle. A PSW can be represented by an equivalent continuous waveguide with the same depth and width, in which the average index difference, $\Delta n'$, is taken to be the weighted average of the index along the direction of propagation. In the case of step index waveguides this is represented by Eq. 1 .

$$\Delta n' = \eta \Delta n \qquad \text{Eq 1}$$

until now, there have not been any reported experimental results which show the accuracy of this statement. Therefore we dedicate Chapter 3 to describing the fabrication of PSWs and to show that they can be accurately described by Eq 1. To do this we studied the cut-off wavelength of PSWs.

Due to asymmetry, Ti:$LiNbO_3$ waveguides experience cut-off, i.e. above a certain wavelength the waveguide will not guide any light. This presents a problem in the fabrication of PSWs, as the reduction in refractive index difference as a consequence of the segmentation, reduces the cut-off wavelength, and due to the birefringe of the material, the cut-off wavelength is different for the ordinary ray and the extraordinary ray. In Chapter 3 a model has been developed to obtain the cut-off wavelength as a function of the duty-cycle and therefore aid us in the fabrication of PSWs. The cut-off wavelength is dependent on the increase of the refractive index, therefore Eq 1 could be implemented directly in our model, and the comparison of the experimental and theoretical results provides us with a direct method to prove the validity of Eq 1.

- The model described by Eq 1 can describe some of the properties of PSWs, but does not account for the losses associated with the segmentation. For the first time light propagation in a PSW has been demonstrated. In Chapter 4, using a 3D finite difference beam propagation method (3D FD BPM), we generated the optical field guided by a PSW. The software has been specifically developed to study PSWs. This provided us with the possibility of observing the field distributions as it propagates over one period, and shows the segmentation losses (the losses associated with the modulation of the refractive index) in the waveguide. Careful control of the optical field at the edges of the computational window (to minimise noise) permitted us to quantify the radiation losses for different periods and duty-cycles. Previous work only investigated the segmentation losses for 2D structures, with radiation towards

the substrate only. We compared the mode size of PSWs and its equivalent continuous waveguide. The agreement between the two sets of results confirms that Eq 1 can be used to describe PSWs, and indicates that the 3D BPM accurately simulates PSWs.

- To show that PSWs interact in phase matching processes in exactly the same way as continuous waveguides. In Chapter 5, PSWs were fabricated, and using the second order nonlinear properties of $LiNbO_3$, the linear propagation of PSWs were studied. Coupling between two modes takes place if a coupling coefficient exists, and the propagation constant of the two modes is the same. In grating assisted coupling any difference between the propagation constants is compensated by the period. Grating assisting coupling using PSWs is not new, it has been used in SHG, but at present the behaviour of the propagation constant as the PSW quasi-mode propagates is not evident. Some authors propose a change in the propagation constant as the wave progresses through areas with different indices. But no evidence of this has been found in our work or has been reported in the literature. In this thesis the fabrication of chirped PSWs and the tuning curves for SHG is reported. All the software used to simulate SHG has been developed to take into consideration the dispersion of the material and some of the limitations imposed by fabrication.

1

Introduction

1.1 Material system.

Lithium Niobate ($LiNbO_3$) is one of the most attractive materials for integrated optics. It allows the fabrication of low loss planar and channel waveguides by titanium indiffusion and proton exchange. A schematic illustration of a typical waveguide in $LiNbO_3$ is shown in Fig 1.1. In addition $LiNbO_3$ possesses a useful combination of properties and characteristics [1]:

- Ferroelectric with high Curie point (1120 °C).
- Moderately large nonlinear optical coefficient: $d_{33} \approx 30$ pm/v, $d_{33}^2 / \left(n_\omega^2 n_{2\omega}\right) \approx 102\ pm^2/v^2$
- Large birefringence: At $\lambda = 1.6\ \mu m$, $n_o = 2.1372$ $n_e = 2.2138$
- Large electro-optic effect: $r_{33} \approx 30$ pm/v, $r_{33} n^3 \approx 306$ pm/v
- Strong piezoelectric effect
- Excellent acoustic properties.
- Photoelastic effect

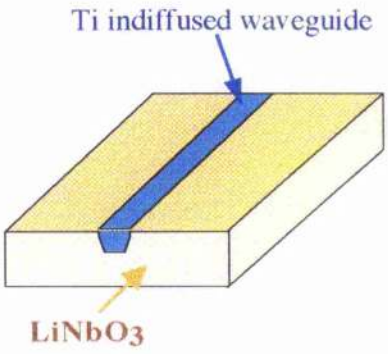

Fig. 1.1. Ti:$LiNbO_3$ waveguide

The electro-optic, photoelastic and piezoelectric properties have been used over the last 25 years to develop of a large variety of active integrated optical devices with high performance. Such components allow the control of phase, amplitude, polarisation and direction of propagation of light, generally with moderately low drive power levels and high bandwidth. Higher drive powers are required to operate at high frequencies. Active devices such as electro-optical and acousto-optical devices (modulators, polarisation converters, polarisation scrambler, beam deflectors, switches, tuneable wavelength filters, etc.....) have been combined with passive devices such as lenses, polarisers, polarisation splitters, directional couplers, beam splitters, Bragg reflector gratings, wavelength filter/multiplexer, etc...., on a common $LiNbO_3$ substrate to form integrated optical circuits for signal-processing

applications [2]. They are used in fibre-optical communication [3, 4, 5, 6] and sensor systems [7].

Over the last 10 years, there has been a growing interest in rare-earth doped optically pumped amplifiers and laser devices in $LiNbO_3$ (Er in particular) [3]. The combination of the amplifying properties of erbium with the excellent electro-optical and acousto-optical properties, allows the development of a whole new class of waveguide devices with higher functionality [3]. The large nonlinear coefficient together with its broad transmission spectrum (from 0.4 to 5 μm) makes $LiNbO_3$ a very attractive material in the fabrication of optical parametric oscillators (OPOs) [8]. The nonlinear properties of $LiNbO_3$ have also been used for blue light generation [9, 10, 11] and all optical switching [12][13].

Discussing the possibilities of $LiNbO_3$ in integrated optics W. Sohler, recently at ECIO'97 (8th European conference on integrated optics) in Stockholm said:

> *"During the last few years several new $LiNbO_3$-specific processing technologies have been developed: periodic poling of ferroelectric microdomains, diffusion-doping with rare-earth ions, laser ablation and photorefractive grating fabrication, selective chemical and ion-beam surface etching, and acoustic waveguide definition by Ti-indiffusion. These technologies made possible the development of a variety of new integrated optical devices of high performance. Examples are parametric frequency converters of high efficiency, optical amplifiers and modelocked, tunable and narrow-linewidth lasers, ultrahigh bandwidth electrooptical modulators, and tailored acoustooptical filters, multiplexers and switches. Together with the more conventional devices they form the building blocks of a future monolithic integrated optics in $LiNbO_3$. It is a great challenge to develop complex application specific optical circuits (ASOCs) for optical communications, instrumentation and sensing."*

For applications such as high-speed electrooptic intensity modulators [14], fast electro-optic polarisation scramblers [4][5] and as parametric frequency converters in OPOs [8] $LiNbO_3$ is one of the most attractive materials.

1.2. Periodically segmented waveguides (PSW).

To date, periodic segmented waveguides (see Fig 1.2) have been reported in a number of different material systems including proton-exchanged $LiNbO_3$ [15], KTP [16, 17, 18], InP [19], annealed proton-exchanged (APE)-$LiNbO_3$ [20, 21, 22] and Ti:$LiNbO_3$ [23, 24, 25]. Initially, PSWs were used in Bragg-grating structures [15] and subsequently to obtain quasi-phase matched (QPM) second harmonic generation (SHG) [16, 17, 18, 22]. Recently, PSWs have been employed in asymmetric Y-junction wavelength demultiplexers [25], asymmetric couplers [26, 27] and in tapers to match the mode of the input source to the desired mode of the structure [19, 20, 28], and therefore to maximise the coupling efficiency.

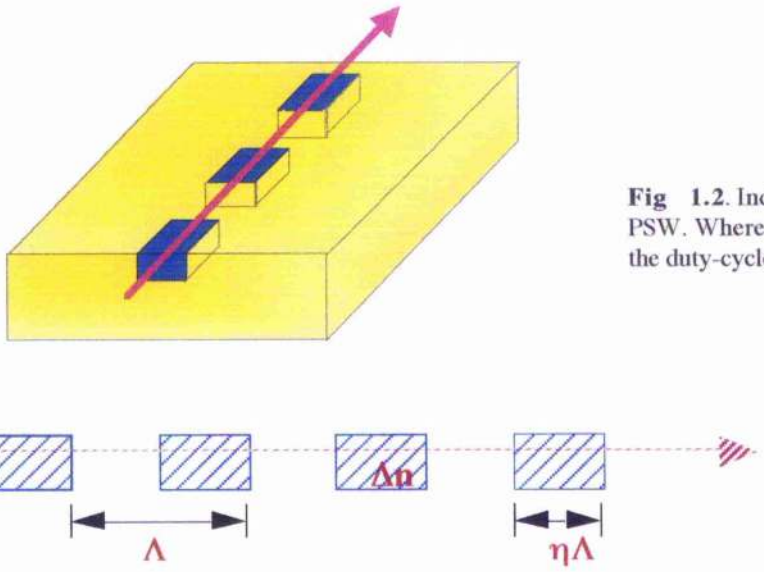

Fig 1.2. Index distribution of a PSW. Where Λ is the period and η the duty-cycle.

In a PSW the refractive index is modulated periodically during fabrication, this is shown schematically in Fig 1.2. Each period of the PSW is composed of two regions with different refractive indices: one region, with an increase in the refractive index of Δn, and another region with a smaller increase in the refractive index (in general it will have the refractive index of the substrate). As a consequence of the segmentation, the loss in the guide is increased and the effective refractive index is reduced when compared to a continuous waveguide. A PSW is characterised by its period, Λ, and duty cycle, η (the ratio of the length of a segment and the period of the guide). It has been demonstrated that a PSW can be represented by an equivalent continuous waveguide with the same depth and width, in which the average index

difference, Δn', is taken to be the weighted average of the index along the propagation direction. This is represented by [20 21, 29, 30].

$$\Delta n' = \eta \Delta n \qquad \text{Eq 1.1}$$

Thus, by choosing the duty cycle, the effective index of the waveguide can be controlled (see Fig 1.3). The refractive index change determines the mode size, propagation constant and cut-off wavelength of the PSW. Control of the mode size permits the fabrication of input and output tapers [19, 20, 28]. The possibility of controlling the propagation constant could be used in asymmetric couplers to provide wavelength filters [26, 27] and in an asymmetrically branched Y-junction to achieve wavelength splitting for wavelength division multiplexing (WDM) applications [31, 25].

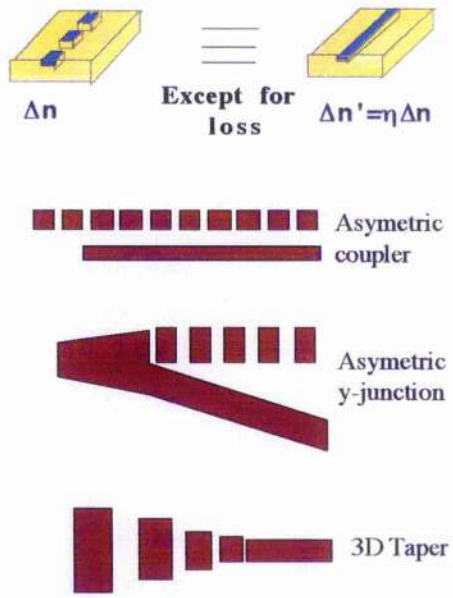

Fig 1.3. PSWs in integrated optics. By choosing the duty cycle, η , the increase in the refractive index of the PSWs, Δn', and therefore the mode size, propagation constant can be controlled in the waveguide.

Equation 1.1 assumes that the refractive index of the PSW is an average of the index along the direction of propagation. To be exact it should be an average of the permittivity. This is because the material properties are introduced thought Maxwell's equations via the permittivity and not the refractive index. However, since Δn is small, terms in Δn^2, or higher, can be neglected, and therefore, the average in the refractive index is equivalent to the average in the permittivity.

PSWs have been modelled by beam propagation method (BPM) [29], coupled-mode-theory (CMT) [29], and the modal method of diffraction gratings [30]. In all these cases the losses and the effective index of the PSWs were calculated on the assumption that the propagation constant and optical field did not change during propagation (z- invariant waveguide).

Some aspects of PSW presented in the literature will be reviewed below, in particular:

- The representation of PSWs by an equivalent continuous waveguide with the same dimension, and increase in the refractive index given by Eq. 1.1.

- The discussion of the influence of the period in the modes of PSWs.

- The influence of the duty cycle on the losses of PSWs.

Different authors have indicated that the refractive index distribution of a PSWs can be represented by Eq 1.1, but the accuracy of this representation is not clear. Li and Burke in Ref. [30] observe that the effective index of a grating model for PSWs is equal to the effective index of the equivalent continuous waveguide. Chou at al. in Ref. [20] show good agreement between the experimental mode size of annealed-proton-exchange PSWs in $LiNbO_3$ with that of an equivalent continuous waveguide, with an average refractive index given by Eq 1.1. Thyagarajan at al. in Ref. [21], using the peak index change and the diffusion depth, showed that the effective index of a PSW can be represented by a continuous waveguide. However, they did not produce any direct evidence on the validity of Eq. 1.1. They found that the diffusion depth of the equivalent waveguide is independent of the duty cycle. Weissman at al. in Ref. [29] using a 2D BPM showed that the effective index of the mode in a PSW is that of a continuous waveguide with an average index difference given by Eq. 1.1. To obtain the mode effective index using the BPM, they did not account for the variations of the intensity profile of the light propagating in a PSW.

Equation 1.1 indicates that the modal properties of a PSW are independent of the period. To that respect Li and Burke in Ref. [30] stated that "*the electromagnetic fields feels only the average index of the waveguide and pays little attention to the segmentation of the index distribution*". Nir at al. in Ref. [22] showed that the intensity distribution of the light guided by a PSW is independent of its period and strongly dependent on its duty cycle. Chou at al. in Ref. [20] showed that the mode depth and width are strongly dependent on duty cycle, and the mode depth is independent of the period, while the mode width is weakly dependent on the period. Thyagarajan at al. in Ref. [21] showed that the mode effective index for different modes in a PSW is strongly dependent on the duty cycle and independent of the period.

PSWs have larger losses than conventional continuous waveguides. At present it is not clear how the duty cycle and period affect the increase in losses. Some experimental results [20, 22] indicate a strong dependence on the duty cycle and weak, or non dependence, on the period. Some theoretical results [28, 29] indicate that both

period and duty cycle will determine the losses in PSWs. Losses cannot be estimated by using an equivalent waveguide defined by Eq. 1.1. Even so, in Refs. [28][29] losses are estimated by extrapolating the characteristics of continuous waveguides to PSWs. It is assumed that the radiation and confined modes of a PSW are those of a continuous waveguide (i.e. the field distribution does not change during propagation). The utility of PSWs depends on their segmentation loss. Determining the factors that will minimise this source of loss allow the design of efficient devices for use in commercial systems.

1.3. Second harmonic generation (SHG).

At the end of the 80s and beginning of the 90s there was much research interest in waveguide second-harmonic generation (SHG) devices to implement compact short wavelength coherent light sources for data storage applications. More recently the second order nonlinear coefficient has been use for all-optical signal processing, mode-locking, pulse compression and solitons formation [32], as well as parametric frequency conversion in OPOs [9]. In this section we summarise the methods proposed in the literature for efficient SHG using periodic structures. In Chapter 5 we will show that some of the proposed methods are not viable.

Important requirements for high efficiency SHG are a large SHG coefficient, large optical field and phase matching. At phase matching, the propagation constant of the incident beam and its second harmonic are equal. But, in general, due to the dispersion of the material this is not the case. Phase matching techniques for waveguide SHG demonstrated so far include temperature and electrooptic tuning using birefringence [33, 34], use of guide mode dispersion [35, 36, 37] , use of periodic structures or grating [38, 16, 24, 10, 39, 40, 41, 17, 18, 42, 11, 43] and automatic matching in Cerenkov-type radiation [44, 45]. The different methods used to obtain phase matching are summarised in Fig 1.4.

In grating phase matching an optical property of the waveguide is periodically modulated and the period of the modulation is used to compensate for any phase mismatch, this is called quasi-phase matching (QPM). If the period for QPM is the same as the period for Bragg reflection, we have Bragg-resonant QPM (B QPM)[17]. But in most cases the period is just used to compensate for the difference in the propagation constant of the pump and SH waves propagating in the forward direction, we will call this mechanism QPM (to differentiate it from B QPM). Quasi phase matching offers many advantages:

- No restrictions imposed on material and polarisation.
- Use of the largest nonlinear tensor component.
- Matching at arbitrary wavelength and temperature.
- High spatial coherence of output.

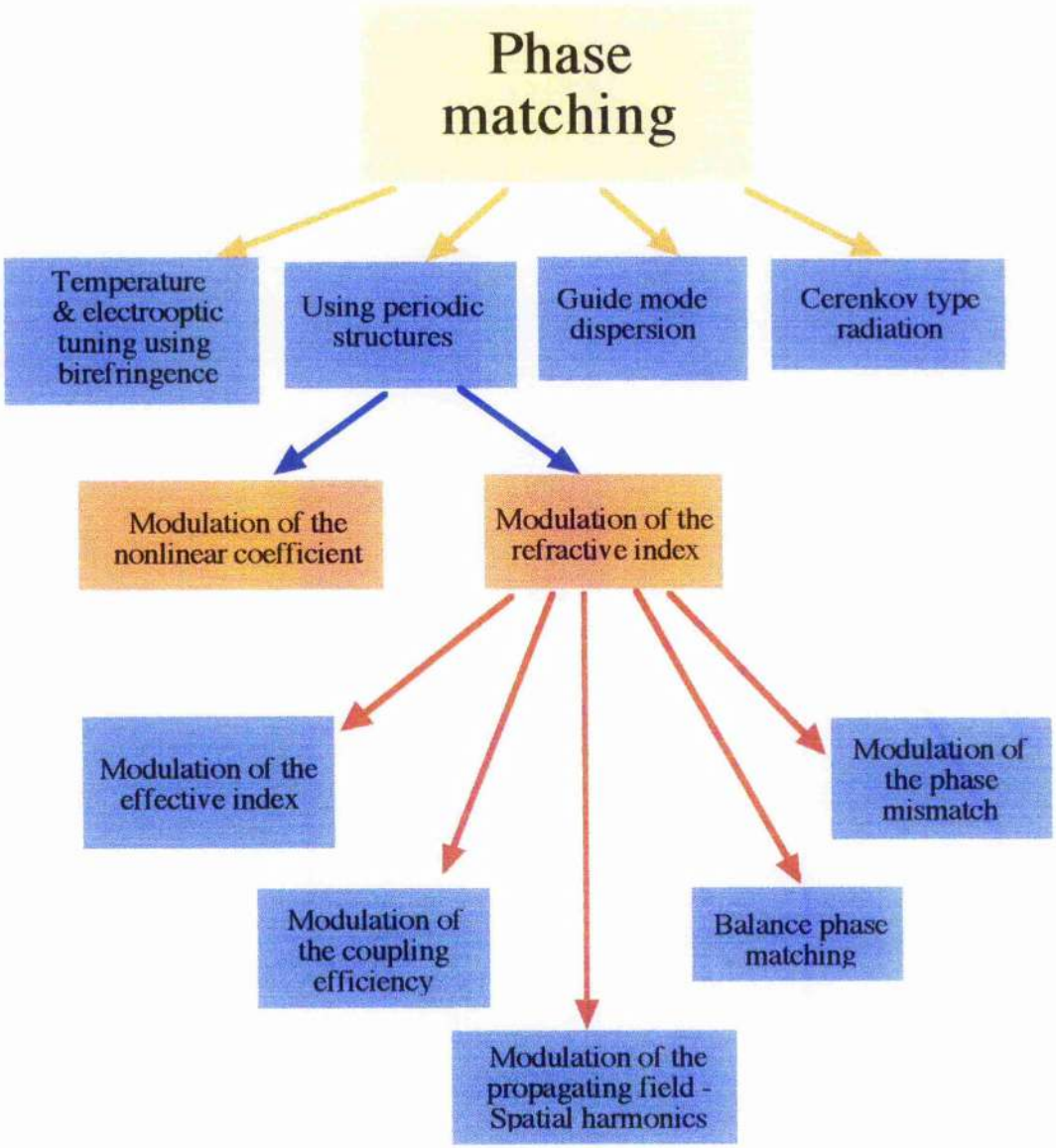

Fig 1.4. Methosd used to obtain phase matching in SHG.

SHG using periodic structures can be achieved by modulating:

- The nonlinear coefficient [42, 46, 18, 11, 41, 43, 16(b), 10, 40, 17, 38].
- The refractive index [10, 16, 17, 38, 39, 40, 41, 43].

A particularly effective type of periodic structure is one in which the sign of the nonlinear coefficient is modulated throughout the waveguide. This can be implemented in ferroelectric material (such as $LiNbO_3$, $LiTaO_3$ and KTP) by reversing the orientation of the dipole moment (domain reversal). Depending on the material and the method used to reverse the domain, the shape of the regions where the nonlinear coefficient is reversed is different. In $LiNbO_3$, titanium indiffusion [10] and lithium outdiffusion [24] lead to domain inverted regions with triangular boundaries. Domain reversal in bulk $LiNbO_3$ [47, 48, 11] and $LiTaO_3$ [49] has been achieved as well by applying an external field, in this case the boundaries of the domain go all the way through the crystal and have nearly vertical walls. In $LiTaO_3$, proton exchange results in domain-inverted regions with a half-circle shape [50, 51], and in KTP, the exchange in a Rb/Ba nitrates solution seems to create very deep domain inverted regions, with no lateral diffusion [18]. The efficiencies of the second harmonic generation are highly dependent on these shapes [46], the most advantageous case is when the domains go deeper than the waveguide and have vertical walls.

PSWs have been used in SHG, in some of the occasions the SHG was produced only by modulation of the refractive index [16(a)] , in other occasions the modulation of the refractive index came accompanied by domain reversal [10, 24 18]. In the last case, both the modulation of the linear and nonlinear properties may contribute to SHG [16(b), 38, 41, 43], and their effects may add either constructively or destructively.

A pure modulation of the refractive index may :

- Modulate the propagation constant. The mode of a PSW may travel with two different propagation constants in the two different segments of a PSW.
- Modulate the phase mismatch. It will take place if the modulation of the propagation constant is different for the fundamental and SH.
- Modulate the coupling efficiency [16(b), 52]. The efficiency of the conversion from the fundamental to the SH is increased as the overlap between the two modes increases. In a PSW the modulation of the refractive index induces a modulation in the mode size. If the overlap integral is different in the two different segments,

the conversion efficiency will be modulated, and this is equivalent to modulating the nonlinear coefficient.

- Modulate the propagating field. *"According to the Bloch's theorem for arbitrary periodic structures, the electric field of the propagating wave of any wavelength in such medium should in general also contain spatial harmonics."* [40]
- Produce balance phase matching. This take place when the phase mismatch in one segment of the PSW is the opposite of the phase mismatch in the other segment. This can be seen as a phase matching situation, where the phase mismatch of the PSW, once Eq 1.1 has been applied, is zero.

An interesting problem in PSWs is that of the propagation constant of the waveguide mode. Until now many authors have considered that the propagation constant will be different in regions with different refractive indices [43, 16, 41]. But, to the knowledge of the author, non of the experiments in which PSWs have been used to generate SH shows evidences of this. Therefore modulation of the effective index and modulation of the phase mismatch may not take place.

But QPM SHG is not a technique without problems and limitations, and they are clearly presented by T. Suhara at al. in Reference [38]:

> *"Exact phase matching can be obtained, in principle, with a grating having a period to compensate the difference between the propagation constants. In practice, however, many factors, e.g., uncertainty of the grating period due to limited accuracy of material constants used in design, fabrication errors, and change of the propagation constants due to grating fabrication, give rise to residual mismatch. Working conditions also affect the phase matching; change of ambient temperature, deviation and fluctuation of laser-diode wavelength, and photorefractive damage in waveguide cause deviation from matching."*

1.4. Methods of analysis of waveguides.

There are two groups of methods used to analyse waveguides (see Fig 1.5), depending on the cross-section of the waveguide. The first uses a mode solver to study waveguides with a cross-section that does not vary along the direction of propagation. The second is a beam propagation method (BPM) which can model the

propagation of light in a waveguide where the cross-section changes along the direction of propagation.

The mode solver is used to calculate the propagation constant and optical field profile of the waveguide modes. The simplest one is the effective index method [53]. This is an approximation method where a 2D problem is decomposed into two 1 D problems, the method is only valid for weakly guiding structures. Although the propagation constant calculated with this method is accurate, this is not the case for the field. Other methods which have been used include the finite difference method, variational method and finite element method. In all these methods the mode profile and propagation constant are obtained from the wave equation. The finite element method usually employs direct solution methods that are numerically intensive. A variety of finite-difference methods have been considered [54] , primarily employing interactive solution techniques, since they are faster and require minimal storage. The variational method [55, 56] is an approximation method and therefore faster. The accuracy of the variational method depends on the closeness of the assumed trial field to the exact mode field of the guiding structure. For a more complete survey of the extensive volume of work in this field, the reader may consult the review by Chiang [57].

The BPM has been used to study Y-junctions, X-crossing waveguides, MMI couplers, periodic segmented waveguides (PSW). The BPM is attractive to the designer of optical devices because it overcomes the difficulties of mode theory when applied to complicated structures, and because of its flexibility as a propagation technique. The BPM is a numerical method which solves the wave equation in some approximate form (usually the Fresnel equation). The original method uses the fast Fourier transform (thus called FFT-BPM) [58, 59, 60]. In the FFT algorithm, each plane wave component of the field profile is calculated using FFT. Then each plane wave component is propagated in the homogeneous medium, and at the end of the propagation step the field in the real space is calculated using inverse FFT. The FFT BPM has limitations that restrict its applications. For instance, in addition to the poor efficiency of the FFT-BPM, a large variation in the transverse refractive index profile of the waveguide will force the method to use extremely small propagation steps. Alternative numerical techniques to solve the wave equation in the spatial domain use a finite difference approximation to replace the partial derivatives in the wave equation (thus called FD-BPM). Recently, this approach has received wide attention from many workers [59, 60, 61, 62, 63 64, 65] . Lately, a vectorial finite-difference beam propagation method has been reported [63]. All FD-BPM techniques

have shown that this approach is much more efficient than then the FFT-BPM in terms of accuracy, speed and storage required. In addition, some of these techniques have succeeded in overcoming the main limitations of low-contrast media in the FFT-BPM, and allow propagation in strongly guiding structures.

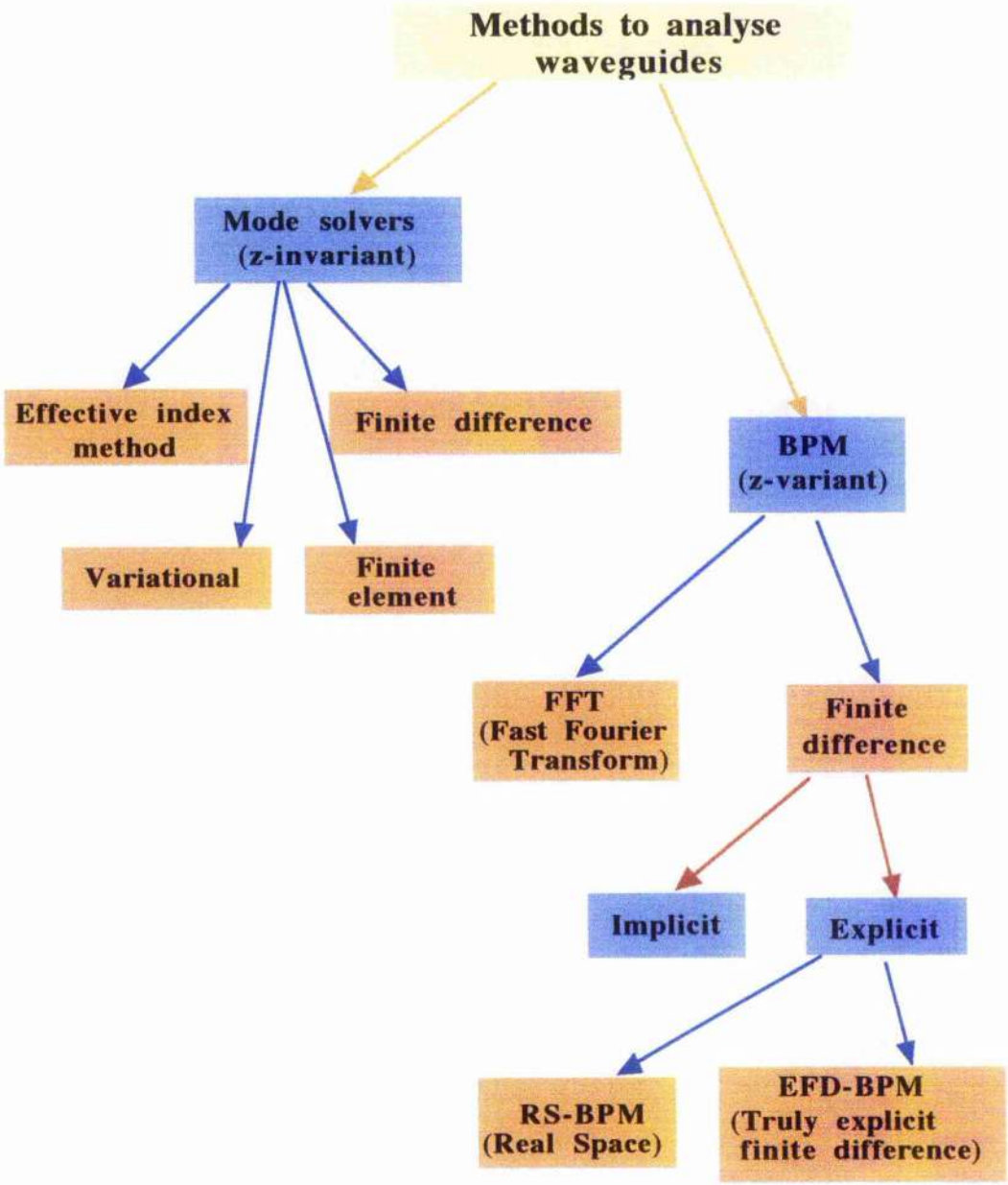

Fig 1.5. Some of the methods used to analyse waveguides.

Generally, the FD-BPM has been used to solve the wave equation by using two methods; the implicit approach and the explicit approach. At present the most popular implicit BPM is based on the alternating direction implicit approximation (ADI-BPM) [60, 61, 63, 64, 65]. The ADI-BPM is unconditionally stable, but requires the solution of a large system of equations for each propagation step. The explicit approach has mainly two ways of formulating the problem; the real space method (RS-BPM) and the truly explicit and therefore called explicit finite difference method (EFD-BPM). The RS-BPM uses the finite difference matrix splitting operator to approximate the wave equation [60, 64, 65]. This method is unconditionally stable but, similar to the FFT-BPM, requires small propagation steps to converge when applied to large contrast media. However, it proves to be much more efficient per propagation step then the ADI- BPM. The EFD-BPM is based on applying the central finite-difference approximation directly to the wave equation [62,64,65]. The propagation of the optical field is straightforward since it involves multiplication of the input field with a very sparse matrix, which makes the method very efficient. However, this algorithm is only conditionally stable, i.e. the method is stable only if the propagation step is smaller than a certain value[62].

1.5. References.

1 J T Milek and M Neuberger, "Linear Electrooptic modular materials", JFI/ Plenum Data Corporation, 1972.

2 W Sohler, "Integrated optics in $LiNbO_3$", Thin Solid Films, **175**, pp. 191--200, 1989.

3 I Baumann, S Bosso, R Brinkmann, R Corsini, M Dinand, A Greiner, K Schafer, J. Sochtig, H Suche, and R Wessel, " Er-Doped Integrated Optical Devices in LiNbO3 ", IEEE Journal of selected topics in quantum electronics, **2**, No 2, pp. 355--366, 1996.

4 F Heismann, R W Smith, "High-speed polarization Scrambler with Adjustable phase chirp", IEEE Journal of selected topics in quantum electronics, **2**, No 2, p 311, 1996

5 T Fujiwara, A Watanable,anf H Mori, "Polarization dependent loss in a Ti:LiNbO3 polarization scrambler/controller", IEEE Photonic technology letters, **8**, no 4, pp. 542--544, 1996

6 F Wehrmann, C Harizi, H Herrmann, U Rust, W Sohler, and S Westenhofer, "Integrated optical, Wavelength selective, acoustically tunable 2*2 switches (add drop multiplexers) in LiNbO3 ", IEEE Journal of selected topics in quantum electronics, **2**, No 2, pp 263--269, 1996

7 H Porte, J P Goedgebuer, W Elflein, A Terras, F Ledeventec, and N Butterlin, "Linear phase tracking in a coherence modulation electrical sensor system using integrated LiNbO3 modulator/demodulator", IEEE Journal of selected topics in quantum electronics, **2**, No 2, p 319, 1996

8 L E Myers, R C Eckardt, M M Fejer, R L Byer, W R Bosenberg and J W Pierce, "Quasi-phasematched optical parametric oscillators using bulk periodically poled LiNbO3 ", JOSA B OPTICAL PHYSICS, 1995, **12**, No.11, pp.2102-2116, 1995.

9 W K Burns, W McElhanon, and L Goldberg, "Second harmonic generation in field poled, quasy-phase-matched, bulk LiNbO3 ", IEEE photonic technology letters, **6**, no 2, pp. 252--254, 1994.

10 M L Bortz, S J Field, M M Fejer, D W Nam, R G Waarts, and D F Welch, "Noncritical quasi-phase matched second harmonic generation in an annealed proton-exchange LiNbO3 waveguide", IEEE Transactions on quantum electronics, **30**, no 12, pp. 2953--2960, 1994.

11 M Fujimura, M Sudoh, K Kintaka, T Suhara, H Nishihsrs, "Resonant waveguide quasi-phase matched SHG devices with electrooptic phase-modulator for tuning", EEE Journal of selected topics in quantum electronics, **2**, No 2, p 311, 1996.
M Fujimura, M Sudoh, K Kintaka, T Suhara, and H Nishihara, "Enhancement of SHG efficiency in periodically poled LiNbO3 waveguide utilising a resonant effect", Electronics Letters, **32**, pp. 1283--1284, (1996).

[12] R Schiek, Y Baek, G Krijnen, and G I Stegaman, I Baumann and W Sohler, "All-optical switching in lithim niobate diectional couplers with cascaded nonlinearity", Optics letters, **21**, no 13, pp. 940--942, 1996.

[13] R Schiek, "All-optical switching in the directional coupler caused by nonlinear refraction duc to cascased second-order nonlinearity", Optical ans quantum electronics, **26**, pp. 415--431, 1994.

[14] J J Veselka and S K Korotky, "Pulse Generation for soliton systems using Lithium Niobate Modulators", IEEE Journal of selected topics in quantum electronics, **2**, No 2, p 396, 1996.

[15] E. B. Pun, K. K. Wong, I. Andonovic, P. J. R. Laybourn, R. De La Rue, "Efficient waveguide Bragg-deflection grating on $LiNbO_3$", Electronics letters, **18**, pp. 774 - 742, (1982).

[16] (a) J. D. Bierlein, D. B. Laubacher, and J. B. Brown, "Balanced phase matching in segmented $KTiOPO_4$ waveguides", Appl. Phys. Lett. **56**, pp. 1725 - 1727, (1990).
(b) J Khurgin, S Colak, R. Stolzenberg, and R N Bhargava, "Mechanism for efficient blue second-harmonic generation in periodically segmented waveguides", Appli. Phys. Lett., **57**, pp. 2540--2542, (1990).

[17] Z Weisman, A Hardy, M Katz, M Oron, and D. Eger, "Second-Harmonic generation in Bragg-resonant quasi-phase-matched periodically segmented waveguides", Optics Letters, **20**, pp. 674--676, (1995).

[18] C J Van Der Poel, J D Bierlein, J B Brown, and S Colak, "Efficient type I blue second harmonic generation in periodically segmented $KTiOPO_4$ waveguides", Appl. Phys. Lett., **57**, pp. 2074--2076, (1990).

[19] F. Dorgeuille, B. Mersali, S. Francois, G. Herve-Gruyer, and M. Filoche, "Spot size transformer with periodically segmented waveguides based on InP", Optics Letters, **20**, pp. 581 - 583, (1995).

[20] M. H. Chou, M. A. Arbone, and M. M. Fejer, "Adiabatically tapered periodic segmentation of channel waveguides for mode-size transformation and fundamental mode excitation", Opt. Lett. **21**, pp. 794 - 796 (1996)
M. H. Chou, M. A. Arbone, and M. M. Fejer, "Periodically-segmented tapered waveguides for mode-size transformation and fundamental mode excitation", 1996 technical digest series , Integrated photonics research, vol 6, pp. 506 - 509, Boston, April 1996.

[21] K. Thyagarajan, C. W. Chien, R. V. Ramaswamy, H. S. Kim, and H. C. Cheng, "Proton-exchange periodically segmented waveguides in $LiNbO_3$ ", Opt. Lett. **19**, pp. 880 - 882, (1994).

[22] D. Nir, S. Ruschin, A. Hardy, and D. Brooks, "Proton exchanged periodically segmented channel waveguides in lithium niobate", Electron. Lett. **31**, pp. 186 - 187, (1995).

[23] D. Nir, Z. Weissman, S. Ruschin, and A. Hardy, "Periodically segmented waveguides in Ti:$LiNbO_3$" Opt. Lett. **19**, pp. 1732 - 1734, (1994).

[24] J. Webjorn, F. Laurell, and G. Arvidsson, "Fabrication of Periodically Domain-inverted Channel Waveguides in Lithium Niobate for Second Harmonic Generation", Journal of Lightwave technology, **7**, pp. 1597 - 1600, (1989).

[25] Z. Weissman, D. Nir, S. Ruschin, and A. Hardy, "Asymmetric Y-junctions wavelength demultiplexer based on segmented waveguides", Appl. Phys. Lett., **67**, pp. 302 - 304, (1995).

[26] R. C. Alferness and R. V. Schmidt "Tunable optical waveguide directional coupler filter", Appl. Phys. Lett. **33**, pp. 161 - 163, (1978).

[27] Z. Weissman, F. Saint-Andre, and A. Kevorkian, "Asymmetric directional couplers using buried ion-exchange, periodically segmented waveguides in glass.", Proc. ECIO'97, pp. 52 - 55, Stockholm April 1997.

[28] Z. Weissman and A. Hardy, "Analysis of Periodically Segmented Waveguide Mode Expanders", Journal of Ligthwave Technology, **13**, pp. 2053 - 2058, (1995).

[29] Z. Weissman and A. Hardy: "Modes of Periodically Segmented Waveguides", J. Lightwave Tech., 1993, **11**, pp. 1831-1838.

[30] Lifeng Li and J. J. Burke, "Linear propagation characteristics of periodically segmented waveguides", Optics Lett., **17**, pp. 1195 - 1197, (1992).

[31] T. Negami, H. Haga, and S. Yamamoto, "Guided-wave optical wavelength demultiplexer using an asymmetric y junction", Appl. Phys. Lett., **54**, pp. 1080 - 1082, (1989).

[32] G. I. Stegeman, D. J. Hagan, and L. Torner, "$\chi^{(2)}$ cascading phenomena and their applications to all-optical signal processing, mode-locking, pulse compression and solitons", Optical and Quantum Electronics, **28**, pp. 1691--1740, (1996).

[33] N Uesugi, and T Kimura, "Efficient second-harmonic generation in three-dimensional $LiNbO_3$ optical waveguide", Appl. Phys. Lett., **29**, pp. 572--574, (1976).

[34] N Uesugi, K Daikoku, and K Kubota, "Electric field tuning of second-harmonic generation in a three-dimensional $LiNbO_3$ optical waveguide", Appli. Phys. Lett. **34**, pp 60--62, (1979).

[35] H Ito and H Inaba, "Efficient phase matched second-harmonic generation method in four-layered optical waveguide structure", Opt. Lett., **2**, pp. 139--141, (1978).

[36] M DeMicheli, J Botineau, S Neves, P Sibillot, D B Ostrowski, and M Papuchon, "Extension of second-harmonic phase matching range in lithium niobate waveguides", Opt. Lett., **8**, pp. 116--118, (1983).

[37] H Itoh, K Hotta, H Takara, and K Sasaki, "Frequency doubling of a Nd:YAG laser by a MNA single crystal thing film on slab-type optical glass waveguide", Appl. Opt., **25**, p. 1491--1496, (1986).

[38] T Suhara, and H Nishihara, "Theoretical Analysis of Waveguide Second Harmonic Generation Phase Matched with Uniform and Chirped Gratings", IEEE J Quantum Electron., **26**, pp. 1265--1276, (1990).

[39] S Somekh, and A Yariv, "Phase-matchable nonlinear optical interactions in periodic thin films", Appl. Phys. Lett., **21**, pp 140--141, (1972).

[40] C L Tang, and P Bey, "Phase Matching in Second-Harmonic Generation Using Artificial Periodic Structures, "IEEE J Quantum Electro., **QE-9**, pp. 9--17, (1973).

[41] C Q Xu, H Okayama, and M Kawahara, "Optical Frequency Conversion in Nonlinear Medium with Periodically Modulated Linear and Nonlinear Optical Parameters", IEEE J Quantum Electro., **31**, pp. 981--987, (1985)

[42] M W Street, N D Whitbread, C J Hamilton, B Vogel, C R Stanley, D C Hutchings, J H Marsh, G T Kennedy, W Sibbett, and J S Aitchison, Modification of the second-order optical nonlinearities in AlGaAs asymmetric multiple quantum well waveguides by quantum well intermixing", Appl. Phys. Lett., **70**, pp. 2804--2806, (1997).

[43] M M Fejer, G A Magel, D H Jundt, and R L Byer, "Quasi-Phase-Matched Second Harmonic Generation: Tuning and Tolerances", IEEE J Quantum Electro., **28**, pp. 2631--2654, (1992)

[44] H. Sato, and Y Azumai, "Cerenkov radiative second-harmonic generation enhancement with a periodically corrugated nonlinear susceptibility in a slab waveguide", J Opt. Soc. Am B, **10**, pp. 894--897, (1993).

[45] H. Ito, T Fujiwara, and Choichi Takyu, "Cerenkov-type second harmonic generation from a LiNbO3 waveguide with a periodic domain gratin", Optics Communication, **99**, pp 237--240, (1993).

[46] D Delacort, F Armani, and M Papuchon, "Second-Harmonic Generation Efficiency inPeriodically Poled $LiNbO_3$ waveguides", IEEE J. Quantum Elctron., **30**, pp. 1090--1099, (1994).

[47] W K Burns, W McElhanon, and L Goldberg, "Second Harmonic Generation in Field Poled, Quasi-Phase-Matched, Bulk $LiNbO_3$", IEEE Photonics Technology letters, **6**, pp 252--254, (1994).

[48] V Proneri, R Koch, P G Kazansky, W A Clarkson P St J Russell, and D C Hanna, Opt. Lett., **20**, pp. 2375-- ,(1995).

[49] K Mizuuchi and K Yamamoto, "Generation of 340 nm light by frequency doubling of a laser diode in bulk periodically poled $LiTaO_3$", Optics Letters, **21**, pp. 107--109, (1996).

[50] K Mizuuchi , K Yamamoto, and T Taniuchi, "Second harmonic generation of blue light in$LiTaO_3$ waveguide", Apli. Phys. Lett., **58**, pp. 2732--2734, (1991).

[51] K Mizuuchi, and K Yamamoto, "Highly efficient quasi-phase-matched second harmonic generation using a first order periodically domain inverted $LiTaO_3$ waveguide", Appl. Phys. Lett., **60**, pp. 1283--1258, (1992).

[52] C G Trevino-Placios, G I Stegeman, and P Baldi, "Spatial nonreciprocity on waveguide second-order processes", Optics Letters, **21**, pp. 1442--1444, (1996),.

[53] G. B. Hocker and W. K. Burns, "Mode dispersion in diffused channel waveguides by the effective index method", Applied Optics, **16**, 113 (1977).

[54] G. R. Hadley, and R. E. Smith "Full-Vector Waveguide Modeling Using an Iterative Finate-Difference Method with Transparent Boundary Conditions", J. Lightwave Thechnol, **LT-13**, no. 3, pp. 465-469, (1995).

[55] A Sharma and P Bindal, "Analysis of Diffused Planar and Channel Waveguides" IEEE J. Quantum Electron, **QE-29**, no. 1, pp. 150-153. (1993).

[56] A Sharma and P Bindal, "An accurate variational analysis of single-mode diffused channel waveguides", Optical Quant. Electron., **24**, pp. 1539-1371, (1992).

[57] K S Chiang, "Review of numerical and approximate methods for the modal analysis of general optical dielectric waveguides", Optical Quant. Electron., **26**, pp S113-S134, (1994).

[58] M D Feit and J A Fleck "Analisis of intersecting difused channel waveguides", IEEE J. Quantum Electron, **QE-21**, pp. 1799-1805, (1985).

[59] D Yevick, " A guide to electric field propagation techniques for guide-wave optics", Optical Quant. Electron., **26**, pp. s185-s197, (1994).

[60] D Yevick and B. Hermansson, "Efficient beam propagation techniques", IEEE J. Quantum Electron, **QE-26**, pp. 109-112, (1990).

[61] Y. Chung and N. Dagli "An assessment of finate diffrence beam propagation method". IEEE J. Quantum Electron, **QE-26**, pp. 1335-1339, (1991).

[62] Y. Chung and N. Dagli "Analysis of Z-invariant a Z-variant semiconductor rib waveguides by explicit finite diffrence beam propagation method with nonuniform mesh configuration", IEEE J. Quantum Electron, **QE-27**, pp. 2296-2305, (1991).

[63] W Huang, C Xu, S Chu and S Chaudhari, "The finite difference vector beam propagation method:analisis and assessment", J. Lightwave Tech, **10**, pp. 209-305 (1992).

[64] H M Masoudi and J M Arnold, "Parallel beam propagation methods", IEEE Photonics Thechnology Letters, **6**, no. 7, pp. 848-850, (1994).

[65] H. M. Masoudi and J. M. Arnold, "Parallel three-dimensional finite difference beam propagation methods", International Journal of numerical Modeling: electronic networks, devices and fields, (1995).

2

$LiNbO_3$

2.1. Introduction.

Lithium Niobate ($LiNbO_3$) was first grown in 1965, since then much work has been done to understand its properties. Today, good quality wafers, single domain and transparent from 0.4 to 5 μm are routinely available. From the beginning, researchers realised that $LiNbO_3$ was ferroelectric at room temperature, with an elevated Curie temperature: 1120 °C. This permits the processing of the material at high temperatures without affecting the direction of the domain. In 1966, X-ray diffraction and neutron diffraction was used to obtain the crystal structure, and hence the origins of the ferroelectric, pyroelectric and piezoelectric characteristics, as well as its birefringence. Ferroelectric $LiNbO_3$ is non centrosymmetric, providing with second order nonlinearities and first order electro-optic effect.

The interest in $LiNbO_3$ continued to grow when in 1975 titanium diffusion waveguides were first fabricated, opening the possibility for integrated optics. Six years later in 1981 proton exchange waveguides were produced as an alternative to titanium indiffusion. In the present work only Ti:$LiNbO_3$ waveguides were fabricated, and therefore only this process will be discussed. From the end of the 70's to nearly the end of the 80's research labs worked to understand the different aspects of the in-diffusion of titanium into Ti:$LiNbO_3$; in particular the indiffusion process, the titanium concentration distribution, the increase in the refractive index, the Li_2O outdiffusion and the domain reversal associated with the indiffusion, the fabrication conditions that minimise transmission losses, and the photorefractive damage amongst others

2.2. $LiNbO_3$ crystal.

In 1965 Ballman and Fedulov independently reported successful applications of the Czochralski technique to grow $LiNbO_3$ [1][2]. The next year, a cornerstone series of five papers on $LiNbO_3$ came from Bell Laboratories [3][4][5][6][7]. There are

several review papers and books on $LiNbO_3$ [8][9][10][11]. In Refs. [9][12] thorough reviews of reported values of the different material coefficients can be found.

2.2.1. Growth

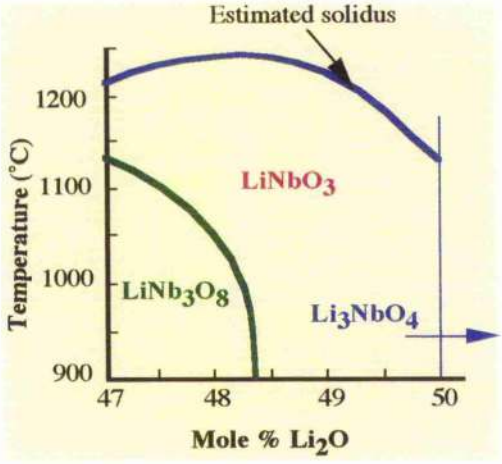

Fig 2.1 . Phase diagram of $LiNbO_3$ in the temperature range 900-1250 °C [after 13]

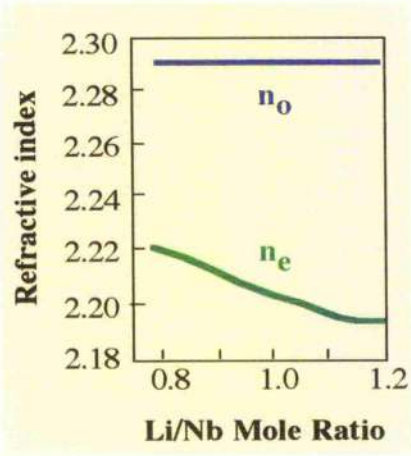

Fig 2.2 Refractive indices of $LiNbO_3$ at 0.6328 μm as a function of the molar ratio Li_2O/Nb_2O_5 in the melt [after 17].

$LiNbO_3$ has a solid-solution range from 44% mol to 50 % mol Li_2O, and grows with variable composition, depending on the ratio of the starting compounds used. The phase diagram of the Li_2O:Nb_2O_5 system in Fig 2.1 [13] shows a single phase $LiNbO_3$ region extending from a Li_2O-deficient phase boundary that is temperature dependent to a Li_2O-rich phase boundary located at, or very near to, the stoichiometric composition (50% mol Li_2O) [14][15][16]. Crystals for device applications are cut from boules grown by the Czochralski method from a congruent melt at 48.6 mol % Li_2O. Congruent crystals are the simplest to grow uniformly and without cracks.

The properties of $LiNbO_3$ depend on the stoichiometry of the crystal, this is the case of the Curie temperature [14][17][18], which lies in the range 1020-1180 °C. The birefringence is also strongly dependent on the crystal composition [17][18][19][20]. Only the extraordinary refractive index is dependent upon the stoichiometry, while the ordinary index is independent, this can be seen in Fig 2.2 [17]. The electrooptic effect shows little variation with the crystal composition [21]. Miller and Norland [22] have reported that only the d_{31} second order nonlinear coefficient is strongly dependent on the crystal composition.

2.2.2. Crystallography, pyroelectricity and piezoelectricity.

The detailed structure of $LiNbO_3$ at room temperature has been unambiguously established by X-ray and neutron diffraction studies of single domain crystals by Abrahams et al. [5]. The crystal structure is a slightly distorted hexagonal close-packed (hcp) oxygen lattice. The octahedral interstice formed are one third filled by lithium ions, one third filed by niobium ions and one third vacant and this can be seen in Fig 2.3. $LiNbO_3$ is ferroelectric at room temperature and paraelectric above the Curie temperature. For congruent $LiNbO_3$ the Curie temperature is approximately 1120 °C, close to its melting point at about 1260 °C. When the temperature is above the Curie point, the lithium ions lie within the plane of the oxygen ions; the niobium ions are midway between planes. Hence, the crystal has no charge (paraelectric). When the temperature is below the Curie point, both the lithium and the niobium ions move in the same direction, resulting in a permanent dipole moment (ferroelectric). This can be seen in Fig 2.4. The polarity increases with decreasing temperature, which means that one end of the c axis (c^+) gets a positive pyroelectric charge on cooling while the opposite end (c^-) gets a negative charge. Similarly, the polarisation will affect the stress in the material which in turn leads to piezoelectricity. During crystal growth, if no precautions are taken, the structure will consist of microscopic ferroelectric domains, where adjacent domains have opposite polarities. To obtain single domain material a $LiNbO_3$ crystal, or boule section is poled with a strong DC field along the direction of the dipoles [4][8]. The poling can be performed either during, or after the growth of the $LiNbO_3$ boule.

$LiNbO_3$ in its ferroelectric phase possesses a three-fold rotational symmetry about the c-axis, making it a member of the trigonal crystal system. It also has mirror symmetry about three planes 60° apart rotating about the c-axis, but is noncentrosymmetric and is thus classified as a member of the 3m point group (see Fig 2.3). Paraelectric $LiNbO_3$ is a member of the $\bar{3}m$ point group (trigonal crystal system as well). Crystals which belong to the trigonal group can be structurally classified using either a hexagonal, or a rhombohedral, unit cell. The hexagonal unit cell has six formula units while the equivalent rhombohedral has two formula units.

The hexagonal unit cell has three equivalent a_H axes and one c_H axes (see Fig 2.3). The optical properties of the ferroelectric phase are usually described in terms of orthonormal x, y and z components. The z axis is chosen to be the symmetry axis, the c axis. The y axis is chosen to be in a mirror plane. This can be seen in Fig 2.3. The senses of the y and z axes are chosen so that their positive ends exit crystal faces that obtain a positive piezoelectric charge under compression. The x axis is chosen to

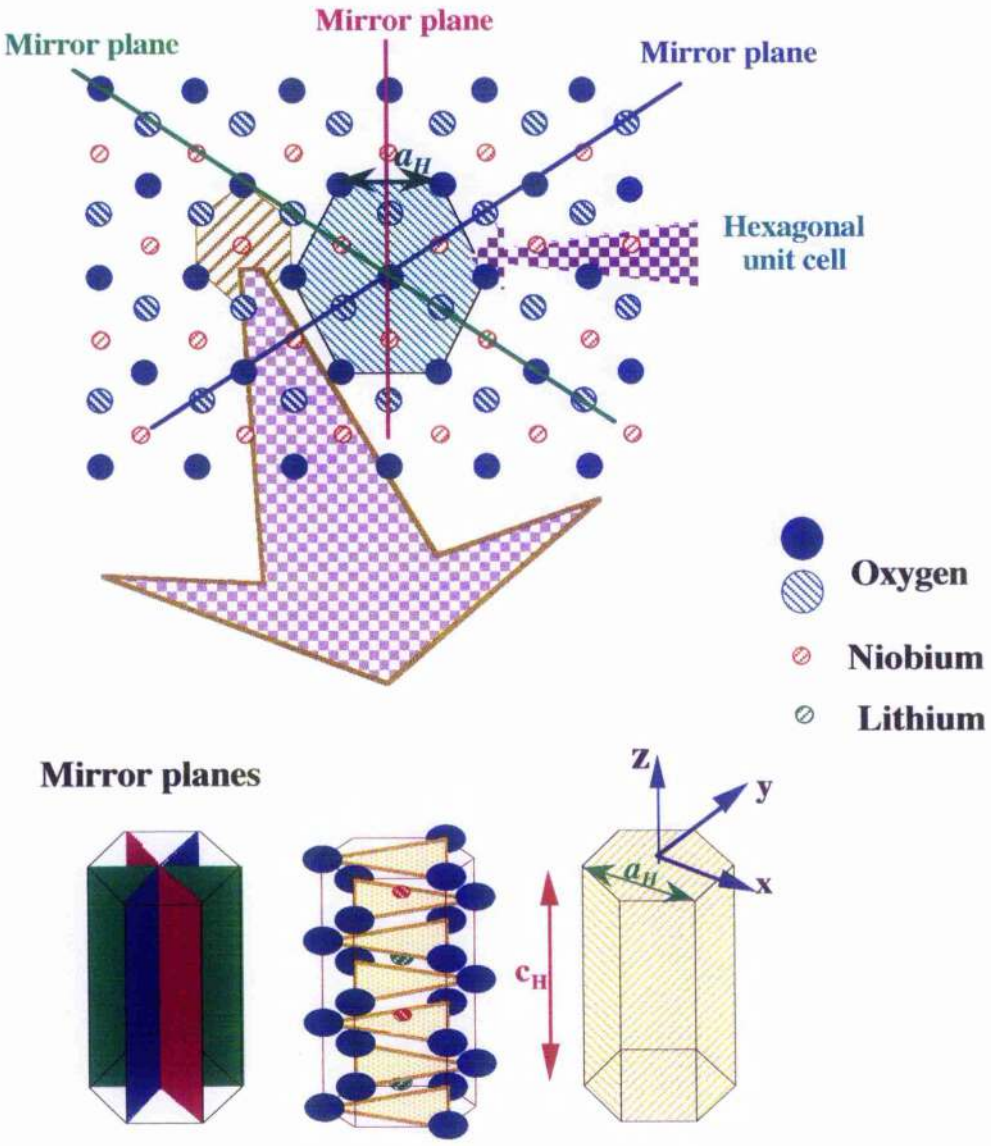

Fig 2.3. Ferroelectric $LiNbO_3$ is classified as a member of the 3m point group, therefore possesses a three-fold rotational symmetry about the c-axis, making it a member of the trigonal crystal system. It also has mirror symmetry about three planes 60° apart rotating about the c-axis.

$LiNbO_3$ crystallise in a slightly distorted hexagonal close packed (hcp) oxygen lattice, with 6 formula units per unit cell. This hexagonal unit cell has three equivalent a_H axes and one c_H axis, the symmetry axis.

z axis - Symmetry axis. Opposite direction in neighbouring domains.
y axis - In a mirror plane. Opposite direction in neighbouring domains.
x axis - Parallel to any a_H axis. Same direction in neighbouring domains.

The positive end of the z and y axes has positive piezoelectric change under compression. The positive end of the z axis has positive charge on cooling.

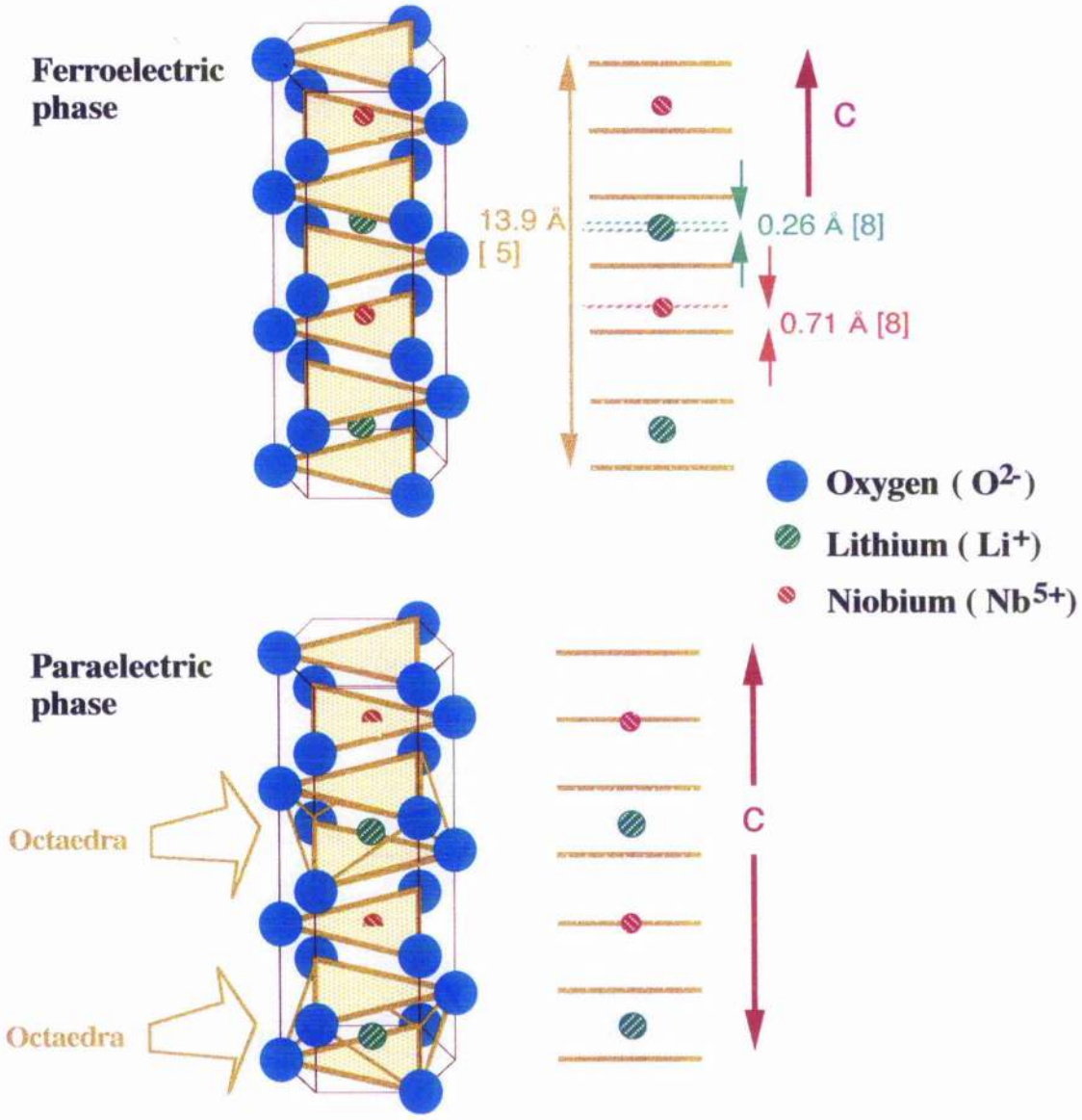

Fig 2.4. In the paraelectric phase, the Nb^{5+} ions are at the centre of the oxygen octaedra and the Li^+ ions are arranged at the centre of the oxygen triangles between the octaedras. In reality the Li^+ ions will be found, with equal probability, above and below the oxygen planes at a distance of 0.37 Å, and therefore, we represent the average position of the Li^+ ions in the crystal lattice [9].

Below the Curie point, in the ferroelectric phase, the Li^+ ions shift to one side of the oxygen triangles, and the Nb^{5+} ions move slightly away from the Li^+ ions. This movement causes a permanent dipole to be set up along the c-axis of the crystal, therefore $LiNbO_3$ passes from being centrosimetric in the paraelectric phase to being non-centrosimetric in the ferroelectric phase. This give rises to the nonlinear, piezoelectric and electrooptic properties of $LiNbO_3$.

obtain right-handedness [23]. Therefore, the z axis coincides with the c-axes, the x axes with any of the a_H axes and the positive z face gets a positive pyroelectric charge on cooling.

The dial axis of the paraelectric lattice coincides with the x axis. As a result, the direction of this axis will be the same in the ferroelectric phase, independent of on which side of the oxygen plane the lithium ions switch to. While the y and z axes have opposite directions in neighbouring domains. Piezoelectricity, the electro-optic effect and the non-linear properties are related to a lack of inversion symmetry, the case of the nonlinear coefficient is discussed in Appendix 1. The lack of inversion symmetry changes the sign of these coefficients in opposite domains.

2.2.3. Dielectric properties - Birefringence and transmission.

Lithium niobate single crystals are uniaxial negative (with the refractive index of the ordinary ray larger than the refractive index of the extraordinary ray, i.e. $n_O > n_e$). The optical axis is the c axis as shown in Fig 2.3 and 2.4.

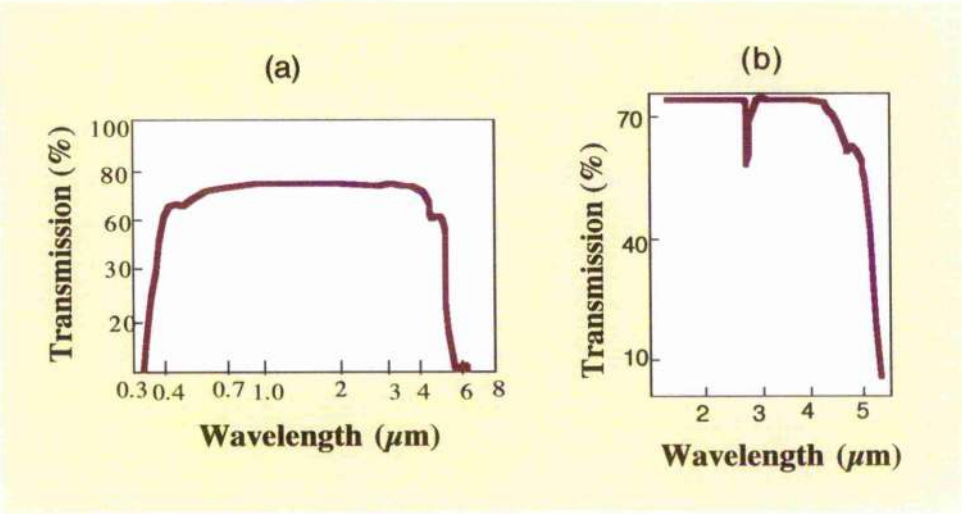

Fig 2.5. Transmission of single-domain $LiNbO_3$ as a function of the wavelength. Transmission is uncorrected for reflection losses. (a) was obtained from Crystal technology Inc. and (b) was obtained from reference [10].

$LiNbO_3$ is transparent from about 0.4 to 5 μm [3][4]. In the infrared region there is a narrow absorption band at λ=2.9 μm, due to OH^- grouping, this can be seen in Fig 2.5. The nature of the transmission spectra depends on the conditions of heat treatment and polarisation of crystals, as can be seen in Fig 2.6. Clear colourless

lithium niobate single crystals transmit as much as 72 % (without corrections for reflections) over a range $\lambda = 0.4$–4 μm. In a 1 cm thick specimen at $\lambda = 1.06$ μm, 5.6 % of the radiation is lost by absorption and 14.6 % by reflection from one surface, so that the total loss is 31%. To reduce the losses due to reflection, a single quarter wavelength coating of quartz (n=1.46), or magnesium fluoride (n=1.38) may be applied to the $LiNbO_3$ crystal surface [24].

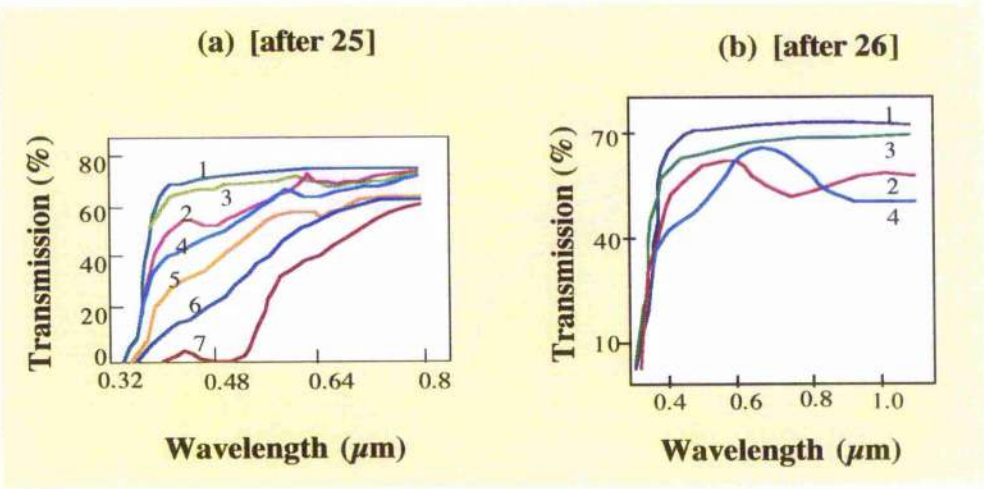

Fig 2.6(a). Transmission of variously colored $LiNbO_3$ crystals as a function of the wavelength:

1- Clear crystal
2- Yellowish
3- Crystal 2 after annealing in oxygen
4- Crystal 2 after annealing for 5 min in hydrogen at 500 °C
5- Yellowish
6- Orange
7- Dark brown

Fig 2.6(b). Optical transmission spectra for congruently melting $LiNbO_3$ single crystal.

1- Pulled without electric current maintained during the growth process
2- Grown with no electric current and subject to poling and concurrent annealing in a separate furnace
3- Grown with electric current in the growth process
4- Heated in Hydrogen.

Analysis of experimental data yields two equations for the temperature dependence of the ordinary and extraordinary refractive indices (n_o and n_e) between. 0.4 μm and 4 μm [10]:

$$n^2 = A_1 + \frac{A_2 + B_1 T^2}{\lambda^2 - \left(A_3 + B_2 T^2\right)^2} - A_4 \lambda^2 + B_3 T^2 \qquad \text{Eq 2.1}$$

	A_1	A_2	A_3	A_4
n_o	4.9130	0.1173	0.212	0.0278
n_e	4.5567	0.097	0.201	0.0224

	B_1	B_2	B_3
n_o	1.65×10^{-8}	2.7×10^{-8}	0
n_e	2.7×10^{-8}	5.4×10^{-8}	2.605×10^{-7}

TABLE 2.1

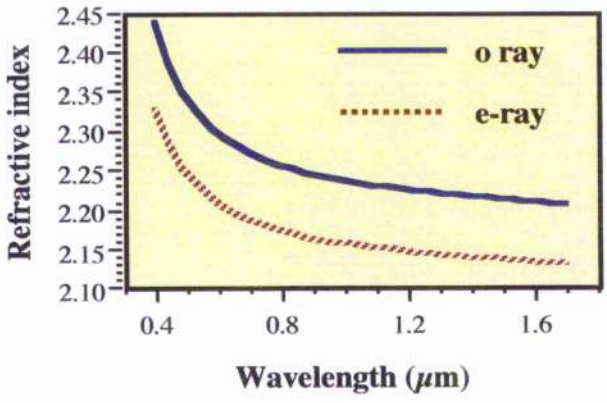

Fig 2.7. Dispersion curves for $LiNbO_3$ at 300 °K.

Where T, in Eq 2.1, is the temperature in K and λ is the wavelength in μm. The dispersion curves for the extraordinary and ordinary ray are shown in Fig 2.7.

The standard deviation of 112 experimentally determined values of the refractive indices from those calculated accordingly to the above formula is 2.2×10^{-4}, demonstrating the accuracy of Eq 2.1.

2.2.4. Photorefraction.

In $LiNbO_3$ high intensities of light can cause local changes in the refractive index that distort the incident wavefront, this phenomenon is called photorefraction. Fe^{2+} and Fe^{3+} ions, always present in $LiNbO_3$, can be photoexcited to produce electrons and holes respectively:

$$Fe^{2+} + h\upsilon \Rightarrow Fe^{3+} + e^{-}$$
$$Fe^{3+} + h\upsilon \Rightarrow Fe^{2+} + hole^{+}$$

and an optically induced space charge field can be generated within the crystal [27].

In general the ratio of Fe^{2+} to Fe^{3+} is not equal to one, and neither electrons, nor holes, are the majority charge carriers. If electrons are in the majority the space charge is set up within the crystal when electrons are exited out of the illuminated region and re-trapped by Fe^{3+} ions away from the light beam. This movement of charge results in an electric field, and, via the electro-optic effect, a change in the refractive index around the beam of light. Since both electrons and holes can contribute to the photovoltaic current, the ratio of Fe^{2+} to Fe^{3+} ions will affect the magnitude of the space charge field and hence, the magnitude of the photorefractive response of the material.

The photorefractivity in the crystal can be minimised by oxidising, or reducing, the crystal so that we obtain the Fe^{2+}/Fe^{3+} ratio for which the photorefractivity is minimum. At this point the electrons and hole currents are equal and opposite and no net space charge is being set up in the crystal. Above approximately 170 °C the photorefractive effect (optical damage) relaxes faster than it is generated.

2.2.5. Nonlinear optical properties.

As already mentioned $LiNbO_3$ at room temperature is a noncentrosymmetric crystal, and therefore, has second order nonlinearities. $LiNbO_3$ has large second order susceptibilities, whereas the third order coefficients are rather small.

The second order polarisation can be written as a function of the contracted tensor and has the following expression:

$$\underline{p}^{NL}(2\omega) = 2\varepsilon_0 d(\omega_1, \omega_2) : \left[\underline{E}(\omega)\right]^2 \qquad \text{Eq 2.2}$$

General crystallographic considerations indicate that for a 3m point group the nonlinear polarisation can be expressed as:

$$\begin{pmatrix} p_x^{2\omega} \\ p_y^{2\omega} \\ p_z^{2\omega} \end{pmatrix} = 2\varepsilon_0 \begin{pmatrix} 0 & 0 & 0 & 0 & d_{15} & -d_{22} \\ -d_{22} & d_{22} & 0 & d_{31} & 0 & 0 \\ d_{31} & d_{31} & d_{33} & 0 & 0 & 0 \end{pmatrix} \begin{pmatrix} \left(E_x^{\omega}\right)^2 \\ \left(E_y^{\omega}\right)^2 \\ \left(E_z^{\omega}\right)^2 \\ 2E_y^{\omega}E_z^{\omega} \\ 2E_x^{\omega}E_z^{\omega} \\ 2E_x^{\omega}E_y^{\omega} \end{pmatrix} \qquad \text{Eq 2.3}$$

Appendix 1 illustrates the determination of the zero and non-zero coefficients for the nonlinear tensor. Usually, the Kleinman symmetry is also applied: As long as there is no strong dispersion between the wavelength of the mixing field, all terms d_{ijk}, which result from a rearrangement of the subscripts i, j, k, are equal. Here this makes $d_{15}=d_{31}$.. The magnitude of the non-zero coefficients are:

d_{15}=6 pm/v
d_{22}=3 pm/v
d_{33}=30 pm/v

Further details on the value of the nonlinear coefficients can be seen in References [8][22][28]

2.3. Ti:$LiNbO_3$ waveguides.

Optical waveguides can be fabricated in $LiNbO_3$ using several different methods; the out-diffusion of Li_2O from the crystal surface, the indiffusion of metals, ion implantation and ion, or proton, exchange. The two most widely used methods are Ti indiffusion and proton exchange [29][30][31]. Titanium indiffusion increases both the extraordinary ($\Delta n_e<0.02$) and the ordinary ($\Delta n_o<0.004$) refractive indices allowing both TE and TM polarisations to be guided. Proton-exchange produces guides with a large change in the extraordinary refractive index ($\Delta n_e<0.18$) and a slight decrease in the ordinary index ($\Delta n_o>-0.05$). Ti indiffusion waveguides are prone to photorefractive damage, and the high temperatures used in fabrication can lead to Li_2O outdiffusion from the crystal surface. Proton exchange waveguides do not suffer significant photorefractive effect [29], but an index profile instability has been detected [32][33], and in these waveguides the nonlinear coefficients are reduced [34].

2.3.1. Titanium-indiffusion.

The indiffusion of certain metals atoms into $LiNbO_3$ produces changes in the optical properties and specifically in the refractive index. Titanium, being tetravalent, is substitutional for Nb in the $LiNbO_3$ crystal lattice and has proved to be the most attractive of the metals for indiffusion. The exact mechanism by which the indiffusion of titanium increases the refractive index is not yet fully understood but it appears to be due to several complex interactions [35][36].

The standard method for fabricating Ti indiffused waveguides commences with the deposition of a Ti film onto the $LiNbO_3$ substrate by means of electron beam evaporation. Films thickness typically in the region of 20 to 120 nm have been used. The indiffusion of the titanium takes place between 900 and 1050 °C, with diffusion times between 0.5 and 30 hours. The diffusion temperature is limited by the Curie temperature (1120 °C) of the crystal. If the Curie temperature is exceeded the crystal must be re-poled to turn it back to a single domain again.

2.3.1.1. Diffusion stages.

The indiffusion process can be broken down into several stages [29][37][36]:

- Firstly the titanium oxidises to form TiO_2 during the furnace heat up period at approximately 500 °C.
- In the absence of a wet atmosphere during diffusion the $LiNb_3O_8$ crystalline phase appears at 600 °C and rapidly disappears after reaching a maximum at 800 °C. A wet atmosphere inhibits the formation of $LiNb_3O_8$.
- The TiO_2 layer forms an intermediate rutile structure most likely to be $(Li_{0.25}Nb_{0.75}O_2)_{0.422}(TiO_2)_{0.58}$. It is this rutile compound that is the real source for the subsequent titanium-indiffusion into the $LiNbO_3$ [36]. Armenise et al. in references [29][38] propose a different compound as the source for Ti diffusion: $(Ti_{0.65}Nb_{0.35})O_2$
- At temperatures usually as high as 1000 °C the titanium diffuses from the surface layer into the substrate until the $(Li_{0.25}Nb_{0.75}O_2)_{0.42}(TiO_2)_{0.58}$ is completely depleted and disappears. Just before the process is complete, investigation of the surface layer by scanning electron microscopy has revealed islands of the mixed oxide. This reveals the non-uniform nature of the indiffusion process that is responsible for the refractive index inhomogeneties. Increasing the diffusion time reduces the surface roughness and decreases the inhomogeneties in the index.
- Precipitation of $LiNb_3O_8$ may take place during cooling at temperatures between 600 °C and 900 C with a maximum precipitation at 800 °C. Cooling rates >3 °C/min are sufficiently rapid to avoid precipitation of $LiNb_3O_8$. The precipitation phase lead to an increase in optical scattering in the sample **[15]**

2.3.1.2. In-plane scattering

Optical losses in slab waveguides have been attributed to in-plane scattering [37]. The scattering depends upon the diffusion time (the losses initially decrease and then

increase with increasing diffusion time [37], see Fig 2.8) with the optimum time increasing with the titanium film thickness. The scattering can be attributed to three main causes [37]:

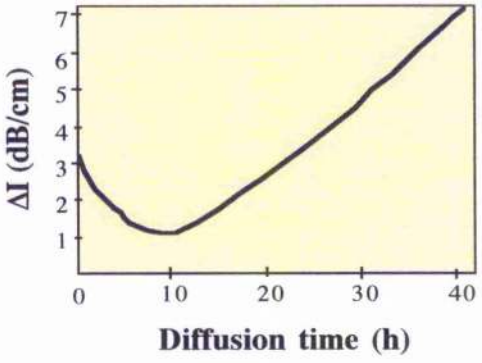

Fig 2.8. ΔI gives a measure of the waveguide quality, it indicate how performance is degraded by inplane scattering. Diffusion temperature 1000 °C, sample coated with a 25 nm thick of Ti [37]

- Non-uniformities which occur during the Ti indiffusion, will create refractive index irregularities in the guide and in the surface.
- Roughness left on the surface after diffusion.
- Crystal strains and defects introduced by the titanium ions in the guiding region.

The surface roughness and index homogeneties can be reduced by increasing the diffusion time, while the crystal defects are induced by the diffusion process and therefore the density of the defects increases with the diffusion time [37].

References [39] and [40] discussed the insertion losses of Ti:$LiNbO_3$ waveguides for a variety of fabrication conditions. The best results were obtained for a z-cut wafer; the insertion loss was 1 dB (1.3 cm waveguide), while the propagation loss was 0.3 dB/cm.

2.3.1.3. Li_2O outdiffusion

While the titanium is diffused into the $LiNbO_3$ substrate, there is an associated outdiffusion of Li_2O from the surface of the $LiNbO_3$. Lithium has a low activation energy and therefore diffuses very rapidly compared to the niobium, or oxygen, the Li_2O outdiffusion will increase the extraordinary refractive index and leave the ordinary index unaffected (see Fig 2.2). Therefore, when a stripe guide is produced this can result in a slab guide at the surface of the $LiNbO_3$ in addition to the stripe guide. The resulting slab guiding has only an increased extraordinary index with a maximum at the surface and a depth profile which can be mathematically modelled using a complementary error function.

To suppress outdiffusion, either an increase of Li partial pressure or the use of wet diffusion atmosphere have been proposed. Jackel et al observe in Reference [41] that the indiffusion in a water vapour atmosphere (pure oxygen flowing through water)

eliminates the outdiffusion of Li_2O by inhibiting the $LiNb_3O_8$ phase, but this affects the optical properties of the waveguides increasing the in-plane scattering levels [37]. Eknoyan et al. in Reference [42] investigated the characteristics of Ti:$LiNbO_3$ waveguides diffused in both dry and wet O_2. They observed no complete suppression of outdiffusion in samples annealed in wet oxygen. Schuppert in Reference [43] investigated the outdiffusion of Li_2O using dry and wet synthetic air. He suggested that the application of a wet gas without an additional Li_2O/LiOH source yields a strong increase of waveguiding (strong increase of outdiffusion) due to the following chemical reaction

$$Li_2O + H_2O \rightarrow 2LiOH$$

Shuppert reports that out diffusion in a wet atmosphere is suppressed only if used in combination with a Li_2O source that increases the Li partial pressure. This is because the outdiffusion in the Li_2O source (an added wafer of $LiNbO_3$ powder) is strongly increased by the water vapour leading to an increased Li_2O pressure in the diffuse tube, which itself lowers outdiffusion in the sample. He found that a suppression of the outdiffusion by means of increasing the Li partial pressure in a dry atmosphere is only successful for long diffusion times. This is because a longer time is necessary to raise the Li partial pressure. Fouchet et al. [44] diffused Ti into $LiNbO_3$ in a flowing atmosphere of dry argon cooled in oxygen. They reported no index variation associated with Li_2O outdiffussion.

The exact mechanisms by which the various methods work are not yet fully understood and the development of an understanding has evolved though trial and error, with only a limited amount of exact scientific understanding. In this work waveguides were fabricated by Ti indiffusion in a dry O_2 atmosphere, and cool down in a dry O_2 atmosphere. No slab guiding due to Li_2O depletion was observed.

2.3.1.4. Photorefractive effect in waveguides.

One of the most important issues which must be considered is the photorefractive effect. It manifests itself as a gradual refractive index change due to irradiation with relatively intense visible light; the effect is observed in Ti-indiffused waveguides [45][46][47][48][49] as well as bulk crystals [50][53]. When the intensity of the light is further increased, a spatial distribution of refractive index is developed and the wave is scattered out of the waveguide [52]. The photorefractive effect can be split into two components, the photovoltaic effect and the photoconductive effect. The photovoltaic effect describes an optically induced change in the refractive index

in the absence of an electric field, while the photoconductive effect describes an optically induced change in the refractive index in the presence of an electrical field. The photorefractive effect in bulk $LiNbO_3$ [50] is normally dominated by the photovoltaic effect. Following titanium-indiffusion Becker et al. [51] reported no increase in the photovoltaic effect from that observed in bulk $LiNbO_3$ for a Mach-Zehnder structure formed on x-cut $LiNbO_3$. The photoconductive effect showed a substantial increase to become the dominant photorefractive mechanism for a field strength of 5×10^3 V/cm. Schmidt et al [48] reported similar effects, using a directional coupler on z-cut $LiNbO_3$, for a field 10^4 V/cm, with the magnitude of the effect decreasing very strongly with increasing wavelength. Harvey [49] has made a comparison between both Mach-Zehnder devices and directional couples fabricated in z-cut $LiNbO_3$. The directional couplers showed an effect in agreement with Schmidt et al [48] while little effect was observed in the Mach-Zehnder. Harvey used a biasing field strength of 103 V/cm, at this level the degree of damage due to the photoconductive effect is reduced enough for the photovoltaic effect to dominate. Chon at al in Ref. [45] presented a theoretical model of the photovoltaic effect in z-cut Ti:$LiNbO_3$ channel waveguides together with experimental results for mode size and output power as a function of the input optical power. Fujiwara et al. in Ref. [46] study the wavelength dependence of the photovoltaic effect in z-cut Ti:$LiNbO_3$ channel waveguides. They show that at 1.1 μm the power necessary to induce a given photovoltaic effect is 3 orders of magnitude larger than at 0.63 μm. At 0.53 μm the photovoltaic damage threshold of a Ti:$LiNbO_3$ channel waveguide is 20 W/cm^2 [45], i.e. in a 5 × 5 μm^2 waveguide, the photovoltaic damage threshold is 5 μw.

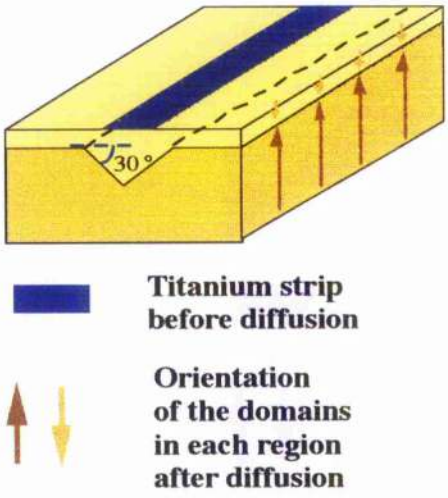

Fig 2.9. Domain orientation after Ti indiffusion in the positive face of a z-cut $LiNbO_3$.

2.3.1.5. Ti-indiffusion domain reversal.

In a z-cut wafer of $LiNbO_3$, integrated optical devices are generally fabricated in the negative z face [54][56]. This is because the diffusion in the positive z face reverses the ferroelectric domain of the area that has been indiffused, this can be seen in Fig 2.9. As mentioned earlier, areas with opposite domain orientation have electrooptic coefficients with different sign. Therefore, in these waveguides light propagates through areas with positive and negative electrooptic

coefficients, reducing the average effect [56]. However, there are situations where domain reversal may be desirable, and titanium indiffusion can be used to periodically reverse the sign of the electrooptic or non-linear coefficient.

One can distinguish between at least two cases for which domain reversal in the positive face has been reported (without applying an external field); the first is a domain inversion in titanium indiffused areas [54][55][56][57] and the second is a domain inversion occurring on bare substrates after heat treatment above about 800 °C [58][59]. The physical mechanisms of domain inversion have been discussed for instance by Peuzin and Miyazawa [57] and by Nakamura et al. [59], although all details are not fully understood. It seems clear, however, that the inversion is related to a composition gradient in the crystal. Such gradients are present in both situations; in the first case mainly due to titanium indiffusion and in the second cases due to Li_2O outdiffusion. At one face of the $LiNbO_3$ crystal, the composition gradient is antiparallel to the optical axis orientation, and at the other the gradient is parallel to the optical axis. This can explain why the inversion occurs only at the positive face.

Ti indiffusion takes place when the crystal is heated to 900 - 1100 °C, and inversion occurs at 1020 °C. The typical indiffusion depth is of the order of 2-4 μm and it has been shown that the inversion depth is proportional to the Ti thickness [56] and the diffusion time [73]. The shape of the inverted regions is triangular with an angle of 30° with the surface boundary (see Fig 2.9).

For both Ti doped and lithium deficient material, the Curie temperature is lower than for congruent material [54]. This means that, at a uniform temperature, a sample with spatially varying Ti concentration will have a varying ferroelectric polarisation and, thus, alternating electrical fields that can affect the domain pattern, this can be seen in Fig 2.10. Since indiffusion is carried out at temperatures closer to the Curie temperature, this field may be sufficient to reverse the polarisation. Nassau et al. in Ref. [4] reported that domain inversion was successful with an electric field of 5 V/cm at 20°C below the Curie temperature. At room temperature 24 kV/mm was required to reverse the domains. A spatial variation in polarisation can, of course, also be obtained in a uniform sample as a result of local temperature variations [60]. Near the Curie temperature the material is not a perfect insulator. Therefore, the electric field will slowly be compensated through charge transfer. This means that the heating and cooling rates are important parameters for the inversion process.

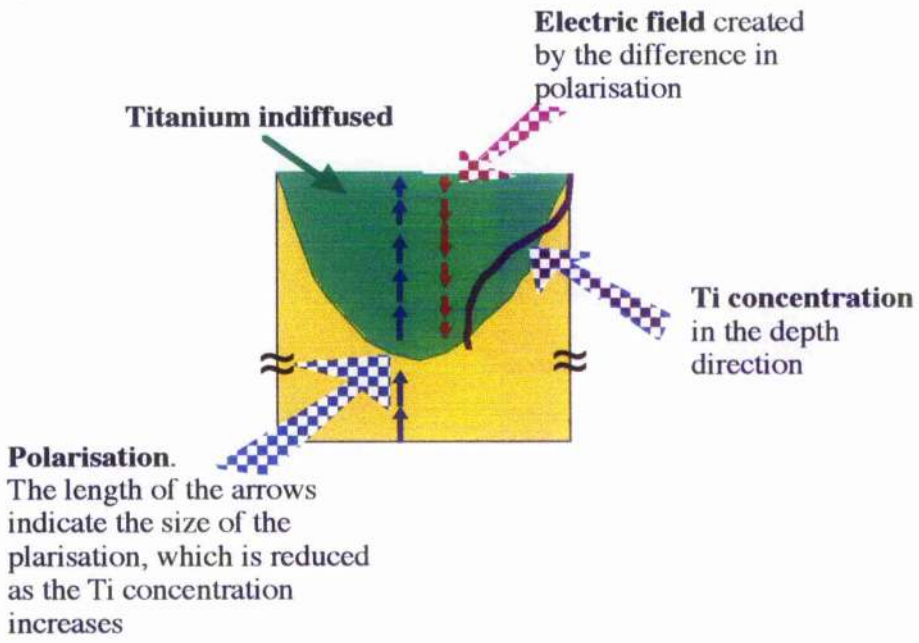

Fig 2.10. Electric field created by the gradient of the titanium during the diffusion process

The effects of gradients inside the boule are not difficult to evaluate. It has been established that for a Y-doping there is an equivalent poling filed which is antiparallel to the concentration gradient. The conditions that prevail in the interior of the crystal boule are quite different from those at the surface of a wafer during heat treatment in a diffusion furnace. In this case the domain formation occurs at the surface, and among other things, this means that pyroelectric surface charge has to be considered. Furthermore , there is evidence that the history of the sample is important for the reversal process [61][62]. A review of the different pooling techniques can be seen in reference [74].

2.3.2. Refractive index profile of Ti:$LiNbO_3$ waveguides.

To date the origin of Titanium induced refractive index change has not been satisfactorily explained. As a consequence, these profiles have to be experimentally determined.

Several papers have already dealt with that problem [63][64][65][66][44][13]. The diffusion conditions; air, argon, or oxygen atmosphere, either wet or dry, are very different from one laboratory to the other [67]. Consequently the dispersion of reported results is very important. The disagreement between data, even for

diffusion conditions apparently identical, could be due to a poor control of diffusion process (lithium out-diffusion for example) or crystal quality. Despite these differences, most of published papers agree to consider that Δn_e and the titanium concentration, C, are proportional, or nearly proportional whereas Δn_o has a nonlinear behaviour versus C [63][66][44].

Although several reported values show that the diffusion of Ti^{4+} ions into the $LiNbO_3$ substrate is anisotropic with a diffusion coefficient in the z-direction 50 % larger than in the x-direction [66][68], other reports show that the diffusion coefficient in the z-direction is 30 % larger than in the y-direction [69][44], and yet other reports show no anisotropy but a strong dependence of the diffusion coefficient upon the stoichiometry of the crystal [13]. Here we are going to use the diffusion coefficient measured by Fouchet at al. in Reference [44].

2.3.2.1. Titanium concentration distribution after diffusion.

The diffused titanium concentration in a continuous waveguide has been shown to be closely modelled by a Gaussian profile in the depth direction and an error function in the lateral direction and can be described by the following approximation [70]:

$$C(y,z) = \frac{1}{2} C_o \exp\left(-\frac{z^2}{D_z^2}\right)\left[erf\left(\frac{W+2y}{2D_y}\right) + erf\left(\frac{W-2y}{2D_y}\right)\right]$$

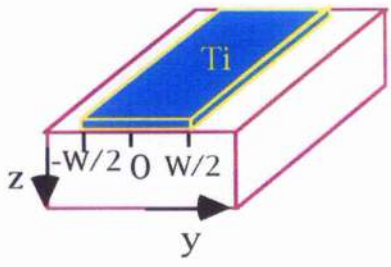

Fig 2.11

Where W is the width of the titanium strip before diffusion (see Fig 2.11), C_o is the titanium surface concentration, and D_z and D_y are the diffusion length in both directions. C_o and the diffusion lengths can be obtained experimentally [44]. Here we are more interested in representing them as a function of the fabrication conditions (Ti thickness and diffusion time) and material parameters (Ti density before diffusion and diffusion coefficient).

The titanium surface concentration, C_o, is a function of the thickness of the Ti strip before diffusion, τ, the diffusion depth, D_z, and Ti density before diffusion, C_f. The relationship is given by [44],

$$C_o = \frac{2}{\sqrt{\pi}} C_f \frac{\tau}{D_z}$$

The diffusion lengths D_z and D_y are a function of the diffusion time, and the diffusion coefficients d_z and d_y. These can be seen in the following equation

$$D_z = 2\sqrt{d_z t}$$
$$D_y = 2\sqrt{d_y t}$$

Therefore, the unknown parameters are C_f, d_z and d_y, and they have to be obtained experimentally. The atomic density of solid Ti is 5.6×10^{28} atoms/m^3. But the density of the Ti film may be reduced depending on the process used to deposit it. Reference [71] uses a 75% density correction for sputtered Ti, while reference [44] measured 68% density correction, making $C_f=3.8\times10^{28}$ atoms/m^3. The Arrhenius law indicates that the diffusion coefficients depend on the activation energy and the diffusion temperature[44]. For a diffusion temperature of 1050 °C Fouchet at al.[44] measured the diffusion coefficients on Z-cut $LiNbO_3$ to be

d_z= 0.68 $\mu m^2/h$
d_y= 0.457 $\mu m^2/h$

2.3.2.2. Increase in the refractive index with Ti concentration.

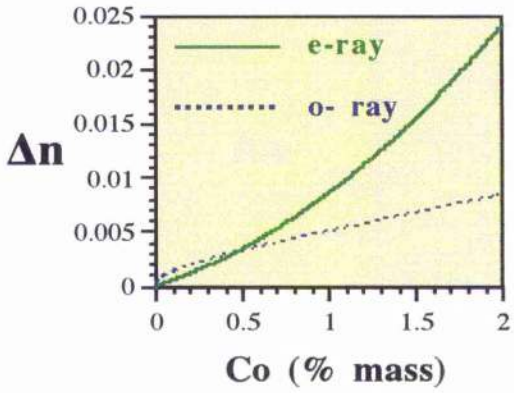

Fig 2.12. Increase in the refractive index as a function of the Ti concentration at 300 °K for an operating wavelength of 1.3 μm.

Based on experimental data Fouchet at al. [44] showed that the increase in the extraordinary index is superlinearly dependent on the titanium concentration, while the ordinary index can be well defined with a sublinear relationship with the titanium concentration, this can be seen in Fig 2.12. They proposed the following relationship between the increases of

the indices and the titanium concentration :

$$\Delta n_e = a^{\alpha_e}\left(B_0(\lambda) + B_1(\lambda)aC_o\right)\left[C(y,z)\right]^{\alpha_e}$$
$$\Delta n_o = a^{\alpha_o}\left(B_0(\lambda) + B_1(\lambda)aC_o\right)\left[C(y,z)\right]^{\alpha_o}$$

Where

$$\frac{1}{a} = \frac{2}{\sqrt{\pi}}C_f$$

For n_o:
$$B_0 = 6.53\times10^{-2} - 3.15\times10^{-2}\lambda + 7.09\times10^{-3}\lambda^2$$
$$B_1 = 0.478 + 0.464\lambda - 0.348\lambda^2$$

For n_e:
$$B_0 = 0.385 - 0.430\lambda + 0.171\lambda^2$$
$$B_1 = 9.13 + 3.85\lambda - 2.49\lambda^2$$

α_e=0.83
α_o=0.53

The dispersion relation is valid for wavelengths in the range $0.6 \leq \lambda(\mu m) \leq 1.6$, and for Ti surface concentrations going up to 2% in mass.

We decided to use the description of the index profile described by Fouchet et al. [44] because accounts for high Ti concentrations and the wavelength dispersion goes up to 1.55 μm. But this in not the only model found in the it the literature, Strake et al. [72] have proposed another model based on a different set of experimental results, however, it only describe situations were the Ti concentrations is smaller than 0.9×10^{21} atoms/cm^{-3} and for a wavelength range going from 0.6 to 1.2 μm.

2.3.2.3. Maximum surface Ti concentration

The highest surface concentration (C_o) of Ti in $LiNbO_3$ is about 2 % in mass. The titanium concentration in percent is defined with reference to the atomic density of solid Ti (C_{Ti}). Therefore, the titanium surface concentration in mass percent is given by:

$$C_o(in\ \%) = \frac{C_o}{C_{Ti}}100$$
$$C_{Ti} = 5.6\times10^{28}\ atom/m^3$$

Therefore, the titanium thickness, τ, and the diffusion time, t, have to fulfil the following relationship to ensure a surface concentration below 2%

$$\frac{\tau}{\sqrt{t}} < 4a\sqrt{d_z}\frac{C_{Ti}}{100}$$

2.3.3. The fabrication of titanium indiffused guides.

The fabrication steps for the titanium indiffused waveguides are shown schematically in Fig 2.13.

Before coating the sample with photoresist, the substrate was cleaned using the following well established procedure: Sequence of solvents

- OPTICLEAR
- Acetone
- Methanol
- RO (reverse osmosis) water

Method: The sample was placed in a bath and covered completely with the solvent and ultrasonic for 5 mins. Finally the sample was rinsed for 3 mins with RO water. The excess water was removed from the substrate with an air gun and placed on a hot plate to dry completely. The ferroelectric nature of $LiNbO_3$ implies the need for care during the cleaning procedure to avoid the electrostatic attraction of dust particles.

Z-cut wafers were used. The waveguides were fabricated onto the negative face to avoid domain reversal, or in the positive face to produce domain reversal

The photoresist, 1400-31, was spun at 4000 rpm for 30 seconds, leaving a 1.8 μm thick layer. To harden the photoresist for exposure, the substrate was baked at 90 °C for 15 minutes, soaked in chlorobenzene for 15 minutes and then baked again at 90 °C for a further 15 minutes. Soaking the substrate in the chlorobenzene creates a hard layer of photoresist at the surface which caused it to be undercut at the edge of the developed strip. This greatly increases the ease with which the titanium on top of the photoresist was removed during lift-off and improve the quality of the titanium strips edges.

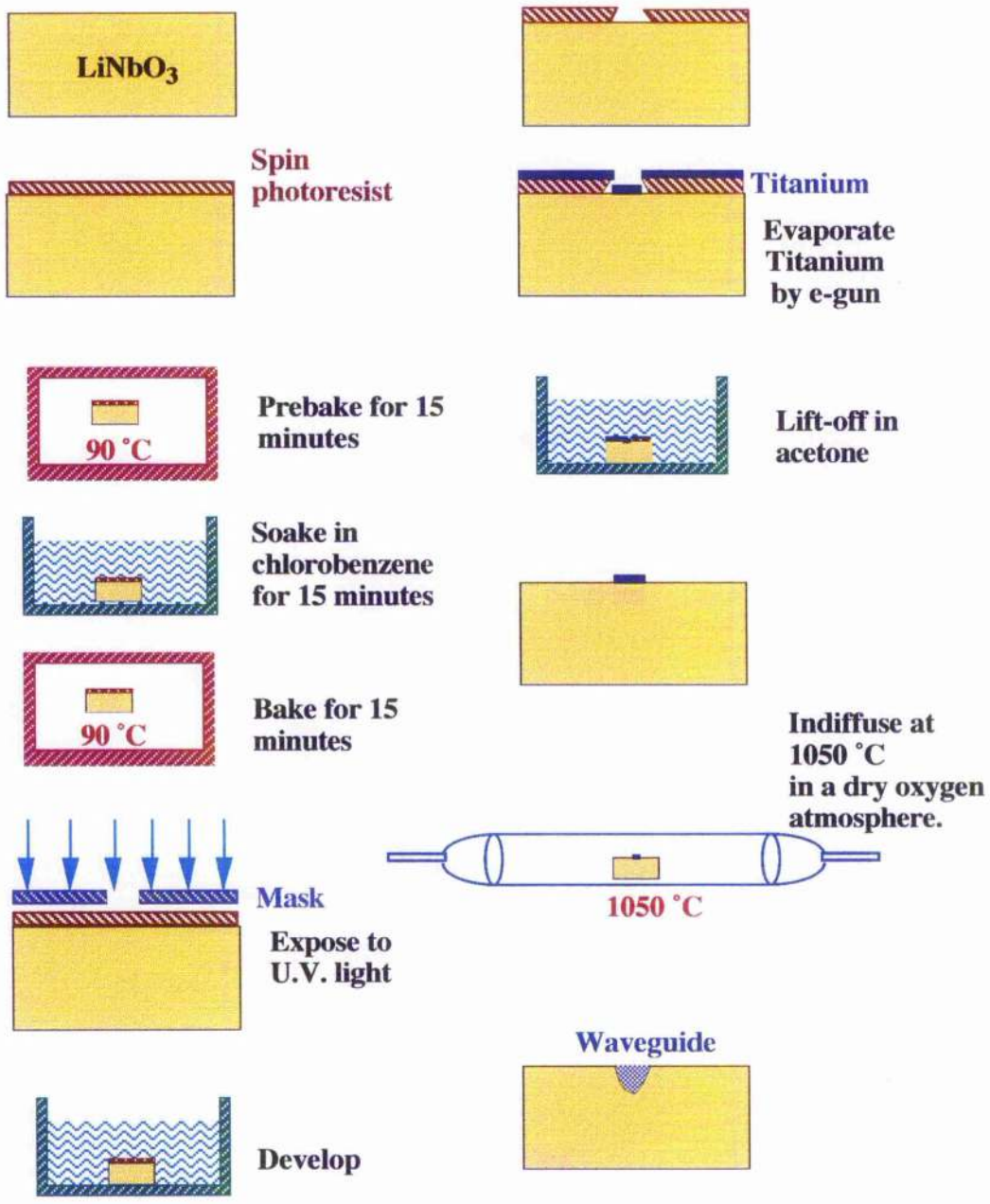

Fig 2.13. Fabrication steps of titanium indiffused waveguides

Next, the baked photoresist was patterned, 1400-31 is a positive photoresist, and with a dark field mask the pattern of the mask will be transfered to the substrate after lift-off. After exposing the photoresist to UV light and developing, titanium was evaporated on the patterned substrate with an electron-gun. To avoid titanium deposition at the edges of the photoresist the evaporation was set to be normal to the substrate. Evaporation was carried out in a vacuum chamber at a pressure of 4×10^{-6} mbar.

After lift-off the titanium was indiffused at 1050 °C in a dry oxygen atmosphere, small changes in the temperature should be implemented to avoid thermal shock while bringing the sample up to the diffusion temperature, and while cooling it down after. To introduce the sample into the furnace, first, the boat containing the samples was placed at the entry of the tube (see Fig 2.14), and after 15 minutes the boat was slowly pushed into the furnace; a process which takes 20 minutes. Once the cap of the tube had been put in place, a small flux of oxygen was passed through the tube. To cool the sample down, the furnace was switched off letting the oxygen flow. The reduction of the temperature as a function of time can be seen in Fig 2.15.

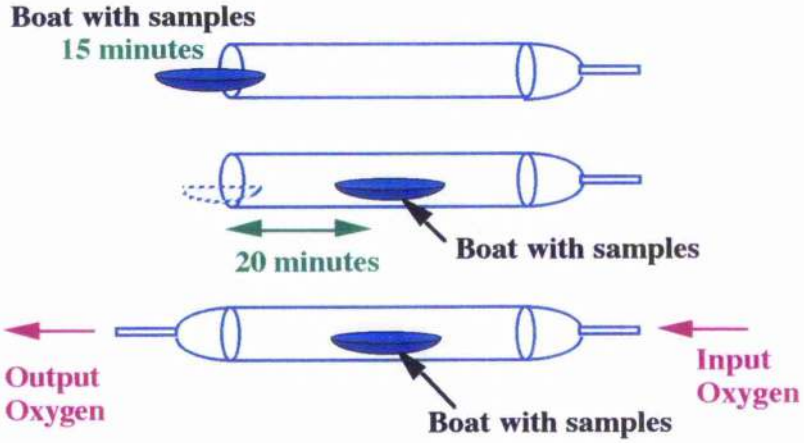

Fig 2.14. Procedure used to raise the temperature of the sample up to the diffusion temperature.

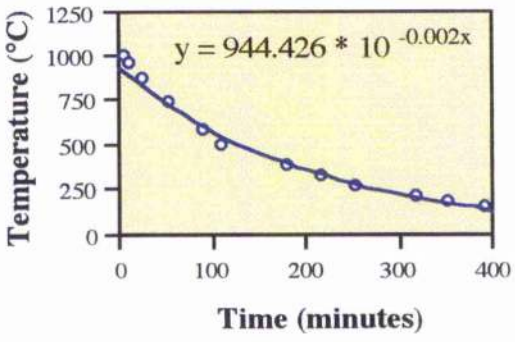

Fig 2.15. Reduction in the furnaces temperature as a function of the time elapse after the furnace had be switched off.

2.4. Summary.

In this Chapter we reviewed some of the properties of bulk $LiNbO_3$ and titanium diffused $LiNbO_3$ waveguides. We have seen that $LiNbO_3$ is a good material for optics; wafers are routinely grown with the same composition and it is transparent from 0.4 to 5 μm. The crystalline structure of $LiNbO_3$ has been presented and from there some characteristics have been discussed: pyroelectricity, piezoelectricity, birefringence, nonlinear behaviour and titanium domain reversal. A brief review of the different aspects associated with the fabrication of titanium diffused waveguides has been discussed. Especially those that can affect the performance of the waveguides used in this work: scattering, Li_2O out diffusion (capable of producing slab guiding) and photorefractive damage. In Chapter 3 we will see that scattering losses and outdiffusion of Li_2O has not seriously affected the performance of our waveguides (we were not able to detect any slab guiding associated with Li_2O outdiffusion). This leaves the threshold for photorefractive damage as potentially the more important problem in Ti:$LiNbO_3$ waveguides, but in Chapter 5 photorefractive damage, if it existed, did not present a problem in SHG.

By looking at all work done on $LiNbO_3$ over the last 30 years, the reader realises that a large amount of information about $LiNbO_3$ has been accumulated. But it can not be said that all the process involved in the fabrication of Ti:$LiNbO_3$ waveguides are always understood. This is the case for Li_2O outdiffusion, the increase in the refractive index, the domain reversal associate with titanium indiffusion, and even the diffusion process itself. Therefore, the optimum fabrication conditions for a particular application are obtained, to a certain degree, by trail and error, always making use of the already existing information. In situations where the behaviour of the waveguide has to be predicted, the major difficulty comes from the variety of diffusion coefficients reported in the literature.

At the end of the Chapter we described the particulars of our fabrication procedures. To pattern the titanium strips on the surface of the $LiNbO_3$ substrate is a straight forward procedure. Bringing the sample up to the diffusion temperature, selecting the atmosphere in the furnace and cooling down the sample are the most critical steps. But, the generation of a good waveguide is mostly dictated by the diffusion time, diffusion temperature and thickness of the titanium strip.

2.5. References.

[1] A A Ballman, "Growth of piezoelectric and ferroelectric materials by the Czochralski technique", J Am. Ceram. Soc., **48**, pp 112--113, (1965).

[2] S A Fedulov, Z I Shapiro, and PB Ladyzhinskii, "The growth of crystals of LiNbO3, LiTaO3 and NaNbO3 by the Czochralski method", Sov. Phys. Crystallography, **10**, pp 218--220, 1965.

[3] K Nassau, H J Levinstein, and G M Loiacono, "Ferroelectric lithium niobate. 1. Growth, domain structure, dislocation and etching", J Phys. Chem. Solids, **27**, 983--988, 1966.

[4] K Nassau, H J Levinstein, and G M Loiacono, "Ferroelectric lithium niobate. 2. Preparation of single domain crystals", J Phys. Chem. Solids, **27**, 989--996, 1966.

[5] S C Abrahams, J M Reddy and J L Bernstein, "Ferroelectric lithiun niobate. 3. Single crystal X-ray diffaction study at 24 C", J Phys. Chem. Solids, **27**, 997--1012, 1966.

[6] S C Abrahams, W C Hamilton, and J M Reddy "Ferroelectric lithiun niobate. 4. Single crystal neutron diffaction study at 24 C", J Phys. Chem. Solids, **27**, 1013--1018, 1966.

[7] S C Abrahams, H J Levinstein, and J M Reddy "Ferroelectric lithiun niobate. 5. Polycrystal X-ray diffraction study between 24 C and 1200 C", J Phys. Chem. Solids, **27**, 1019--1026, 1966.

[8] A Rauber, Chemestry and physics of lithium niobate", in Curent topics in material science **1**, E Kaldis (ed), pp. 481--601, North-Holland 1978.

[9] R S Weis and T K Gaylord, "Lithium niobate: summary of physical and crystal structure", Appl. Phys. A, **37**, pp 191--203, 1985.

[10] A M Prokhorov, and Yu S Kuz'minov, " Physics and Chemestry of crystalline lithium niobate, Adam Hilger, Bristol, 1990.

[11] EMIS Data reviews series no 5, "Properties of lithium niobate", Institute of Electrical Engineers, INSPECT, London, 1989.

[12] Landolt-Bornstein numerical data and functional relationships in science and technology, III/16a and III/28a: 3. LiNbO3 family

[13] R J Holmes and D M Smyth, "Titanium diffusion into LiNbo3 as a function of stoichiometry", J Appl. Phys., **55**, pp. 3531--3535, 1984.

[14] J R Carruthers, GE Peterson, M Grasso, and P M Bridenbaugh, " Nonstoichiometry and crystal growth of LiNbO3", J Appl. Phys, **42**, p 1846, 1971.

[15] L O Svaasand, M Eriksrud, A P Grale, F Mo, "Crystal growth and properties of LiNb3O8", J Cryst. Growth, **18**, p 179, 1973.

[16] L O Svaasand, M Eriksrud, G Nakken, A P Grale, "Solid solution range of lithium niobate", J Cryst. Growth, **22**, p 239, 1974.

[17] J G Bergman, A Ashkin, A A Ballman, J M Dziedzic, H J Levingstein, R G Smith, "Curier temperature, birefringe, and phase-matching temperature variations as a function of melt stoichiometry", Appl. Phys. Lett., **12**, p 92, 1968.

[18] R L Byer, J F Yung, R S Feigelson, Growth of high-quality litium niobate crystals from the congruent melt" J Appl. Phy., **41**, p 2320, 1970.

[19] J E Midwinter, " Assesment of lithium meta-niobate for non-linear optics", Appl. Phys. Lett., **11**, p 128, (1967).

[20] J E Midwinter, "Lithium niobate: Effects of composition on the refractive indices & optical second harmonic generation", J Appl. Phys., **39**, p 3033, 1969.

[21] B H Turner, F R Nash, P M Bridenbaugh, "Dependence of linear electro-optic effect &dielectric constant on melt composition in lithium niobate", J Appl. Phys., **41**, p 5278, 1970.

[22] R C Miller and W A Norland, "Dependence of second harmonic generation coefficients on LiNbO3 composition, J Appl. Phys., **42**, p 4145, 1971.

[23] Standards on piezoelctric crystals, 1949, Institute of Radio Engineers, New York, **49 IRE 14**

[24] J T Milek and M Neuberger, "Linear Electrooptic modular materials", IFI/Plenum Data Corporation, 1972.

[25] L M Guseva et al, "Investigation of some of the optical Characteristics of Ferroelectric lithium niobate", ACAD. OF SCI., USSR, Bull., Phys. ser., **31**, no. 7, pp. 1181--1183, 1967

[26] G D Boyd et al., "LiNbO3:An efficient phase matchable nonlinear optical material", Applied phys. letters, v. 5, no. 11, pp 234--236, 1964.

[27] W K Burns, P H Klein and E J West, J Appl. Phys., **50**, p 6175, 1989.

[28] M M Choy and R L Byer, "Accurate second-order susceptibility measurements of visible and infrared nonlinear crystals", Physical Review B, Vol. **14**, pp. 1693--1706, 1976.

[29] M. N. Armenise, "Fabrication techniques of lithium niobate waveguides", IEE proceedings, vol. **135**, Pt. J. No 2, pp. 85--91,April 1988.

[30]M. L. Borth and M. M. Fejer, "Annealed proton-exchange $LiNbO_3$ waveguides", Optics letters , vol. **16**, No 23, pp. 1844--18436, December 1991

[31] G Tartarini, P Bassi, P Baldi, M P De Micheli, and D B Ostrowsky, "Biaxial Characteristics of planar proton exchanged Lithium Niobate waveguides", Journal of lightwave technology, vol **15**, no 5, pp. 821--826, may 1997.

[32]Yi-Yan, A, "Index instability in proton exange LiNbO3 waveguides", Appl Phys Lett, 1983, **42**, pp 633-635.

[33] Yu N Korkishko, V A Fedorov, and M P De Micheli, "Anomalous refractive index change in proton exchanged $LiNbO_3$ waveguides after annealing"

[34] M L Borth, L A Eyres and M M Fejer, "Depth profiling of the d_{33} nonlinear coefficient in annealed protong exchange $LiNbO_3$ waveguides", Appl. Phys. Lett. Vol **62**, pp. 2012--2014, April 1993.

[35] A D McLachlan, "Theoretical and experimental investigations of titanium diffused lithium niobate optical waveguides", PhD Thesis, 1981, Gkasgow University.

[36] C E Rice, R J Holmes "A new rutile structure solid-solution phase in the LiNb3O8-TiO2 systems, and it's role in Ti diffusion into LiNbO3", J. Apll. Phys. vol 60, pp 3836--3839, December 1986.

[37] M N Armenise, C Canali, M De Sario, P Franzosi, J Singh, R H Hutchins and R M De La Rue, "Dependence of implane scattering levels in Ti:LiNbO3 optical waveguides on diffusion time", IEE proceedings, vol. **131**, Pt. H. No 5, pp. 295--298, Octiber 1984.

[38] M N Armenise, C Canali, M De Sario, A Carnera, P Mazzoldi, and G Celotti, "Characterisation of TiO2, LiNbO3O8 and (Ti0.65Nb0.35)O2 compound growth observed during Ti:LiNbO3 optical waveguide abrication" J Appl. phys., **54**, pp 6223--6231, 1983.

[39] R C Alfernes, V K Ramaswamy, S K Korotky, M D Divino, L Buhl, "Efficient single-Mode fiber to titanium diffused lithium niobate waveguide coupling for λ=1.32 μm", IEEE J Quantum elec., vol **QE-18**, No 10, pp 1807--1813, 1982.

[40] M Fukuma and J Noda, " Optical properties in titanium-diffused LiNbO3 strip waveguides and their fiber coupling-to-a-fibre characteristics", Appl. Opt., 19, pp 591--597 , 1980.

[41] J L Jakel, A M Glass G E Peterson, C E Rice, D H Olson and J J Veselka, "Damage resistant LiNbO3 waveguides", J Apll. Phys. Vol **55**, pp 269--270, January 1984.

[42] O Eknoyan, A S Greenblatt, W K Burns, and C H Bulmer, "Characterisation of Ti:LiNbO3 deep waveguides diffused in dry and wet oxigen ambient", Appl. Opt. vol. **25**, pp. 737--739, 1986.

[43] B Shuppert, "Experimental investigation of outdiffusion in LiNbO3-substrates", Proceedins of the Fourth European conference on Integrated optics, ECIO 87, Gasgow, 1987.

[44] S. Fouchet, A. Carenco, C. Daguet, R. Guglielmi, and L. Riviere, "Wavelength Dispersion of Ti Induced Refractive Index Change in Ti:$LiNbO_3$ as a function of Diffusion Parameters", Journal of Lightwave technology, **LT-5**, pp. 700 - 708 (1987).

[45] J C Chon, W Feng, and A R Mickelson. "Photorefractive damage thresholds in Ti:LiNbO3 channel waveguides.", Applied optics, vol **32**, No 36, pp. 7572--7580, December 1993.

[46]T Fujiwara, S Sato and H Mori, "Wavelength depencence of photorefractive effect in Ti-indiffused LiNbO3 waveguides", Appl. Phys. Lett., **54**, pp. 975--977, March 1989.

[47] R A Becker "Methods of characterizong photorefractive susceptibility of LinbO3 waveguides", SPIE Proc. **578**, pp. 12-18, 1985.

[48] R V Schmidt, P S Cross and A M Glass "Optically induced crosstalk in LiNbO3 waveguides switches", J Appl Phys **51**, pp. 90--93, January 1980

[49]G T Harvey, "The photorefractive effect in dierectional coupler and Mach-Zehnder LiNbO3 optical modulators at a wavelength of 1.3 μm", J Lightwave Tech. **6** pp. 872--876, June 1988.

[50] A Ashkin, G D Boyd, J M DziedzicR G Smith, A A Ballman, J J Levinstein, and K Nassau, "Optically induced refractive index inhomogeneities in LiNbO3 and LiTaO3" Appl Phys Lett **9**, pp. 72--74, July 1966.

[51] R A Beckker R C Williamson, "Photorefractive effects in LiNbO3 channel waveguides:Model and experimental verification" Appl. Phys. Lett., **47**, pp. 1024-1026, November 1985.

[52] R L Holman and P J Cressman, Opt. Eng **21**, 1025, (1982)

[53] A M Glass, Opt. Eng **17**, 470 (1978)

[54] S Miyazawa, "Ferroelectric domain inversion in Ti-diffused LiNbO3 optical waveguide", J Appl Phys vol. 50, pp. 4599--4603, 1979.

[55] D Hoffman and U Langmann, "Diffused optical waveguides on the +c and -c face os c-plate LiNbO3 - Characteristic revealed by chemical etching", Proc. 1st Euro. Conf. Integrates Opt. London, England:iEE, 1981, pp 1--3.

[56] S Thaniyavarn, T. Findakly, D Booher, and J Moen,"Domain inversion effects in Ti-LiNbO3 integrated optical devices," Appl. Phys. Lett., Vo. **46**, pp. 933--935, 1985.

[57] J. C. Peuzin, "Comments on 'Domain-inversion effects in Ti-LiNbO3 integrated optical devices' ", Appl. Phy. Lett., Vol. 48, p 1104, 1986; also S. Miyazawa, "Response", Appl. Phys. Lett., Vol. **48**, pp. 1104--1105, 1986.

[57-b]S Miyazawa, "Esponse", Appl. Phys. Lett., Vol. **48**, pp. 1104--1105, 1986.

[58] N Ohnishi, "An etching study on a heat-induced layer at the positive-domain surface of LiNbO3", Japan J Appl. Phys., Vol **16**, pp. 1069--1070, 1977.

[59] K Nakamura, H Ando, and H Shimizu, "Ferroelectric domain inversion in LiNbO3 plates by heat treatment", Appl. Phys. Lett., Vol **50**, pp. 1413--1414, 1987.

[60] V V Antipov, A A Blistanov, N G Sorokin, and S I Chizhikov, "Formation of regular domain structure in the ferroelectric LiNbO3 and LiTaO3 near the phase transition", Sov. Phys. Crystallogr., **30**, pp. 428--430, 1985.

[61] M Tasson, H Legal, J C Gay, J C Peuzin, and F C Lissalde, "Piezoelectric study of poling mechanism in lithium niobate crystals at temperature close to the Curie point", Ferrolectrics, **13**, pp 479--481, 1976.

[62] I Camlibel, "Spontaneous polarization measurements in several ferroelectric oxides using a pulsed-field method", J Appl. Phys., **40**, pp 1690--1693,

[63] M Minakata, S Saito, M Shibata, and S Miyazawa, "Precise determination of refractive-index changes in Ti-diffused LiNbO3 optical waveguides", J Appli. Phys., Vol. **49**, pp. 4677--4682, 1978.

[64] H Ludtke, W Sohler, and H Suche, "Characterization of Ti:LinbO3 waveguides", in Dig. Workshop Integrated Optics, R T Kersten and R Ulrich, Eds., p 122, 1980.

[65] J Vollmer, J P Nisius, P Hertel, and E Kratzing, "Refractive index profiles of LiNbO3:Ti waveguides", Appl. Phys. A, Vol. **322**, pp 125--127, 1983.

[66] J Ctyroky, M Hofman, J Janta, and J Shcrofel, "3-D analysis of LiNbO3:Ti channel waveguides and directional couplers", IEEE J Quantum Electron, Vol. **QE-20**, pp. 400--409, 1984.

[67] G J Griffiths and R J Esdaile, "Analysis of titanium diffused planar optical waveguies in lithium niobate", IEEE J Quantum Electron, Vol. **QE-20**, pp. 149--159, 1984.

[68] W K Burns, P H Klein, E J West, and L E Plew, "Ti indiffusion in Ti:LiNbO3 planar and channel optical waveguies", J Appl. Phys., **50**, pp. 6175--61--82, 1989.

[69] M Fukuma, and J Noda, "Optical properties of titanium-diffused LiNbO3 strip waveguides and their coupling to a fiber characteristics", Appl. Opt., Vol. **19**, pp. 591--597, 1980.

[70] G B Hocker and W K Burns, "Mode dispersion in diffused channel waveguides by the effective index method", Appl. Opt. , vol **16**, pp. 113--118, 1977.

[71] R T Hawkins II and J H Goll, "Method for calculating coupling lengths of Ti:LiNbO3 waveguide directional couplers", Journal of Lightwave technology, Vol. **6**, pp. 887--891, 1988.

[72] E Strake, G P Bava, and I Montrosset, "Guided Modes of Ti:LiNbO3 channel waveguides: A novel quasy-analytical technique in comparison with the scalar finite-element method", Journal of lightwave technology, vol. **6**, no 6, pp. 1126--1135, 1988.

[73] J Webjorn, F Laurel and G Arvidsson, "Fabrication of periodically domain-inverted channel waveguides inLithium niobate for second harmonic generation", Journal of lightwave technology, 7, No. 10, pp 1597--1600, 1989.

[74] M Hove and P D Townsend, "An introduction to methods of periodic poling for second-harmonic generation", J Phys. D:Appl. Phys., 28, pp. 1747--1763, 1995.

3

Cut-off wavelength of periodically segmented waveguides in Ti:LiNbO3

The cut-off wavelength for Ti:$LiNbO_3$ periodic segmented waveguides (PSWs) with different duty cycles and of continuous waveguides has been measured for both polarisations. PSWs are described by an equivalent continuous waveguide and, using this model, a universal relationship between the cut-off wavelength of a PSWs with different duty cycles is proposed and verified experimentally. Using the Fabry-Perot method, PSWs with a duty cycle of 0.55 have been found to have a loss coefficient of 1.9 dB/cm, about 0.9 dB/cm greater than the loss coefficient of a continuous waveguide.

3.1. Introduction

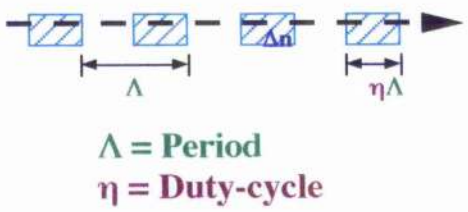

Fig 3.1. Schematic representation of a PSW.

In a PSW the increase in the refractive index (Δn) is modulated periodically during fabrication, this is shown schematically in Fig 3.1. As a consequence of the segmentation, the loss in the guide is increased and the effective refractive index is reduced when compared to a continuous waveguide. A PSW can be represented by an equivalent continuous waveguide with the same depth and width, in which the average index difference , Δn', is taken to be the average of the index along the direction of propagation, and in the case of step index waveguides is given by Eq. 3.1

$$\Delta n' = \eta \Delta n \qquad \text{Eq 3.1}$$

By choosing the duty cycle, η, Δn' can be spatially modified along the waveguide. The refractive index change determines the mode size, propagation constant and cut-off wavelength of the PSW.

The possibility of using Eq 3.1 to describe PSWs permits their study using existing tools for continuous waveguides. Thyagarajan et al. [1] showed that PSWs can be represented accurately by an equivalent continuous waveguide. However, no direct evidence was produced on the validity of Eq. 3.1. To establish the accuracy of Eq. 3.1, a measurable property of the waveguide has to be related to the increase in the refractive index. In this Chapter we propose using the cut-off wavelength, which is directly related to $\Delta n'$. If we want to verify Eq 3.1 using properties associated with the effective index, we require a good description of the index distribution in the waveguide as a function of the fabrication conditions, as well as an appropriate model to obtain the effective index from the index distribution.

Due to the diffusion nature of the Ti:$LiNbO_3$ waveguides, Eq 3.1 can only be used to describe PSWs for the case of weakly confined modes, where the mode size is larger than the diffusion length. And this is certainly the case near cut-off. This will be discussed in section 5.3.2. of Chapter 5.

Strip waveguides were fabricated in a z-cut $LiNbO_3$ substrate by titanium indiffusion. For this configuration the quasi-TM mode corresponds to the extraordinary ray (e-ray) and the quasi-TE mode corresponds to the ordinary ray (o-ray). The cut-off wavelength of the fundamental mode was obtained for different fabrication conditions, as a function of the duty cycle and period, for both polarisations.

In this Chapter, we report on PSWs fabricated in Ti diffused $LiNbO_3$ designed for operation in the 1.3 μm and 1.55 μm telecommunications windows. To predict the cut-off wavelength as a function of the duty-cycle, the approximation represented by Eq. 3.1 has been used to formulate a relationship between these two parameters. An experimental verification of this relationship has been produced. The reduction in the average increase of the refractive index ($\Delta n'$), results in a reduction in the cut-off wavelength. This reduction in the cut-off wavelength of the fundamental mode is important; firstly because we have to ensure that PSWs guide at the desired operating wavelength and secondly, because, in devices formed by PSWs with different duty cycles, e.g. tapers, the PSW section with the smaller duty cycle could be used as a low pass filter and/or as a polarisation filter.

The accuracy in the determination of the cut-off wavelength has been studied as a function of the different fabrication parameters as well as measurement conditions. This approach provides direct information on the considerations to be taken into account when using Eq. 3.1 to describe PSWs.

We have used the Fabry-Perot method to obtain the loss coefficient for PSWs and continuous waveguides.

3.2. Derivation of a relationship between the cut-off wavelength and the duty cycle of PSWs.

Cut-off of the fundamental mode is defined as the condition at which the effective refractive index of a waveguide is the same as the refractive index of the substrate [2, 3], implying that the mode size extends over the whole substrate [3]. This condition will occur for a specific free-space wavelength, refractive index distribution and dimension of the waveguide. For the case of PSWs and continuous waveguides fabricated under the same conditions, both have the same dimensions and any difference in the cut-off wavelength will be due to the variation in the increase of the refractive index, Δn_{PSW} for PSWs and Δn_{cont} for continuous waveguides.

3.2.1. Relationship between the cut-off wavelength of PSWs and continuous waveguides using the V numbers.

The relationship between the cut-off wavelength of PSW and continuous waveguides will be shown. Firstly for diffused slab waveguides (using the "V" number as defined by Hocker at al. [3]) and then it will be shown that we can extrapolate this result to channel waveguides (by using the relationship between their "V" numbers described in ref. [4]).

3.2.1.1. Case of diffused slab waveguides.

Firstly we shall consider the case of Ti:$LiNbO_3$ slab waveguides. A normalised frequency V can be defined as [3]

$$V = L_D \frac{2\pi}{\lambda}\left(n_{\max}^2 - n_s^2\right)^{1/2} \qquad \text{Eq 3.2}$$

Where n_{max} is the refractive index at the surface and it is assumed that the refractive index profile has a monotonic decrease from the maximum value, n_{max}, to the substrate index n_s. In the present context, n_{max} in a PSW is a weighted average of the maximum value in the diffused high-index regions and the substrate index n_s in the undoped substrate regions. L_D represents the diffusion depth of the titanium into the $LiNbO_3$ (which is the same for PSWs and continuous waveguides) and λ is the free-

space wavelength. A similar normalisation has already been employed to advantage in the analyses of slab guides with a step index profile [2, 5, 6] and with a diffusion profile [3, 4].

At cut-off the value of the normalised parameter V only depends on the asymmetry parameter [2]. For Ti:$LiNbO_3$ waveguides we assume the asymmetry parameter will approach infinity [2, 3, 4], and therefore, that the value of V at cut-off will be the same for both PSWs and continuous waveguides:

$$V_{PSW}^{cut-off} = V_{cont}^{cut-off} \qquad \text{Eq 3.3}$$

This effectively means that as n_{max} is reduced by changing the duty cycle in a PSW, the free space wavelength at which cut-off occurs is also reduced.

Expressing n_{max} as $n_{max}=n_s+\Delta n$, and assuming $\Delta n^2 << 2n_s\Delta n$, we obtain:

$$\left(n_{max}^2 - n_s^2\right) \approx 2n_s\Delta n \qquad \text{Eq 3.4}$$

Using the approximation of Eq 3.4 in Eq 3.2 we obtain the following expression for V:

$$V^2 = L_D\left(\frac{2\pi}{\lambda}\right)^2 2n_s\Delta n \qquad \text{Eq. 3.5}$$

where n_s and Δn are wavelength dependent. Then, for continuous waveguides at cut-off:

$$V_{cont}^2 = L_D 2\left(\frac{2\pi}{\lambda_{cont}}\right)^2 n_s(\lambda_{cont})\,\Delta n(\lambda_{cont}) \qquad \text{Eq 3.6}$$

where λ_{cont} is the cut-off wavelength for the continuous waveguide. Similarly for PSWs:

$$V_{PSW}^2 = L_D 2\left(\frac{2\pi}{\lambda_{PSW}}\right)^2 n_s(\lambda_{PSW})\,\Delta n'(\lambda_{PSW}) \qquad \text{Eq 3.7}$$

where λ_{PSW} is the cut-off wavelength for the PSW. As expressed in Eq. 3.1, the increase in the refractive index of a PSW is reduced due to the segmentation. Using Eq 3.1 we obtain:

$$\Delta n'(\lambda_{PSW}) = \eta \Delta n(\lambda_{PSW}) \qquad \text{Eq 3.8}$$

and using Eq. 3.8 with Eq 3.3, 3.6 and 3.7 we obtain

$$\frac{\lambda_{PSW}^2 n_s(\lambda_{cont}) \Delta n(\lambda_{cont})}{\lambda_{cont}^2 n_s(\lambda_{PSW}) \Delta n(\lambda_{PSW})} = \eta \qquad \text{Eq 3.9}$$

On the left hand side of Eq. 3.9, the term $\Delta n(\lambda_{cont})/\Delta n(\lambda_{PSW})$ accounts for the substrate dispersion and the term $n_s(\lambda_{cont})/n_s(\lambda_{PSW})$ for the Ti:$LiNbO_3$ dispersion. The remaining term, $\lambda_{cont}^2/\lambda_{PSW}^2$, can be used as a first approximation to relate the duty cycle and the cut-off wavelength of continuous waveguides and PSWs, i.e.:

$$\eta = \frac{\lambda_{PSW}^2}{\lambda_{cont}^2} \qquad \text{Eq 3.10}$$

3.2.1.2. Case of channel waveguides.

This result can be generalised to diffused channel (or stripe) waveguides using the relationship between the "V" number of a channel waveguide (V_c) with the "V" number of a slab waveguide (V) [4]. This relationship is expressed as

$$V_c = Vb\frac{W}{L_D} \qquad \text{Eq. 3.11}$$

Where W is the width of the Ti film before diffusion, L_D is the diffusion depth and b is the normalised mode effective index [4]. In the context of channel waveguides, n_{max} is related to the index distribution of a diffusion channel waveguide by the following relationship [4]:

$$n^2(x.z) = n_s^2 + (n_{max}^2 - n_s^2) f(z) g(x) \qquad \text{Eq. 3.12}$$

where f(z) and g(x) describe the diffusion profile in depth and laterally respectively.

Eq 3.11 indicates that for a given width and depth, the value of V_c depends only on V and b. Because b is a function of V [2, 3], it is clear that V_c is directly related to V. Then, at cut-off V_c is the same for PSWs and continuous waveguides, and the results for slab waveguides can be extrapolated to channel waveguides.

Then, at cut-off V_c is the same for PSWs and continuous waveguides, and the results for slab waveguides can be extrapolated to channel waveguides.

3.2.2. Relationship between the cut-off wavelength of PSW and continuous waveguides using the transversal propagation constant.

In this section we will show how we can arrive at the results of the previous section by using the transversal propagation constant k_t instead of the "V" number. To simplify the model only the case of a step index channel waveguide is considered, where n_c is the refractive index in the channel and n_{eff} is the effective refractive index of the mode propagating through the waveguide ($n_s \leq n_{eff} \leq n_c$).

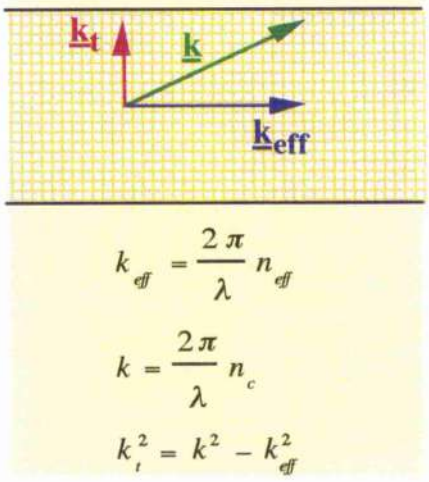

Fig 3.2. Direction and magnitude of the propagation constant for the light propagating in a waveguide

The transversal propagation constant k_t for the case of a step index waveguides is given by [6]: (see Fig 3.2)

$$k_t^2 = \left(\frac{2\pi}{\lambda}\right)^2 \left(n_c^2 - n_{eff}^2\right) \qquad \text{Eq. 3.13}$$

At cut-off the effective refractive index n_{eff} will be that of the substrate n_s. Therefore at cut-off the transversal propagation constant will be

$$k_t^2 = \left(\frac{2\pi}{\lambda}\right)^2 \left(n_c^2 - n_s^2\right) \qquad \text{Eq. 3.14}$$

Using the approximation of Eq 3.4 the transversal propagation constants at cut-off for continuous waveguides and PSWs are respectively:

$$k_{cont}^2 = 2\left(\frac{2\pi}{\lambda_{cont}}\right)^2 n_s(\lambda_{cont})\,\Delta n(\lambda_{cont}) \qquad \text{Eq. 3.15}$$

and

$$k_{PSW}^2 = 2\left(\frac{2\pi}{\lambda_{PSW}}\right)^2 n_s(\lambda_{PSW})\,\Delta n'(\lambda_{PSW}) \qquad \text{Eq. 3.16}$$

same for all continuous and periodic segmented step index channel waveguides, at cut-off they have the same transversal propagation constant.

$$k_{PSW}^{cut-off} = k_{cont}^{cut-off} \qquad \text{Eq. 3.17}$$

Now, using Eq. 3.15, 3.16, 3.17 and Eq. 3.8 we re-obtain the result of Eq. 3.9 and 3.10. This result for step index channel waveguides can be extrapolated to diffused channel waveguides.

3.2.3. Relationship between the cut-off wavelength of PSWs of different duty cycles.

A continuous waveguide can be regarded as a PSW with duty cycle 1. If we substitute the continuous waveguide with a PSW, the results of Eq 3.9 and 3.10 (shown to be true for diffused channel waveguides) can be generalised to relate the cut-off wavelength of two PSWs with different duty cycles. This generalisation leads to:

$$\frac{\lambda_{PSW}^2(\eta_1)\, n_s\left(\lambda_{PSW}(\eta_2)\right) \Delta n\left(\lambda_{PSW}(\eta_2)\right)}{\lambda_{PSW}^2(\eta_2)\, n_s\left(\lambda_{PSW}(\eta_1)\right) \Delta n_{PSW}\left(\lambda_{PSW}(\eta_1)\right)} = \frac{\eta_1}{\eta_2} \qquad \text{Eq 3.18}$$

where $\lambda_{PSW}(\eta)$ is the cut-off wavelength of a PSW with duty cycle η. The approximation for the case where dispersion is not considered will be:

$$\frac{\eta_1}{\eta_2} \approx \frac{\lambda_{PSW}^2(\eta_1)}{\lambda_{PSW}^2(\eta_2)} \qquad \text{Eq 3.19}$$

Rearranging Eq 3.19 the following expression is obtained:

$$\frac{\eta_1}{\lambda_{PSW}^2(\eta_1)} = \frac{\eta_2}{\lambda_{PSW}^2(\eta_2)} \qquad \text{Eq 3.20}$$

This simple expression relates the cut-off wavelength of two PSWs with different duty-cycles.

3.3. Ti-diffused $LiNbO_3$ waveguide fabrication.

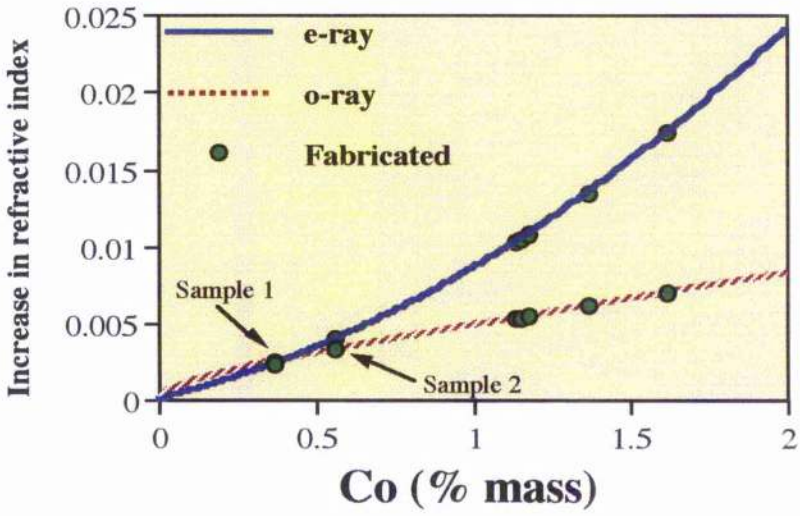

Fig 3.3. Increase of the refractive index at 1.3 μm for e-ray and o-ray as a function of the Ti concentration in percent in mas [21]. The points indicate the maximum possible increase in the refractive index for both polarisations for the fabrication conditions of Table 3.1.

Waveguides were fabricated by Ti-diffusion in a z-cut substrate of $LiNbO_3$. Standard photolithography techniques were used to pattern a layer of titanium evaporated onto the surface of the substrate. Once patterned, the titanium was in-diffused in a dry oxygen atmosphere by placing the sample in a furnace at 1050 °C, see Chapter 2. The thickness of the initial titanium layer and the diffusion time were both adjustable parameters in this investigation and are given in Table 3.1. One of the lithographic masks used gave continuous strip waveguides nominally 5 μm wide and PSWs also nominally 5 μm wide, with periods between 15.8 and 19.8 μm in 0.2 μm steps and a duty cycle of 0.5. The other mask contained continuous waveguides 4 μm wide and PSWs 4 μm wide with duty cycles varying from 0.35 to 0.65 in 0.05 steps with 19 μm periods. Some variation in the duty cycle across the mask as a consequence of photolithographic processing of the mask is to be expected. In this investigation we observed that flowing dry oxygen inhibited outdiffusion of Li_2O sufficiently to suppress slab guiding. For most of the fabrication conditions the increase in the refractive index due to Ti-indiffusion is larger for the e-ray than for the o-ray. Fig 3.3 shows the increase in the refractive index at the surface of a slab waveguide as a function of the Ti concentration [7]. The points in Fig 3.3 represent the expected values, assuming the diffusion times and Ti thickness given in Table 3.1. The difference in the increase of the refractive index between the o-ray (quasi-TE polarisation) and e-ray (quasi-TM polarisation) is responsible for the differences in their cut-off wavelengths.

Fig 3.4 shows the surface relief produce by the titanium after indiffusion. From this photograph we can have an idea of the titanium distribution of the PSWs after patterning and indiffusion.

	Ti thickness (nm)	Diffusion time (hours)	Cut-off wavelength o-Ray (μm)		Cut-off wavelength e-Ray (μm)	
			PSW	Continuous	PSW	Continuous
Sample 1	25	8	<0.6328	0.80	<0.6328	0.80
Sample 2	30	4.5	0.65	0.84	0.65	0.84
Sample 3	70	6	1.11	1.49	1.38	>1.64
Sample 4	80	5.45	1.02	1.33	1.32	>1.64
Sample 5	90	5	1.21	1.63	1.41	>1.64
Sample 6	100	12.40	1.55	>1.64	>1.64	>1.64
Sample 7	100	13:10	>1.64	>1.64	>1.64	>1.64

Table 3.1 Cut-off wavelength for both polarisation modes, for different fabrication conditions of $Ti:LiNbO_3$ channel waveguides. The lower limit in the cut-off wavelength is the wavelength of the HeNe laser, used to align the waveguides. The upper limit is given by the detector of the spectrum analyser. In the case of samples 1 and 2, the method could not be used to distinguish between the cut-off wavelength of the quasi-TE and quasi-TM modes because for these samples the cut-off wavelength is similar for both polarisation.

Fig 3.4. Photomicrograph (× 125) of a PSW of sample 7 in Table 3.1. The duty-cycle is 0.54. The observed contrast was contributed mainly by the surface relief related to the Ti indiffusion.

3.4. **Measurements.**

3.4.1. Transmission spectrum.

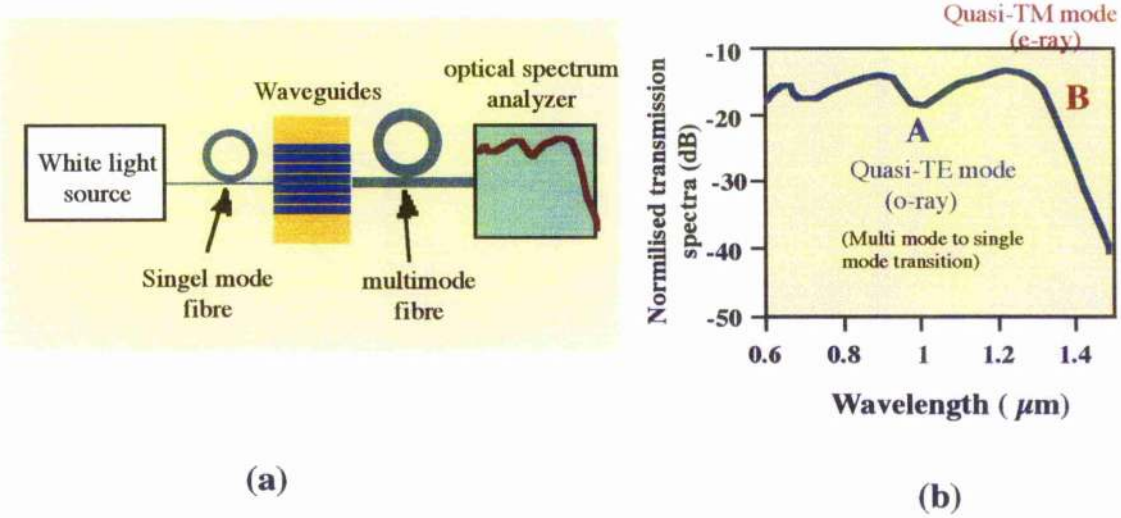

Fig 3.5. (a) Experimental set-up used to obtain the transmission spectra of PSWs. (b) Normalised transmission spectrum for the PSW of sample 4 of Table 3.1, with period 19.6 μm and duty-cycle 0.55.

To obtain the cut-off wavelengths, unpolarised white light was end-fire launched into the waveguide through a single mode fibre (at 1.55 μm), efficiently exciting all the modes in the waveguide and avoiding excessive coupling of light into the substrate. At the output, the light was collected in a multimode fibre, which was connected to an optical spectrum analyser, see Fig 3.5(a). The core of the output fibre, 50 μm diameter, did not permit the collection of significant levels of leakage light. A similar set up is described in Ref. [8]. The resolution of the spectrum analyser was chosen to be 5 nm and it was scanned between 632.8 and 1640 nm. To eliminate the spectral response of the white light source and the input and output fibres, we measured the spectrum of the whole system without the waveguides and used it as a reference, which later was used to normalise the spectrum of the waveguides. Fig 3.5(b) shows a typical example of the normalised transmission spectrum for a PSW (period 19.6 μm, duty cycle 0.55) of sample 4 in Table 3.1. We defined the cut-off wavelength of the more confined mode (e-ray in general) as the wavelength at which the transmission intensity dropped by 3 dB (point B in Fig 3.5(b)) after having attained its last maximum. The cut-off wavelength for the less confined mode (o-ray in general) is defined as the point at which the normalised transmission spectrum starts to rise again (point A in Fig 3.5(b)) after having obtained a minimum; when the less confined mode begins to radiate into the substrate the power in the spectrum will be reduced until all power in that polarisation has been dissipated, leaving the power in

the other polarisation. To verify this, both polarisations were end-fire launched into the samples, and with the help of a cross-polariser, the modes in each polarisation were investigated, see Fig 3.6.

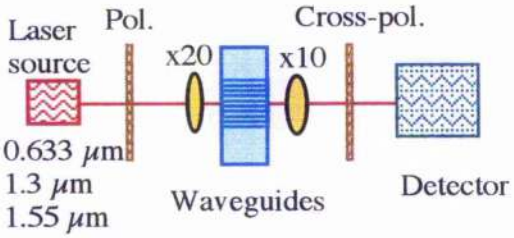

Fig 3.6. Experimental set up used to verify the polarisation sustained by the waveguide.

The general shape of the transmission spectrum shown in Fig. 3.5(b) depends on the overlap integral between the input field and the mode of the waveguide. The maximum transmission corresponds to a maximum value for the overlap integral. Here we assume small coupling losses between the waveguide and the multimode output fibre. The reduction in the transmission after the last maximum is due to the increase in the mode size. And because the transmission decreases rapidly with wavelength we know we are near cut-off. The segmentation losses are wavelength dependent [9], and therefore they affect the transmission spectrum of a PSW. But its overall contribution to the shape of Fig 3.5(b) is small and will not be considered in this analysis. This dispersion in the segmentation losses depends on the duty-cycle of the PSWs.

The definition of point B in Fig 3.5(b) as the condition for cut-off is a matter of choice. We decided to use this point because it is easy to obtain from the transmission spectrum. This definition is valid if the slop of the transmission spectrum, after the last maximum, is independent of the period or duty-cycle of the PSW. But this is not the case, and we were able to observe only a small variation on these slops. The rate of change in the transmission as a function of the wavelength increases as the cut-off wavelength decreases. There are two reasons for this, the first is due to the dispersion in the segmentation losses of a PSW, and its dependency on the duty-cycle. The second is related to the variation of the mode size with wavelength, for waveguides with the same dimensions but different cut-off wavelengths (or equivalently different increase in the refractive index). The latter can be verified for slab waveguides by analysing the variation of the effective guide thickness as a function of the V number near cut-off presented in reference [2]. The rate of increase in the effective guide thicknesses as a function of the wavelength increases as the cut-off wavelength decreases. The dimensions of the waveguides will have an effect in the transmission spectrum, but this is not of interest to us because we only compared waveguides fabricated under the same conditions, and therefore with the same dimensions. The influences on the variation on the slops of the transmission spectrum in our results will be discussed later.

3.4.2. Cut-off wavelength for PSWs and continuous waveguides for different fabrication conditions.

The cut-off wavelength of a Ti:$LiNbO_3$ waveguide depends on its dimensions (width and height) and on the increase in the refractive index due to titanium indiffusion (Δn_T). Table 3.1 shows the dependence on the cut-off wavelength for PSWs and continuous waveguides with the same width, but with different height and Δn_T. The cut-off wavelengths were obtained from spectra similar to those of Fig 3.5(b), and were cross-checked by measuring the polarisation at the waveguide output at 0.633 μm, 1.3 μm and 1.55 μm. In the case of diffused waveguides, the height of the waveguides is considered to be the diffusion depth, defined as:

$$L_D = 2\sqrt{D\,t} \qquad \text{Eq. 3.16}$$

where 'D' is the diffusion coefficient, which is a function of the diffusion temperature, and 't' is the diffusion time. All our samples were diffused at the same temperature and, therefore the height of the waveguides will only be a function of the diffusion time. The increase in the refractive index is a function of the Ti concentration, which will depend on the thickness of the Ti stripe before diffusion and the diffusion conditions. The effect of the diffusion time on the cut-off wavelength is not straight forward, as larger diffusion times imply lower Δn_T but larger diffusion depth. In general, for a given Ti thickness an increase in the diffusion time will result in a larger cut-off wavelength, since the effect on the increase in the diffusion depth dominates over the effect of the reduction in Δn_T.

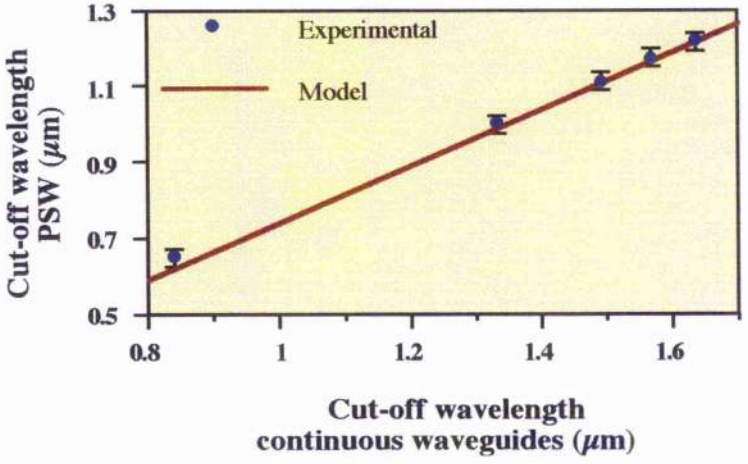

Fig 3.7 The points represent the cut-off wavelength of PSWs versus the cut-off wavelength of continuous waveguides for the waveguides of Table 3.1. The error bars (the same size as the diameter of the points) reflect the dispersion in the results to be shown in Fig 3.8 and 3.9. The continuous line corresponds to the theoretical results represented by Eq 3.10 for a duty cycle of 0.55.

To test the model present in section 3.2. for different fabrication conditions we have studied the relationship between the cut-off wavelength of PSWs of duty cycle 0.55 (in the ferric oxide mask) and continuous waveguides (PSWs with a well-defined duty-cycle of 1) for different fabrication conditions (see Fig. 3.7). The advantage of using continuous waveguides is that the duty-cycle is known precisely and therefore Eq. 3.10 can relate the cut-off wavelength of both waveguides to the duty cycle of the PSW, thus providing us with the possibility of quantitatively verifying the accuracy of our model. This has be done in Fig 3.7, where the points correspond to the experimental results for the quasi-TE mode, and the line corresponds to the theoretical results obtained from Eq 3.10 for a 0.55 duty-cycle. The error bars reflect the dispersion in the results that will be presented in Fig 3.8 and Fig 3.9, similar in both cases.

3.4.3. Cut-off wavelength as a function of the period of PSWs.

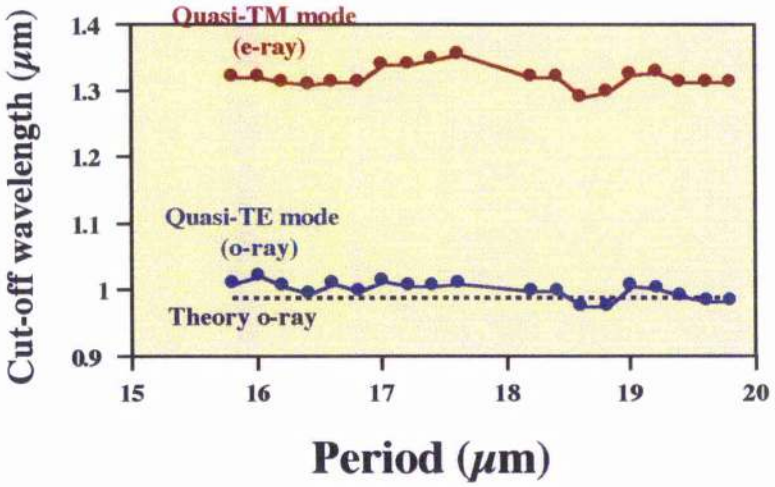

Fig 3.8. Cut-off wavelength of Ti:$LiNbO_3$ channel PSWs as a function of the period, for both quasi-TE and quasi-TM modes. The points correspond to the measured values and the discontinuous line to the theoretical results obtained with Eq 3.10 for 0.55 duty-cycle. The waveguides are those of sample 4 in Table 3.1. The duty cycle varies depending on the position of the waveguide in the sample, its values were measured to be between 0.54 to 0.57.

Using spectra such as the one of Fig 3.5(b), we were able to determine the cut-off wavelengths for the PSWs of sample 4 (Table 3.1) as a function of the period for both polarisations. The results can be seen in Fig 3.8. No dependence of the cut-off wavelength on the period could be observed. The cut-off wavelength for the quasi-TM polarisation deviates by ±30 nm around an average of 1321 nm. For the quasi-TE polarisation the cut-off wavelength deviates by ±23 nm around an average of

1000 nm. The variations of the cut-off wavelength appear to be a function of the position of the waveguide on the sample. All measurements were carried out on the same day, with the same fibres and same alignment conditions. Under these conditions, variations in coupling can account for up to 10 nm variation in the estimated cut-off wavelength for both the quasi-TE and quasi-TM polarisations. The largest variations in the estimated cut-off wavelength appear to be due to variations in the waveguide dimensions across the lithographic mask. The measured values for the duty-cycle in the mask went from 0.54 to 0.57 (nominal duty-cycle 0.50), sufficient to account for the dispersion of the data in Fig 3.8. In our case the pattern transfer from the mask to the sample does not appear to play a significant role in the final value of the duty cycle of the PSWs.

3.4.4. Cut-off wavelength as a function of the duty-cycle of PSWs.

Eq 3.15 indicates that the cut-off wavelength squared has a linear dependence on the duty cycle. The slope will depend on the fabrication conditions and, for zero duty cycle, zero cut-off wavelength would be expected. Fig 3.9 was obtained to assess the accuracy of these statements. Here the PSWs are 4 μm wide and their period is 19 μm. The duty-cycle in Fig 3.9 is that measured on the mask. As expected, these points form a straight line, but this line does not intersect the x axis at zero. In Fig 3.9(a) the cut-off wavelength for a given duty-cycle was obtained for different waveguides, the spread in the data is due to measurement errors and to small fluctuations in the dimensions (duty cycle, width and Ti concentration) of the waveguides.

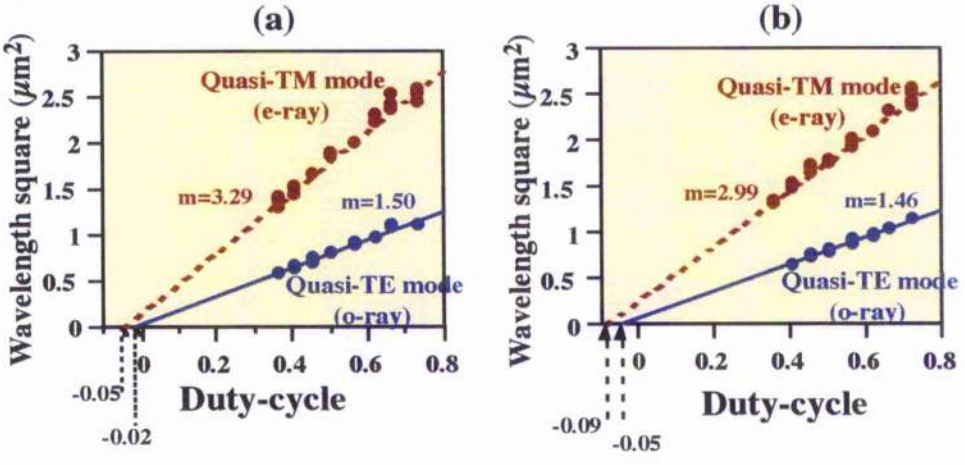

Fig 3.9. Square of the PSW cut-off wavelength as a function of the actual duty cycle on the mask used to pattern the PSWs, for the quasi-TM mode and the quasi-TE mode. 4 μm wide and 19 μm period PSWs were fabricated by patterning 80 nm thick films of Ti and diffusing at 1050°C for 12 hours. The lines are the regression lines of slop "m". Graphs (a) and (b) corresponds to the same waveguides for different alignment conditions.

To study the influence of different alignment conditions on the measurement of the cut-off wavelength presented in Fig 3.9(a), the same set of waveguides was measured again after the sample was removed and cleaned, the coupling fibres were also cleaned and the set-up was realigned. These new results can be seen in Fig 3.9(b). Variations in the estimated cut-off wavelength for the same waveguide were typically about 30 nm for the quasi-TM mode and 20 nm for the quasi-TE mode.

Despite the alignment conditions, in Fig 3.9 and 3.10 the line corresponding to the quasi-TM mode always intersects the x axis further away from zero than the line of the quasi-TE mode. This may be due to the criteria used to define cut-off for both modes. In the case of the more confined mode (quasi-TM), cut-off occurs when the mode is larger than a certain value, and therefore the coupling power from the input fibre to the waveguide is reduced by 3 dB. The definition of cut-off for the less confined mode (quasi TE) involves certain relationships between the mode sizes of the two polarisations.

As already mentioned, the rate of change in the transmission spectrum after the last maximum increases with the duty-cycle. Therefore, a different definition of cut-off, say a 6 dB reduction of the transmission intensity instead of 3 dB, will modify the slop of the quasi-TM mode of Fig 3.9, so that the line cuts the x-axis closer to zero.

3.4.5. Loss coefficient of PSWs and continuous waveguides.

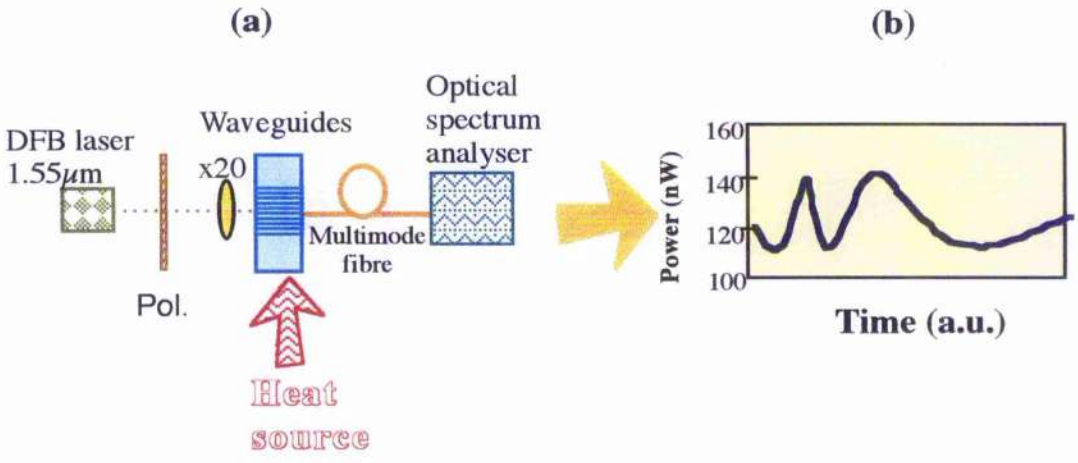

Fig 3.10. (a) Experimental set-up used to measure the loss coefficient of Ti:$LiNbO_3$ waveguides by the Fabry-Perot method as described in ref. [10]. (b) Transmitted intensity versus time (the temperature of the sample is a function of time), which can be seen as the resonator transmission versus the optical phase difference ($2\beta L$, β = propagation constant, L= length of the resonator), which in this case is a function of the temperature.

The Fabry-Perot method [10] has been used to measure the loss coefficient in both PSWs and continuous waveguides fabricated under the same conditions. The losses were measured using a 1550 nm DFB laser on the waveguides of sample 6 in Table 3.1. The experimental set-up can be seen in Fig 3.10. For the continuous waveguides the estimated loss coefficient is 1.0 dB/cm while for PSWs the estimated loss coefficient is 1.9 dB/cm. This method yields the upper limit of the waveguide attenuation coefficient. If the waveguides are not perpendicular to the facets or if imperfections are introduced by polishing, the actual attenuation coefficient can be smaller than the measured value .

3.5. Discussion.

$Ti:LiNbO_3$ waveguides are asymmetric, and therefore do not guide at all wavelengths. For a given waveguide there is a certain wavelength above which the light is radiated into the substrate, this is the cut-off wavelength. Due to the birefringence of the $Ti:LiNbO_3$ in a z-cut crystal, the two different polarisations will have different cut-off wavelengths. These considerations determine whether, at a given wavelength, the device will operate in one polarisation, both polarisations or none. The cut-off wavelength in stripe waveguide depends on the width, height and increase in the refractive index of the waveguide. But new considerations arise when studying PSW; the increase in the refractive index will be smaller due to the reduction in the average concentration of Ti along the waveguide. Fig 3.7, Fig. 3.8 and Fig 3.9 have shown that this reduction in the increase of the refractive index is as given by Eq. 3.1, and furthermore they show that a simple relationship (Eq 3.20) can be established between the cut-off wavelength and the duty cycle of two PSWs. This relationship, together with Table 3.1, provides us with a wide range of PSWs operating at different wavelengths. In particular, we have been able to fabricate PSWs that will operate in the 1.3 μm and 1.55 μm telecommunication windows.

There are three sources of error that affect the estimated value of the cut-off wavelength. First, there is the fabrication error, where photolithographic processing produces changes in the duty-cycle and in the width of the PSWs. Other fabrication errors are associated with the uneven thickness distribution of the titanium strips before diffusion. The second source of errors is measurement error, associated with the alignment of the set-up. Finally, there is an uncertainty in the criteria chosen to determine the cut-off wavelength from the transmission spectrum.

Increments of the duty cycle due to photolithographic processing were measured to be up to 6% and dependent on the position of the waveguide in the sample. This was taken into consideration in Fig 3.7 and Fig 3.8.

Two different measurements for the same alignment conditions carried out at different times (e. g. in the range between 30 seconds and half an hour) produced no significant change in the spectrum of the waveguide. Differences in alignment can produce a significant change in the estimated cut-off wavelength, of about 20 nm for the quasi-TE mode and 30 nm for the quasi-TM mode. Variations in the cut-off wavelength as a function of the position of the waveguides across the sample were found to be about 46 nm for the quasi-TE mode and 60 nm for the quasi-TM mode.

Point A in Fig 3.5(b) determine the cut-off conditions for the less confined mode, while point B determines the cut-off condition for the more confined modes. Because the criteria are different, it is not surprising that the point of intersection with the x-axis of the lines of Fig 3.9 differs for the two modes. It is easy to believe that the definition represented by points A in Fig 3.5(b) better portrays the behaviour of the cut-off wavelength as a function of the duty-cycle. At this point, virtually no energy from the less confined (quasi-TE) mode is maintained in the waveguide, unlike for the case of point B. This is consistent with the results of Fig 3.9, where the point of intersection with the x-axis for the quasi-TE mode is closer to zero; the expected value.

Our model predicts no dependence of the cut-off wavelength on the period, and this can be seen in Fig 3.8. The model predicts a linear relationship between the square of the cut-off wavelength and the duty cycle, which is supported by Fig 3.9. The accuracy to which the model can be used can be obtained from Fig. 3.7, Fig 3.8 and Fig 3.9. In Fig. 3.9, the point of intersection with the x-axis for the case of the quasi-TE mode (with better criteria for cut-off, and smaller measurement errors) is 0.02. Our model predicts it to be zero and the error indicates that Eq. 3.1 can be used to describe the increase of the refractive index of PSW with an error of 2% . Using the same argument for Fig 3.10 we obtain that the error is 5 %. The difference between these two values is purely due to measurement errors. If we relax the statistics slightly, and obtain the mean value and deviation with only two points, we can say that our model has an error of 4% ± 3%. The dispersion of the data in Fig. 3.7 and Fig 3.8 around the theoretical predicted value indicates similar accuracy.

3.6. **Conclusions.**

We were able to fabricate PSWs for different fabrication conditions, with duty cycles ranging from 0.3 to 0.65, and periods ranging from 15 μm to 20 μm. In all cases the model represented by Eq 3.1 has been proved to describe the behaviour of PSWs successfully. We were able to measure the cut-off wavelength of PSWs and, using a simple model, predict its variation with the duty-cycle. Agreement between the model and the experimental results is excellent, which indicates that Eq. 3.1 describes the properties of the PSWs (except loss) very accurately.

3.7. References.

[1] K. Thyagarajan, C. W. Chien, R. V. Ramaswamy, H. S. Kim, and H. C. Cheng, "Proton-exchange periodically segmented waveguides in $LiNbO_3$ ", Opt. Lett. **19**, pp. 880 - 882, (1994).

[2] H. Kogelnik and R. V. Ramaswamy, "Scaling Rules for Thin-Film Optical Waveguides", Applied Optics, **13**, pp. 1857-1862, (1974).

[3] G. B. Hocker, and W. Burns, "Modes in Diffused Optical Waveguides of Arbitrary Index Profile", IEEE Journal of Quantum Electronics, **QE-11**, pp. 270 - 276, (1975).

[4] G. B. Hocker and W. K. Burns, "Mode dispersion in diffused channel waveguides by the effective index method", Applied Optics, **16**, pp. 113 - 118, (1977).

[5] A. W. Snyder and R. M. De La Rue, "Asymptotic solution of Eigenvalue Equations for Surface Waveguide Structures", IEEE Transactions on Microwave Theory and Techniques, **MTT-18**, pp. 650 - 651, (1970).

[6] W. W. Anderson, IEEE J. Quantum Electron. **QE-1**, 2289 (1965)

[7] S. Fouchet, A. Carenco, C. Daguet, R. Guglielmi, and L. Riviere, "Wavelength Dispersion of Ti Induced Refractive Index Change in Ti:$LiNbO_3$ as a function of Diffusion Parameters", Journal of Lightwave technology, **LT-5**, pp. 700 - 708 (1987).

[8] T. Lang, L. Thevenaz, Z. B. Ren, and Ph Robert, "Cut-off wavelength measurements of Ti:$LiNbO_3$ channel waveguides", Meas. Sci. Technol., **5**, pp. 1124 - 1130, (1994)

[9] Z. Weissman and A. Hardy: "Modes of Periodically Segmented Waveguides", J. Lightwave Tech., 1993, **11**, pp. 1831-1838.

[10] R Regener and W Sohler, "Loss in Low-Finesse Ti:$LiNbO_3$ Optical Waveguide Resonators", Appl. Phys. B, 36, pp. 143--147, (1985)

4

Optical field distribution and losses in PSWs (Modes of PSWs)

A Three Dimensional Explicit Finite Difference Beam Propagation Method (3D EFD-BPM) has been used to study the modal characteristics and losses of Periodic Segmented Waveguides (PSW). Results for the variation of the mode width and depth, as a function of the duty cycle and period, are presented and compared with those obtained using the equivalent continuous waveguide model at a wavelength of 1.55 μm. The radiation losses associated with the modulation of the refractive index are studied and we show that a 3D representation of a PSW is necessary to evaluate the radiation loss.

4.1. Introduction.

In this Chapter we are going to use the EFD-BPM [1] to study the optical field of step index periodic segmented waveguides (PSW) with a index distribution chosen to resemble that of Ti:$LiNbO_3$ channel waveguides. We will show that the EFD-BPM can be used in the study of PSWs and we will show the behaviour of the optical field along the direction of propagation. One key difference between PSW and standard continuous waveguides is in the definition of a mode. A waveguide mode is normally associated with a field distribution which remains unchanged along the direction of propagation. However, in the case of a PSW the mode shape changes periodically as a function of distance. It is important to be able to understand the behaviour of these "quasi-modes" and to be able to account for radiation losses associated with the periodic modulation in refractive index. To that effect we used a 3D BPM.

EFD-BPM was used because the method is very efficient per propagation step, and the propagation step used for this structures is much smaller than that required to make the algorithm stable [1].

First, in section II we are going to state the Fresnel equation (the wave equation that has been numerically solved by our BPM), and indicate all assumptions and limitations involved. In section III we are going to obtain the explicit finite difference implementation of the Fresnel equation, and discuss the conditions for stability and on the boundary conditions. In section IV we are going to study the PSWs using the 3D EFD-BPM; we will study the variation of the optical field as it propagates through the PSW, the variations of the mode size as a function of the duty cycle and period, and we will obtain the losses associated with the segmentation. Then we will conclude.

4.2. Fresnel equation

Starting from the Maxwell equations and using a number of approximations:

1 $\underline{E}(x,y,z,t) = \underline{E}^{\omega}(x,y,z)\exp(-i\omega t)$

2 $E = \psi(x,y,z)\exp(-ik_r z)$

3 Disregard the polarisation properties of the waveguide [2]

4 A non conducting medium

5 Slow longitudinal variation:

$$k_r \frac{\partial \psi}{\partial z} \rangle\rangle \frac{\partial^2 \psi}{\partial z^2}$$

$$k_r^2 \frac{\partial \psi}{\partial z} \rangle\rangle \frac{\partial^2 \psi}{\partial z^2}$$

We obtain the Fresnel equation:

$$-2jk_0 n_r \frac{\partial \psi}{\partial z} + \frac{\partial^2 \psi}{\partial x^2} + \frac{\partial^2 \psi}{\partial y^2} = -k_0^2\left(n^2(x,y,z,\omega) - n_r^2\right)\psi \qquad \text{Eq 4.1}$$

Where n(x,y,z,w) is the index distribution of the waveguide and k_0 is the free space propagation constant.

The Fresnel equation is an approximation of the Helmholtz equation, which in turn is an approximation of a vectorial wave equation resulting from Maxwell equations. The derivation of the Fresnel equation from Maxwell equations can be seen in Appendix 2 .

4.3. Formulation of the EFD-BPM

4.3.1. Finite difference.

To obtain a solution for the Fresnel equation we are going to use a finite difference scheme. There are three kinds of finite differences [3]:

Forward differences

$$\Delta_{+\tau}\psi(\tau,s) = \psi(\tau+\Delta\tau,s) - \psi(\tau,s) \qquad \text{Eq 4.2}$$

Backward differences

$$\Delta_{-\tau}\psi(\tau,s) = \psi(\tau,s) - \psi(\tau-\Delta\tau,s) \qquad \text{Eq 4.3}$$

Central differences

$$\delta_{\tau}\psi(\tau,s) = \psi\left(\tau+\frac{1}{2}\Delta\tau,s\right) - \psi\left(\tau-\frac{1}{2}\Delta\tau,s\right) \qquad \text{Eq 4.4}$$

When the central difference operator is applied twice we obtain the second order central difference

$$\delta_{\tau}^2\psi(\tau,s) = \psi(\tau+\Delta\tau,s) - 2\psi(\tau,s) + \psi(\tau-\Delta\tau,s) \qquad \text{Eq 4.5}$$

For first differences it is often convenient to use the double interval central difference

$$\begin{aligned}\Delta_{0\tau}\psi(\tau,s) &= \frac{1}{2}\left(\Delta_{+\tau}+\Delta_{-\tau}\right)\psi(\tau,s)\\ &= \frac{1}{2}\left[\psi(\tau+\Delta\tau,s) - \psi(\tau-\Delta\tau,s)\right]\end{aligned} \qquad \text{Eq 4.6}$$

By using the backward differences for the derivative in z in the Fresnel equation, the method becomes implicit. This is because the scheme involves more than one unknown value of the solution on the new propagation level z+Δz. The forward difference and the double interval central difference will result in a explicit method. The forward difference results in an instability for any Δz, while the double interval central difference is conditionally stable. Any method based on the central difference

requires the field distribution at the present and preceding step to calculate the field at the next step.

4.3.2. Explicit finite difference applied to the Fresnel equation.

To solve the Fresnel equation, a parabolic partial differential equation, we use the double interval central difference for the derivative in z

$$\frac{\psi(x,y,z+\Delta z)-\psi(x,y,z-\Delta z)}{2\Delta z}\approx\frac{\partial\psi(x,y,z)}{\partial z} \qquad \text{Eq 4.7}$$

and centred second difference for the second derivatives in x and y

$$\frac{\psi(x+\Delta x,y,z)-2\psi(x,y,z)+\psi(x-\Delta x,y,z)}{(\Delta x)^2}\approx\frac{\partial^2\psi(x,y,z)}{\partial x^2} \qquad \text{Eq 4.8}$$

$$\frac{\psi(x,y+\Delta y,z)-2\psi(x,y,z)+\psi(x,y-\Delta y,z)}{(\Delta y)^2}\approx\frac{\partial^2\psi(x,y,z)}{\partial y^2} \qquad \text{Eq 4.9}$$

using these approximation we obtain that the Fresnel equation satisfies

$$\begin{aligned}\psi_{ij}(z+\Delta z)=\psi_{ij}(z-\Delta z)+a_i^-\psi_{(i-1)j}(z)+a_i^+\psi_{(i+1)j}(z)\\+c_j^-\psi_{i(j-1)}(z)+c_j^+\psi_{i(j+1)}(z)+b_{ij}(z)\psi_{ij}(z)\end{aligned} \qquad \text{Eq 4.10}$$

where

$$\begin{aligned}a_i^+&=\frac{\Delta z}{jk_0n_r(\Delta x)^2}\\a_i^-&=\frac{\Delta z}{jk_0n_r(\Delta x)^2}\\c_j^-&=\frac{\Delta z}{jk_0n_r(\Delta y)^2}\\c_j^+&=\frac{\Delta z}{jk_0n_r(\Delta y)^2}\\b_{ij}(z)&=-a_i^--a_i^--c_j^--c_j^+-j\frac{k_0\Delta z}{n_r}\left(n_{ij}^2(z)-n_r^2\right)\end{aligned} \qquad \text{Eq 4.11}$$

$\psi_{ij}(z)$ and $n_{ij}(z)$ are the optical field values and the sampled refractive index values, respectively, at $x=x_i$, $y=y_j$ in the computational window, and $\Delta x=x_i - x_{i-1}$ and $\Delta y=y_j-y_{j-1}$. The propagation of the optical field in Eq 4.10, is explicit and straightforward since it involves multiplication of the input field with a very sparse matrix, which

makes the method very efficient. However, this algorithm is only stable under the condition [1]

$$\Delta z < 2k_o n_r \left\{ \frac{4}{\Delta x^2} + \frac{4}{\Delta y^2} + k_o^2 \left| n_{ij}^2 - n_r^2 \right|_{\max} \right\}^{-1} \qquad \text{Eq 4.12}$$

This condition assures power conservation as well as stability[1]

4.3.3. Boundary conditions.

To solve the Fresnel equation with the BPM, boundary conditions have to be implemented at the edges of the computational window. The computational window can be seen in Fig 4.1. At present the most popular boundary conditions are the transparent boundary conditions [4, 5] which allow the radiation to escape from the computational window without appreciable reflections. However, this boundary condition has not been implemented in a EFD BPM. Here we use a different approach. First we make the electric field zero at the boundaries (metallic boundary conditions), in this situation the optical field will be reflected at the boundaries of the computational window. To avoid these reflections reaching the waveguide, we force the field to pass through an aperture. This is done by making the electric field zero in a single propagation step in all computational windows except for an aperture. The edges of the aperture are positioned so that they are far away from the guiding mode. In this situation the aperture has a minimum influence in the optical field (see Fig 4.6).

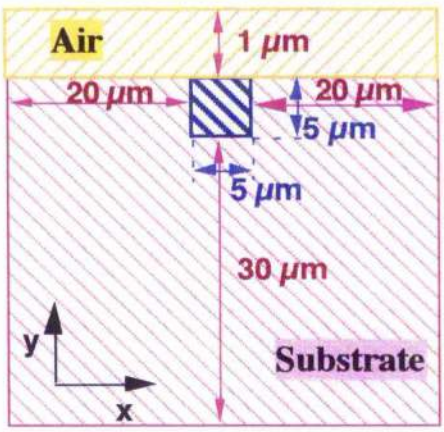

Nx=225 points
Ny=180 points

Δx=0.20 μm
Δy=0.22 μm
Δz=0.03 μm

(Δz *{to fulfil stability condition of Eq 23 }* = 0.06 μm)

n_{guide}=2.1587
$n_{substrate}$=2.1372
Δn=0.0215

Z direction of propagation.

Fig 4.1. Computational window used to simulate the propagation of light in a PSW using EFD BPM.

4.4. Analysis of PSWs using a EFD-BPM.

In a PSW the increase in the refractive index is modulated periodically. Each segment is composed of two regions with different refractive indices; a doped region, with an increase in the refractive index of Δn, and an undoped region with the same refractive index as the substrate. The modal properties of a PSW are determined by its dimensions, period (Λ), duty cycle (η) and the increase in the refractive index. In Chapter 3 have shown that the behaviour of a step index PSW can be approximated by a continuous waveguide with the same depth and width, in which the average index difference, Δn', is given by :

$$\Delta n' = \eta \Delta n \qquad \text{Eq 4.13}$$

This relationship has proved useful in the design of PSW; however, it does not provide information about the radiation losses associated with the modulation of the refractive index, or the behaviour of the optical filed along the direction of propagation.

4.4.1. Periodicity of the optical field; "Modes" of PSW.

The structure used in these BPM simulations was based on a 5 μm wide, step index PSW, with a period of 17.5 μm, guide index 2.1587, substrate index 2.1372 and with a range of duty cycles varying from 0.2 to 1. This geometry was chosen to approximate a single-mode PSW Ti indiffused $LiNbO_3$, where the maximum change in refractive index is ~0.02 [6]. Simulations were carried out at a wavelength of 1.55 μm. We used this relatively large refractive index modulation to reduce the mode size, and therefore the size of the computational window. A smaller increase in the refractive index will require excessively large computational times. The details of the computational window can be seen in Fig 4.1. The results from the BPM for a PSW of period 17.5 μm and duty-cycle 0.5 can be seen in Fig 4.2. Here we represent the intensity profile in the vertical and horizontal directions. The intensity profile in the vertical direction (the direction of the substrate) was calculated by adding all the intensity points in the transverse direction at a constant depth and is shown in Fig. 4.2(a). The intensity profile in the horizontal direction was calculated in a similar manner and is shown in Fig. 4.2(c). As can be seen, the periodic modulation of the refractive index forces a periodic modulation of the intensity distribution along the direction of propagation.

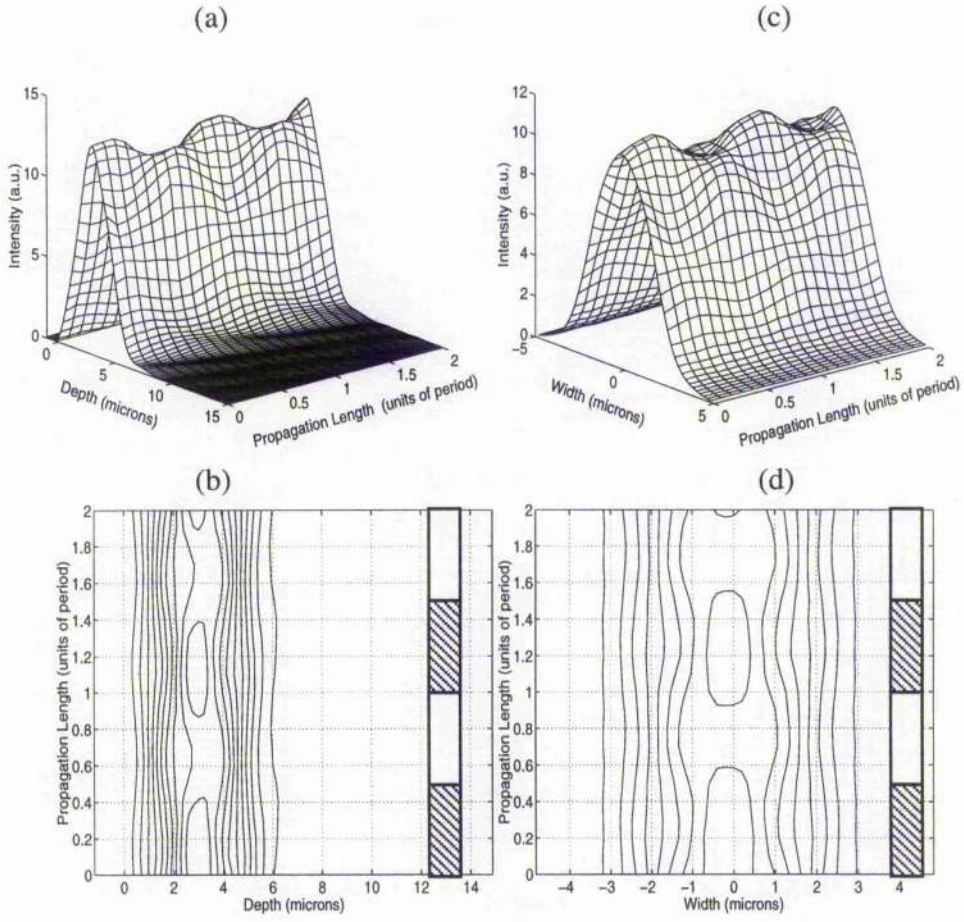

Fig 4.2. a) Depth intensity profile along 2 periods of a PSW and b) its contour curves. c) Horizontal intensity profile along 2 periods of a PSW and d) its contour curves. Period 17.5 μm, duty cycle 0.5, width 5 μm, depth 5 μm and an increase in the refractive index of 0.0215. Operating wavelength 1.55 μm. The period starts at the beginning of the doped region. Depth and width are the y and x coordinates of Fig 4.1 respectively.

To obtain the field distribution of Fig 4.2, the input field (a Gaussian) was allowed to propagate until the radiation modes that may exist in the input field disappear from the computational window, leaving only the propagating energy together with the segmentation losses. We found that to obtain the "mode" of a PSW, the step size in the direction of propagation has to be smaller than that given by the stability condition of Eq 4.12. The boundaries of the computational window were placed far away from the guide, so that they could not affect the propagating field distribution or the segmentation loss.

A mode exists when the optical field does not interfere destructively with itself when propagating in a waveguide. In the case of PSWs these conditions have to exist over a complete period, making the mode of a PSW a function of the transversal distribution of the refractive index as well as the longitudinal distribution of the refractive index (i.e. period and duty-cycle). Therefore, the field distribution of Fig 4.2 is the "mode" of PSWs, together with its radiation losses. From another point of view, the condition for the existence of a mode is that the transversal propagation constant is zero. i.e. the transversal propagation constant has the same magnitude in the opposite directions. In a PSW this condition is not fulfilled at any one point. However, after one period, the summation of all transversal propagation constants is zero, except for the radiation loss. Therefore, in the context of the latter definition, the radiation loss is not part of the "mode" of a PSW.

The conditions that determine the "mode" sustained by a PSW also determine the radiation losses. Therefore the cross section of the doped regions, the period and duty cycle determine the radiation losses.

The intensity distributions for PSWs with different duty-cycles are very different, not only in its mode size but also in the periodic distribution of the intensity. For the case of duty-cycle 0.5, the variation in the mode width and depth along one period is larger than for the PSWs with duty-cycle 0.2 or 0.8 (Fig 4.3). Later we will see how this can affect the radiation losses.

Fig 4.2(d) shows how the light in the horizontal direction converges when travelling throught the areas with the higher refractive index, and diverges when passing through the areas in between. Fig 4.2(b) shows that, due to the strong asymmetry, the light in the vertical direction bends away from the surface when passing throught the undoped regions. The radiation losses originate at the transition between the low refractive index region and the doped segment. The energy expands into the non doped region in such a way that, when it reaches the interface with the doped region, part of the energy can not be re-confined by the guide, while at the transition from the doped to the non-doped region, the mode is free to expand adiabatically and thus there are no radiation losses.

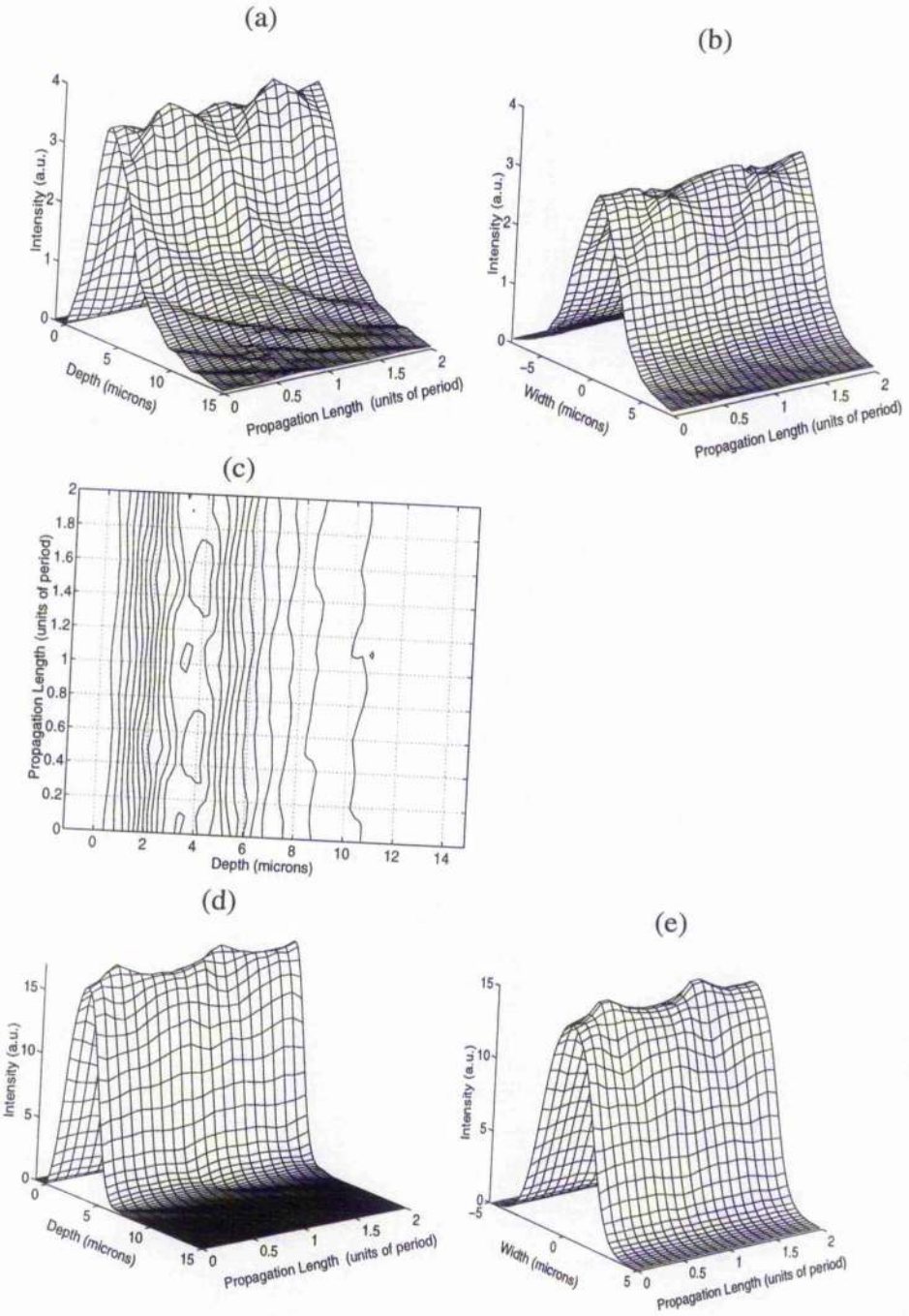

Fig 4.3. Depth intensity profile along 2 periods of a PSW of duty cycle 0.2 (a)-(c) and 0.8 (d)-(e). The waveguides have the same dimensions, and increase in the refractive index as that of Fig 4.1. Operating wavelength 1.55 μm.

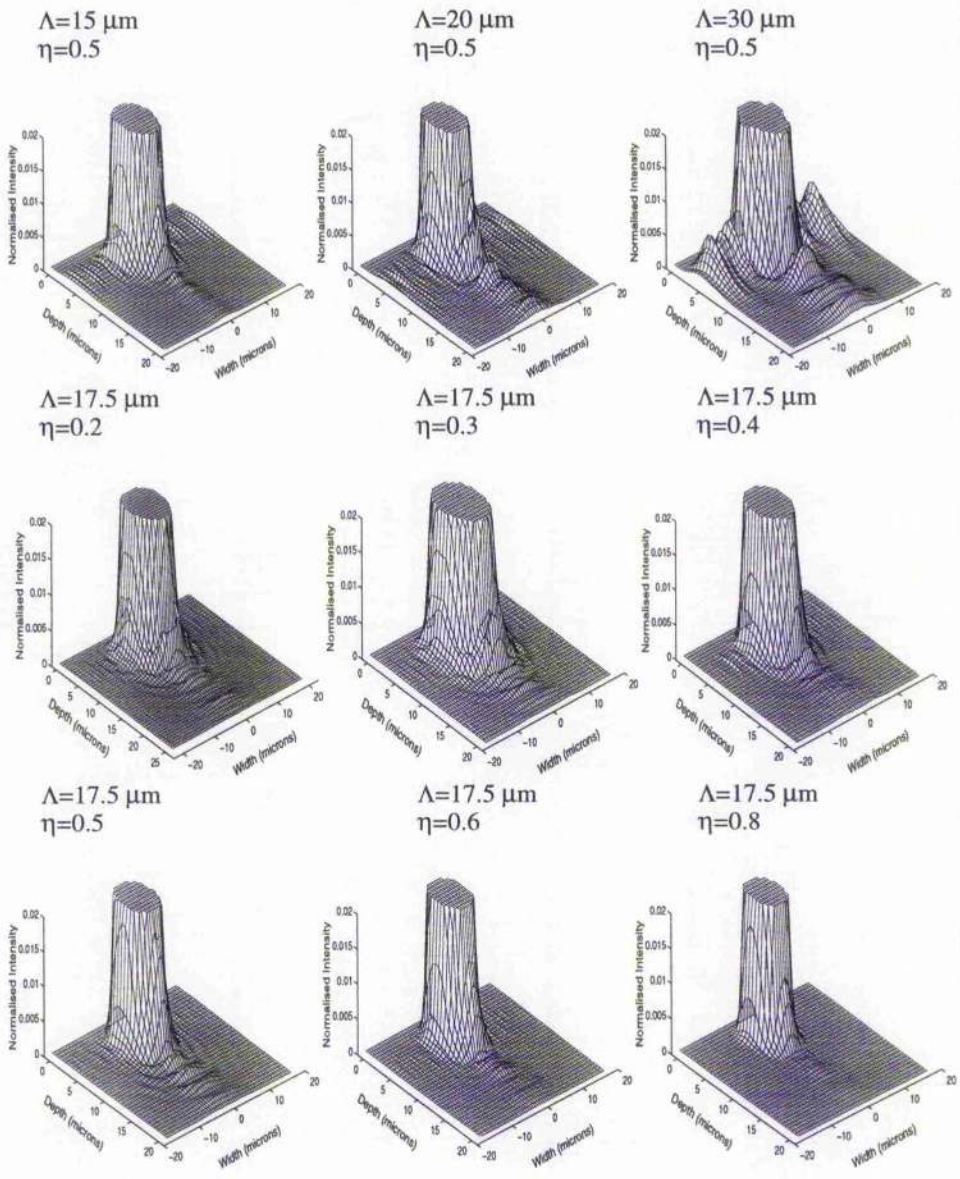

Fig 4.4. A three-dimensional view of the intensity propagating in the plane normal to the direction of propagation for PSWs with different periods and duty-cycles. The intensity has been obtained at the beginning of a doped segment and has been normalised to one, and then truncated at 2 % of the maximum.

4.2.2. Segmentation losses.

Figure 4.4 shows a surface plot of the optical field in the transversal plane to the direction of propagation, from which the details of the radiation loss can be seen. In some cases, the radiation spreads towards the boundaries with most of the radiation directed under the guides, and only a very small fraction spreads laterally. But on some occasions (Fig 4.4, Λ=30 μm, η=0.5), a considerable amount of light is radiated laterally. For this reason a 3D BPM is essential to study the radiation losses and the modal properties of PSWs. The advance of the energy radiated toward the substrate, as the light propagates along one period, can be seen in Fig 4.5. The marked region is the radiation loss produced in one period.

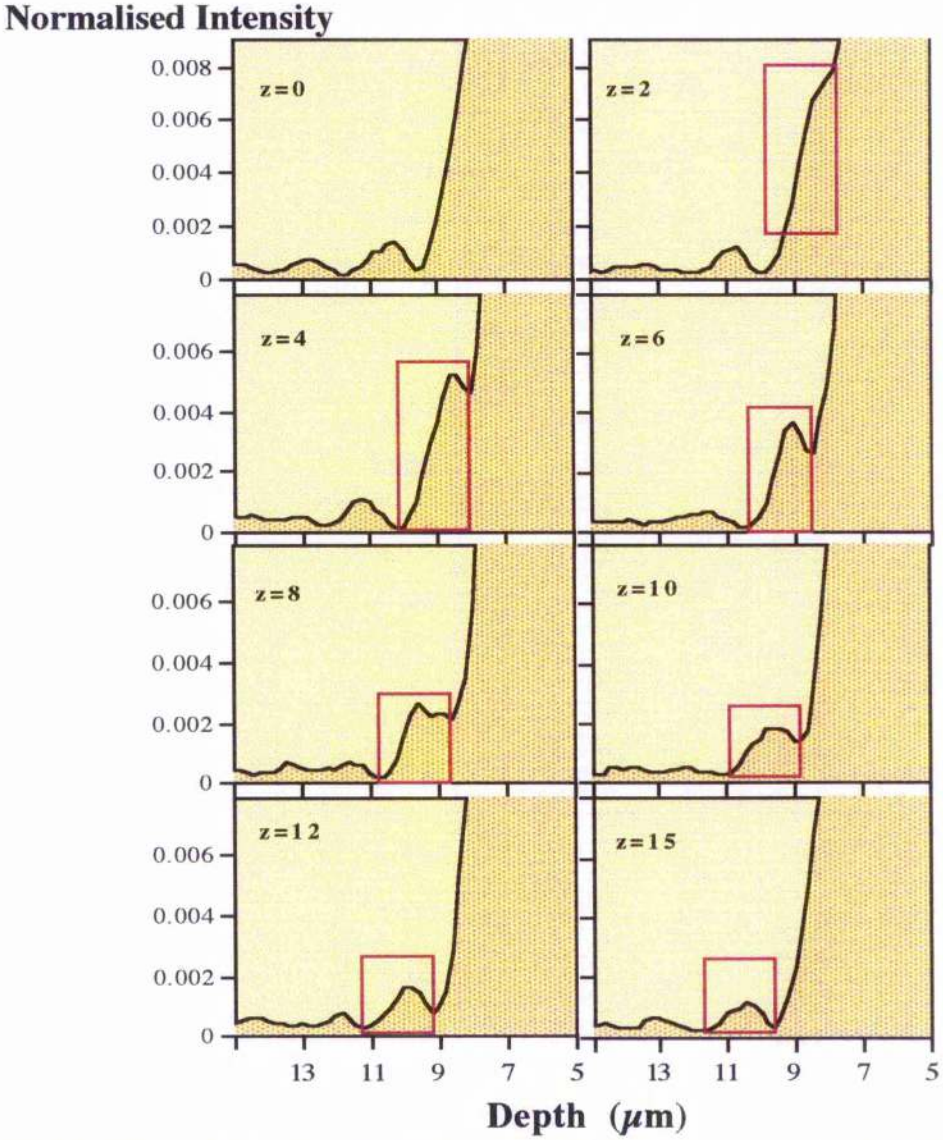

Fig 4.5 Normalised depth intensity profile for a PSW of period 15 μm and duty-cycle 0.5. Here we can see the segmentation losses in the direction of the substrate. The marked region follows the progression of the loses generated at one period.

In Fig 4.2, 4.3, 4.4 and 4.5, we can observe how the radiation losses exit the waveguide, but provide us with no information about the magnitude of these radiations. Fig 4.5 shows the progress of the segmentation loss towards the substrate along one period. But to obtain the losses from Fig 4.5 is difficult; The losses are not easy to isolate from the "mode" of the PSW, or from the losses generated by previous periods.

Weissman et. al in ref. [7] used a 2D BPM to study the radiation losses, they used the modal spectrum of the waveguide to obtain the radiation losses. They justified the use of a 2D BPM, arguing that most of the radiation loss takes place towards the substrate. As we show in Fig 4.4, this is not always the case. For this reason we studied the radian loss in all directions, and since the PSWs modes vary periodically we preferred not to use the modal spectrum.

4.4.2.1. Measurement of the segmentation losses.

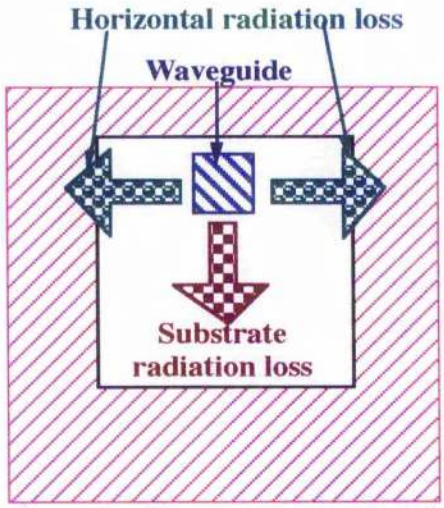

Fig 4.6. Here we can see the computational window used to obtain the segmentation losses of the PSW. The waveguide radiates energy horizontally and towards the substrate. To measure the losses we forced the optical field to zero in the shaded area, and then we measured the energy that enters this zone as the light propagates.

To obtain the segmentation loss we forced the electric field to zero at a single propagation step in all of the computational window except for a small aperture. This can be seen in Fig 4.6. Here the optical field is forced to zero in the shaded zone. The edges of the aperture are positioned so that they are far away from the guiding mode. In this situation the aperture has a minimum influence in the optical field. The aperture lets the "mode" pass and blocks some of the radiation losses. Next we allowed the optical field to propagate, and measured the intensity that entered the shaded zone of Fig 4.6. By doing this we observed the increase in the radiation loss as a function of the propagation distance. The results can be seen in Fig 4.7. In Fig 4.7(a) the increase in the losses is nearly linear with the propagation distance, while in Fig 4.7(b) we can see a step like behaviour. Every step corresponds to the energy generated by one period. This cannot be seen in Fig 4.7(a) because the segmentation loss from one period overlaps with the radiation generated at previous periods. The losses are obtained by comparing the total energy in the mode with the radiation energy given by Fig 4.7:

$$loss = \left(10\log\frac{Total\_energy - Radiation\_loss}{Total\_energy}\right)\frac{1}{Length}\left[dB/cm\right] \qquad \text{Eq 4.15}$$

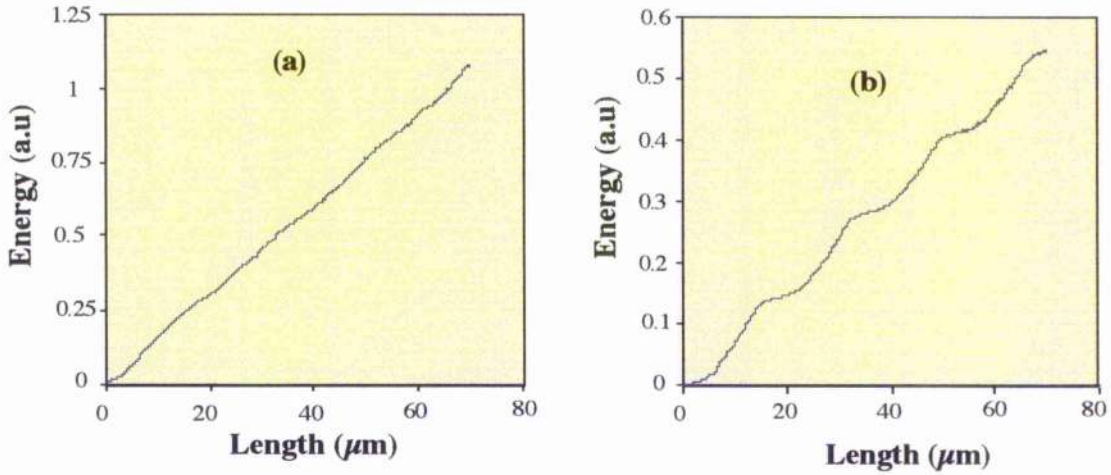

Fig 4.7. Radiation entering the shaded region of Fig 4.5 as a function of the propagation distance for PSW of period 17.5 μm and duty-cycle 0.5 (a) and 0.8 (b).

4.4.2.2. Segmentation loss as a function of the period and duty-cycle.

Figure 4.8 shows the segmentation loss as a function of the duty-cycle and as a function of the period. These absolute values are larger than those reported previously, both experimentally [8, 9] and theoretically [7, 9]. This is due to the relatively large refractive index modulation used to reduce the computational time. In addition, the index profile is a step function, whereas for $LiNbO_3$ waveguides a diffusion profile should be used. The general shape of the curves coincides with those of refs. [7,8,9].

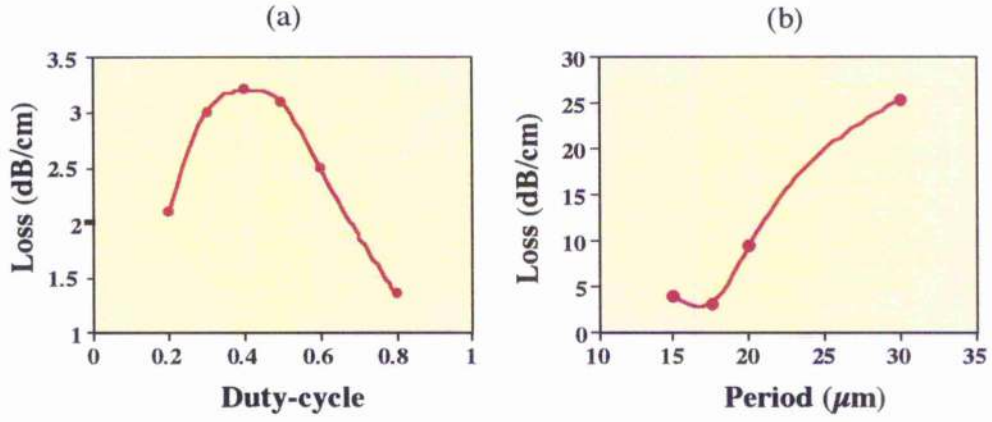

Fig 4.8. Segmentation loss as a function of the duty-cycle (a) and period (b). The point represents the results obtained with the BPM and the lines are their interpolation.

From Fig 4.8(a) it can be seen that the radiation losses have a maximum when the duty-cycle is ~0.5. The decrease in the radiation losses as the duty-cycle increases is due to the reduction in the gap between the doped segments; this minimises the space in which the beam is allowed to diffract. The decrease in the radiation losses as the duty-cycle is reduced is due to the increase in the mode size, and therefore a reduction in the diffraction angle. Therefore, large duty-cycle with small gap and small duty-cycle with small diffracting angles are competing mechanisms to reduce the radiation loss.

We have also considered the case of radiation loss as a function of the period (Fig 4.8(b)). The average mode size is the same for all periods, therefore, we expect the radiation losses to increase with the period (i.e. as the gap between doped regions increases). It should be noted that the radiation losses for waveguides of the same length increase as the period decreases. This is because the segmentation loss is proportional to the number of periods.

4.4.3. Variations of the "mode" size as a function of the duty cycle and period

In Chapter 3 we have shown that a PSW can be represented by an equivalent continuous waveguide in which the increase in the refractive index is given by Eq 4.13. Now we are going to use this to prove that the 3D EFD-BPM adequately describes the propagation of light though a PSW. To that purpose we compared the mode width and depth of PSWs and its equivalent continuous waveguide for different duty cycles using the 3D EFD-BPM. The results can be seen in Fig 4.9. The lines represent calculations performed for the PSWs and the points the results obtained using the equivalent continuous waveguide. The mode width and depth of the PSWs was calculated from the curves of Fig 4.10, where the intensity profile in the vertical and horizontal direction is shown at the beginning of each period for different duty- cycles and periods.

The variation of the mode width and height as a function of the period can be seen in Fig 4.11. Here we can see that the mode size is very similar for all periods, but there may be some differences in the intensity distribution. This is in agreement with the equivalent waveguide model proposed.

The consensus between both sets of results for the PSW and its equivalent continuous waveguide in Fig 4.9, and the independence of the mode size on the

period (Fig 4.11) indicate that a step index PSW can be represented by an equivalent continuous waveguide. In Chapter 3 we have experimentally demonstrated that a PSW can be represented by an equivalent continuous waveguide, therefore the results of Fig 4.9 and 4.11 suggest that the 3D EFD-BPM accurately simulate PSWs.

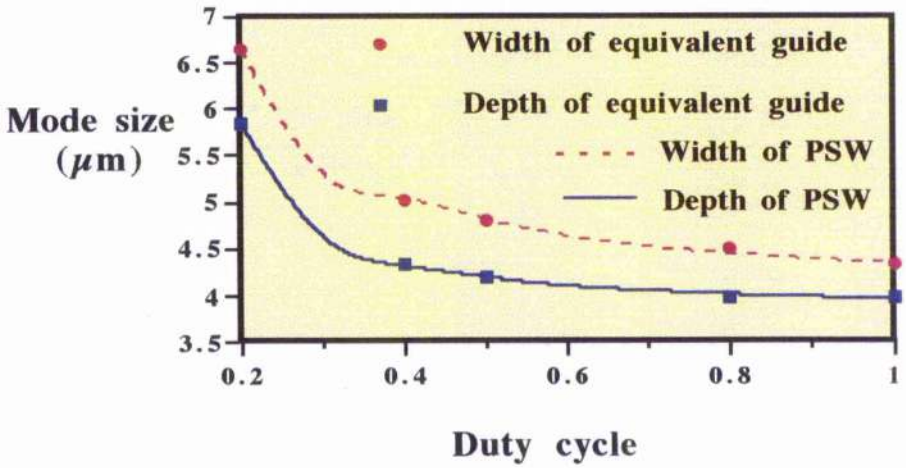

Fig 4.9. Variation of the mode width and depth with the duty cycle for PSWs and the equivalent continuous waveguides. The mode width and depth were obtained from the curves of Fig 4.10. The mode size were measured at 0.3 of the maximum. Operating wavelength 1.55 μm.

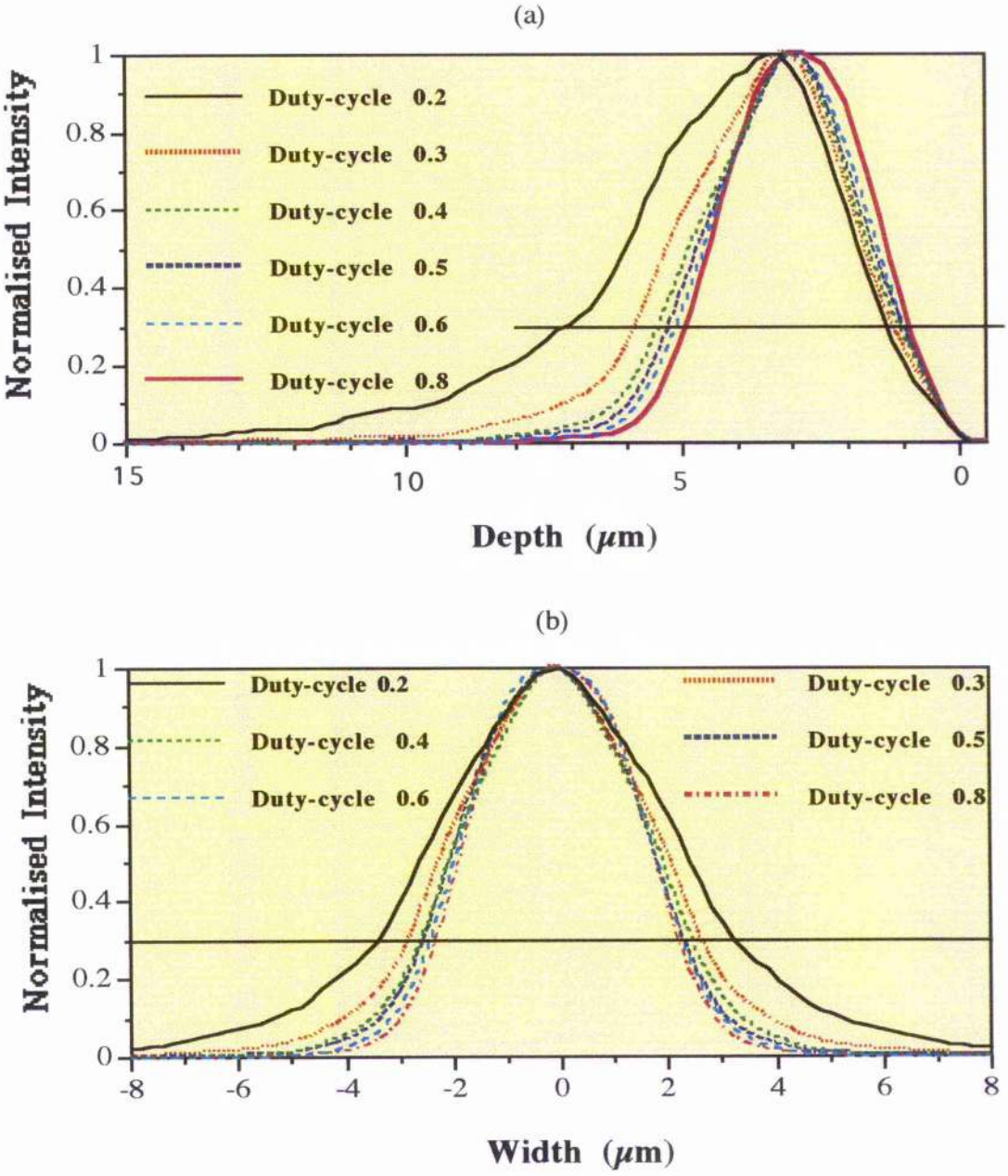

Fig 4.10. Vertical (a) and horizontal (b) intensity profile for PSWs of period 17.5 μm and different duty cycles ranging from 0.2 to 0.8. The intensity distribution in one direction was obtained by adding the intensity in the transversal direction and then it was normalised so that the maximum has a value of one. In all cases the intensity distribution was obtained at the beginning of a doped segment.

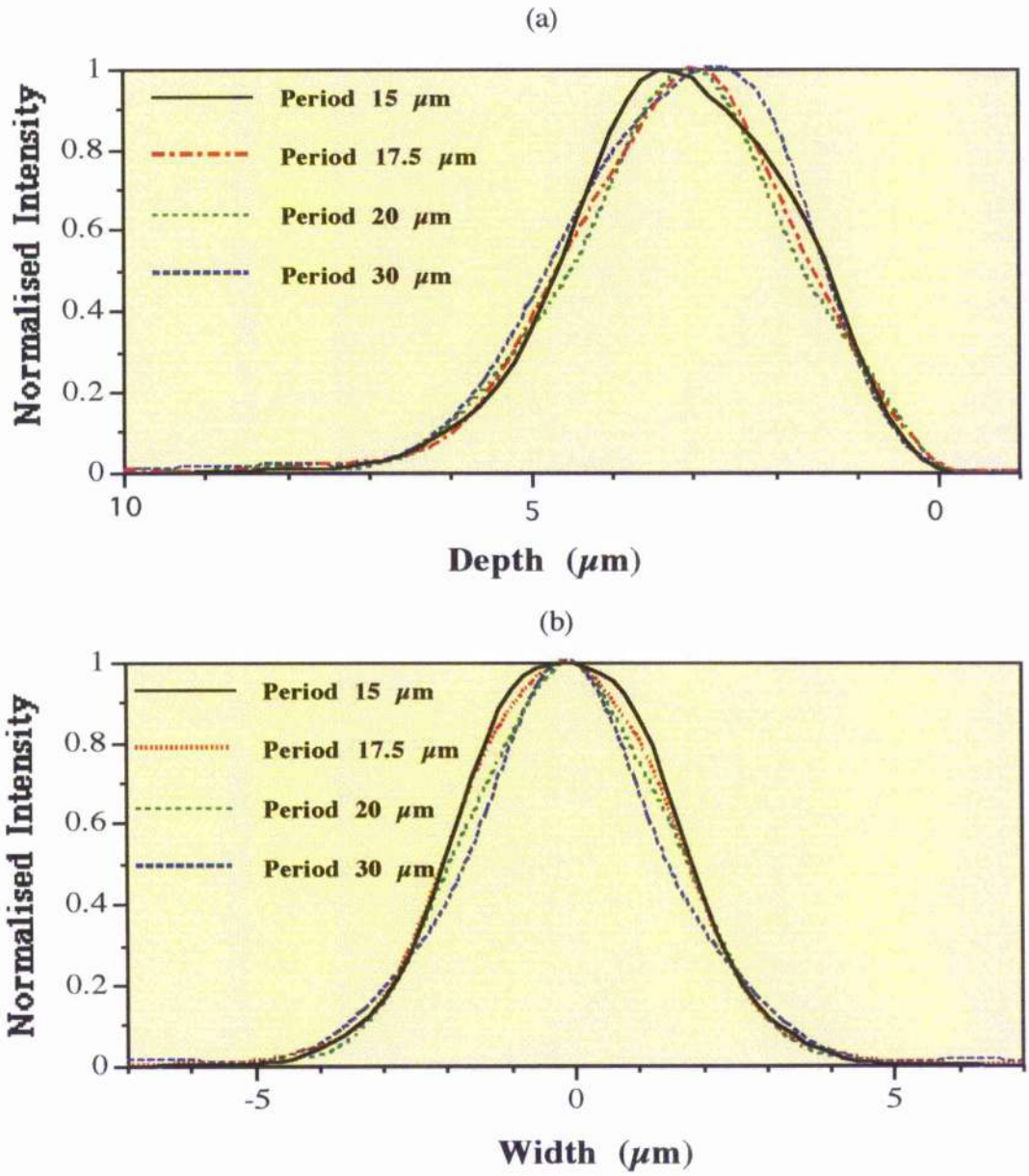

Fig 4.11. Vertical (a) and horizontal (b) intensity profile of PSWs. The intensity distribution in one direction was obtained by adding the intensity in the transversal direction and then it was normalised so that the maximum has a value of one. In all cases the intensity distribution was obtained at the beginning of a doped segment. The duty-cycle of the PSW is 0.5.

4.5. Conclusions.

We have shown that a PSW can be represented by an equivalent continuous waveguide and that the 3D EFD-BPM adequately describes the propagation of light through PSWs. The equivalent waveguide model provides a good design tool for calculating the modal properties of PSWs. However, it does not provide any information about the radiation losses of the waveguides, or the behaviour of the optical field along the direction of propagation. We have seen that a 3D representation of the PSWs is necessary to evaluate the radiation losses, both in the direction of the substrate and in the lateral direction.

The Three-Dimensional Explicit Finite Difference Method has been used to study the propagation characteristics of the optical field in Periodic Segmented Waveguides. We found that the period and duty-cycle of the PSWs together with the index distribution, set the conditions that will allow a certain field distribution to be sustained by the waveguide, i.e. set the modes of the PSW and with the mode, the radiation losses. We have shown that PSWs have "modes" where the intensity profile is repeated periodically along the direction of propagation, except for a reduction of the amplitude due to radiation loss. Thus, modes in a PSW are three-dimensional functions, formed by the optical field in one period. The numerical simulations illustrate how the segmentation loss escapes from the waveguide. We were able to measure the magnitude of the losses as a function of the period and duty-cycle. We found that for long periods, in our structure, the radiation loss becomes excessively large.

4.6. References.

[1] Y. Chung and N. Dagli "Analysis of Z-invariant a Z-variant semiconductor rib waveguides by explicit finite difference beam propagation method with nonuniform mesh configuration", IEEE J. Quantum Electron, **QE-27**, pp. 2296-2305, (1991).

[2] A. W. Snyder and J D Love, "Optical waveguide theory", J W Arrowsmith Ltd. Bristol, 1983.

[3] K. W. Morton and D F Mayers, "Numerical solutions of partial differenctial equations", Cambridge unversity press, 1994.

[4] G R Hadley, "Transparent boundary conditions for the beam propagation method", IEEE Journal of quantum electronics, **28**, pp. 363-370, (1992).

[5] G R Hadley, "Transparent boundary conditions for beam propagation", Optics letters, **16**, pp. 624-626, (1991).

[6] S. Fouchet, A. Carenco, C. Daguet, R. Guglielmi, and L. Riviere, "Wavelength Dispersion of Ti Induced Refractive Index Change in Ti:LiNbO3 as a function of Diffusion Parameters", Journal of Lightwave technology, **LT-5**, pp. 700 - 708 (1987).

[7] Z. Weissman and A. Hardy: "Modes of Periodically Segmented Waveguides", J. Lightwave Tech., 1993, **11**, pp. 1831-1838.

[8] M. H. Chou, M. A. Arbone, and M. M. Fejer, "Periodically-segmented tapered waveguides for mode-size transformation and fundamental mode excitation", 1996 technical digest series , Integrated photonics research, vol 6, pp. 506 - 509, Boston, April 1996.

[9] D. Nir, Z. Weissman, S. Ruschin, and A. Hardy, "Periodically segmented waveguides in Ti:LiNbO3" Opt. Lett. **19**, pp. 1732 - 1734, (1994).

5

SHG in PSWs

In this Chapter we will show how, using Ti:$LiNbO_3$ PSWs, we were able to generate the second harmonic of a 1.55 μm fundamental wave. There are a few possible mechanisms by which second harmonics (SH) can be generated in a PSW, but only two result in significant conversion: a) the periodic reversal of the sign of the nonlinear coefficient and b) periodic modulation of the propagation constant. We will show the theoretical detuning curves for both cases, and we will derive a general up-conversion / down-conversion condition to include the case of SHG produced by a modulation of the propagation constant.

In Chapter 3 and 4 we have shown that a PSW behaves like a continuous waveguide, where the increase in the refractive index is given by the average titanium concentration. We have illustrated that the mode size is modulated as the beam propagates over one period. In this Chapter, we will investigate the behaviour of the propagation constant along a PSW. By chirping the period of the PSWs we were able to control the tuning curves of the SHG process, and we were able to model them with numerical simulations.

5.1. Introduction.

Coupling between two modes takes place if a coupling coefficient exists, and if the propagation constant of the two modes is the same. In grating assisted coupling any difference between the propagation constants is compensated by the period. Grating assisted coupling using PSWs is not new, for example it has been demonstrate in SHG [1], but what is not clear at present is the behaviour of the propagation constant as the PSW mode propagates. Some authors propose a change in the propagation constant as the wave progresses through areas with different indices [2, 3, 4]. However, no conclusive evidence of this has been reported in the literature.

Traditionally SHG has been obtained by modulating the nonlinear properties, via a process called domain reversal. As we have shown in Chapter 2, there are situations where domain reversal can be obtained during the fabrication of PSWs. If a Ti:$LiNbO_3$ PSW is fabricated on the positive face, the waveguide has both a periodic modulation of the refractive index and a modulation of the nonlinear coefficient. If a Ti:$LiNbO_3$ PSW is fabricated on the negative face, the waveguide only experiences a modulation of the refractive index.

In this Chapter, we investigate the phase matching properties of PSWs by considering the details of the SHG process. Quasi-phase matching (QPM) SHG takes place at a wavelength where the difference between the propagation constants of the fundamental and SH is compensated by the period of the PSW. We will show that a periodic modulation of the nonlinear coefficient only, and a modulation of both the propagation constant and the nonlinear coefficient, yields different phase-matching curves. However, the experimental detuning curves show no indication of a modulation in the propagation constant.

First, we fabricated and tested PSWs with different periods and attempted to predict the phase matching wavelength from the fabrication conditions. For this we needed to estimate the propagation constant of the fundamental and SH from the index distribution using a mode solver. The problem with PSWs is that the index distribution is not uniform along the direction of propagation, and therefore we had to average it.

We also fabricated chirped PSWs and compared their detuning curves with those obtained theoretically. Briefly, we will discuss the application of chirp waveguides in all-optical switching.

All the software used to simulate SHG has been developed to take into consideration the dispersion of the material and some of the limitations imposed by fabrication.

5.2. Theory for second harmonic generation (SHG).

In this section we will discuss the conditions required for efficient SHG. SHG is a second order nonlinear process and arises as a consequence of a nonlinear interaction between light and matter. In SHG two photons from the fundamental generate one photon at double the frequency, the second harmonic (SH). However, this process is only efficient under certain circumstances, which depend on the propagation of the fundamental and SH waves in the nonlinear material. Therefore, to describe SHG it

is necessary to generate a wave equation for each of the frequencies involved and the coupling between them. Because this is a very difficult system to solve, some approximation has to be used to simplify the problem.

5.2.1. Dielectrics

As light propagates in a medium the photons will interact with the atoms. Therefore the light modifies the medium, which in turn influences the propagation of the light. The permittivity and the permeability are the macroscopic quantities which account for the microscopic behaviour of the light in the material. They are introduced in Maxwell's equations by substituting the electric field (E) with the electrical displacement (D) and the magnetic flux density (B) with the magnetic field (H).

The effect of the material on the electromagnetic (EM) field can be studied by considering that the incident EM field polarises the atoms in the material, which creates a polarisation charge that modifies the incident field. If the energy of the incident beam is small, the response of the material is proportional to the electric field and therefore the polarisation charge oscillates with the same frequency of the incident field. However, if the optical field is very intense, the response of the material is nonlinear and the polarisation charge oscillates at a different frequency from that of the incident field.

In general, for two optical fields at frequencies ω_1 and ω_2, the second order nonlinear interaction between the material and the two EM waves produces dipole momentums which oscillate with the following frequencies:

$$\begin{aligned} \omega_1 + \omega_2 &= \omega_3 \\ \omega_1 - \omega_2 &= \omega_4 \\ \omega_2 - \omega_1 &= \omega_5 \end{aligned} \quad , \qquad \text{Eq 5.1}$$

and each dipole generates light at its oscillating frequency.

Once ω_3 has been generated, the interaction between the new wave and the existing waves generates polarisation terms at the following frequencies:

$$\begin{aligned} \omega_3 - \omega_1 &= \omega_2 \\ \omega_3 - \omega_2 &= \omega_1 \end{aligned} \qquad \text{Eq 5.2}$$

5.2.2. Up-conversion and down-conversion

In a second order nonlinear process, where we have two optical fields at frequency ω_1 and ω_2, there are three competing processes:

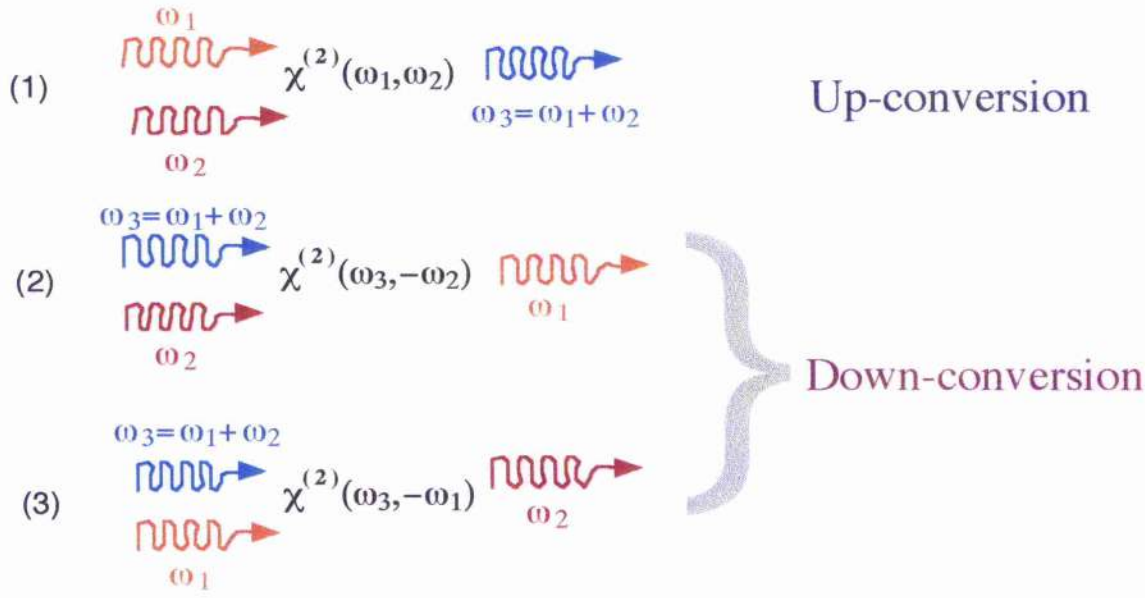

Fig 5.1

In process 1, photons at frequencies ω_1 and ω_2 generate a photon at a new frequency ω_3 ($=\omega_1+\omega_2$). In processes 2 and 3 the generated photon at ω_3 in combination with one of the two original photons (ω_1 or ω_2) generates the other photon (ω_2 or ω_1). Therefore, the nonlinear process will generate photons at ω_3 (up-conversion), but will consume them as well (down conversion). Up-conversion, or down conversion will dominate depending on the relative phases of the three waves. Therefore, to analyse the system we have to obtain three wave equations which are coupled through the nonlinear coefficient.

Starting from the Maxwell equations and using the following approximations:

1 $\underline{E}(x,y,z,t) = \underline{E}^{\omega}(x,y,z)\exp(-i\omega t)$

2 $\underline{E}^{\omega} = \hat{\underline{E}}^{\omega}(z)\exp(ikz)$

3 $\hat{\underline{E}}^{\omega}$, will only vary on propagation, i.e. is only a function of z:

4 The envelope $\hat{\underline{E}}^{\omega}(z)$ varies much less rapidly than $\exp(ikz)$, the slowly varying envelope approximation.

5 Overall permutation symmetry $\Rightarrow$

$$\chi^{(2)}(\omega_3,-\omega_2) = \chi^{(2)}(\omega_3,-\omega_1) = \chi^{(2)}(\omega_1,\omega_2) = \chi^{(2)}$$

6 A non conducting medium.

we obtain the following system of equations:

$$\begin{cases} \dfrac{\partial \hat{\underline{E}}^{\omega_3}}{\partial z} = \dfrac{i\omega_3}{cn_3} d_{eff} \hat{E}^{\omega_1} \hat{E}^{\omega_2} \exp(i\Delta kz) \\ \dfrac{\partial \hat{\underline{E}}^{\omega_1}}{\partial z} = \dfrac{i\omega_1}{cn_1} d_{eff} \hat{E}^{\omega_3} \left(\hat{E}^{\omega_2}\right)^* \exp(-i\Delta kz) \\ \dfrac{\partial \hat{\underline{E}}^{\omega_2}}{\partial z} = \dfrac{i\omega_2}{cn_2} d_{eff} \hat{E}^{\omega_3} \left(\hat{E}^{\omega_1}\right)^* \exp(-i\Delta kz) \end{cases} \qquad \text{Eq 5.3}$$

Where:

- n_1, n_2 and n_3 are the effective indices of the propagating modes..
- $\Delta k = k_1 + k_2 - k_3$
- $d = \dfrac{\chi^{(2)}}{2}$
- $d :: \hat{\underline{E}}^{\omega_1} \hat{\underline{E}}^{\omega_2} = d_{eff} \hat{E}^{\omega_1} \hat{E}^{\omega_2}$

  where $d_{eff} = d : \hat{\underline{e}}_1 \hat{\underline{e}}_2$, $\hat{\underline{e}}_1$ and $\hat{\underline{e}}_2$ are unitary vectors in the direction of $\hat{\underline{E}}^{\omega_1}$ and $\hat{\underline{E}}^{\omega_2}$.

A detailed derivation of these equations can is given in Appendix 3 .

5.2.3. Second harmonic generation.

Second harmonic generation occurs when a wave interacts with itself to generate the sum frequency. In this situation we can use Eq. 5.3 assuming $\omega_1=\omega_2=\omega$ and $\omega_3=2\omega$. Then, the coupled differential equations that describe the process can be expressed as:

$$\begin{cases} \dfrac{\partial \hat{\underline{E}}^{\omega}}{\partial z} = \dfrac{i\omega}{2cn_{\omega}} d_{eff}(2\omega, -\omega) \hat{E}^{2\omega} \left(\hat{E}^{\omega}\right)^* \exp(-i\Delta kz) \\ \dfrac{\partial \hat{\underline{E}}^{2\omega}}{\partial z} = \dfrac{i\omega}{cn_{2\omega}} d_{eff}(\omega, \omega) \left(\hat{E}^{\omega}\right)^2 \exp(i\Delta kz) \end{cases} \qquad \text{Eq 5.4}$$

Where,

$$\Delta k = 2k_{\omega} - k_{2\omega} = \frac{4\pi}{\lambda_{\omega}} \left(n_{\omega} - n_{2\omega}\right) \qquad \text{Eq 5.5}$$

If we apply the Manley-Rowe relations we obtain

$$d_{eff}(2\omega,-\omega)=2d_{eff}(\omega,\omega). \qquad \text{Eq 5.6}$$

This means that we have two photons of the fundamental to one of the second harmonic.

5.2.4. Overlap area.

Equations 5.3 and 5.4 apply to plane waves, therefore, there is no confinement. To incorporate the properties of the waveguides in our equation we define an overlap area.

If we want to express the amplitude of the electric field ($|E^{\omega}|$)in terms of the power (P^{ω}), we need to know the area in which the beam is propagating:

$$\left.\begin{aligned} I^{\omega}&=\frac{\varepsilon_o cn(\omega)}{2}\left|E^{\omega}\right|^2 \\ I^{\omega}&=\frac{P^{\omega}}{Area}\end{aligned}\right\}\Rightarrow\left|E^{\omega}\right|^2=\frac{P^{\omega}}{Area}\frac{2}{\varepsilon_o cn(\omega)} \qquad \text{Eq 5.7}$$

where I^{ω} is the intensity.

In SHG, the efficiency of the process is given by the overlap integral between the fundamental and SH modes ($I_{overlap}$). Therefore, to include the area in which the interaction takes place we define the overlap area, $A_{overlap}$, as:

$$\begin{aligned} A_{overlap}&=\frac{1}{I_{overlap}^2} \\ I_{overlap}&=\int_{-\infty}^{\infty}\int_{-\infty}^{\infty}\left(\hat{E}^{\omega}(x,y)\right)^2\hat{E}^{2\omega}(x,y)dxdy\end{aligned} \qquad \text{Eq 5.8}$$

where x and y are the space coordinates in a cross section of the waveguide. The amplitudes are normalised according to

$$\int_{-\infty}^{\infty}\int_{-\infty}^{\infty}\left|\hat{E}(x,y)\right|^2dxdy=1 \qquad \text{Eq 5.9}$$

5.2.5. Solving the coupled amplitude equations governing SHG.

The coupled differential equations of Eq 5.4 have been solved using the fourth-order Runge-Kutta method. If the fundamental beam is polarised so that the electric field is parallel to the z axis of the $LiNbO_3$ crystal, the nonlinear polarisation and therefore the SH have only a component in the z direction. This can bee seen in Eq 2.3 of Chapter 2. For this situation the d-coefficient is d_{33}= 30 pm/v. $LiNbO_3$ is a birefringent crystal and the z direction is that of the extraordinary ray. The implementation of the Runge-Kutta method is outlined in more detail in Appendix 5.

Equation 5.4 will be solved for three different structures:

- A waveguide with a periodic change in the sign of the nonlinear coefficient. This is implemented by changing the sign of the nonlinear coefficient in Eq 5.4 .

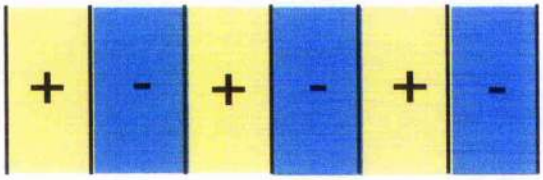

Fig 5.2

- A waveguide with a periodic modulation of the propagation constant for the fundamental and SH. This is implemented by changing the value of the effective indices in Eq. 5.4.

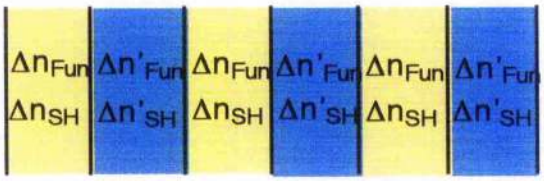

Fig 5.3

- A waveguide with both a modulation in the sign of d_{eff} and the propagation constant. This is implemented by changing the value of the effective indices and sign of the nonlinear coefficient in Eq. 5.4.

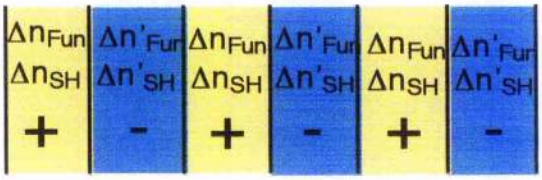

Fig 5.4

To implement the periodic modulation in the refractive index and the nonlinear coefficient, only these two parameters have been changed in the coupled differential equation. Other effects that may take place at the boundary between two different materials were not considered.

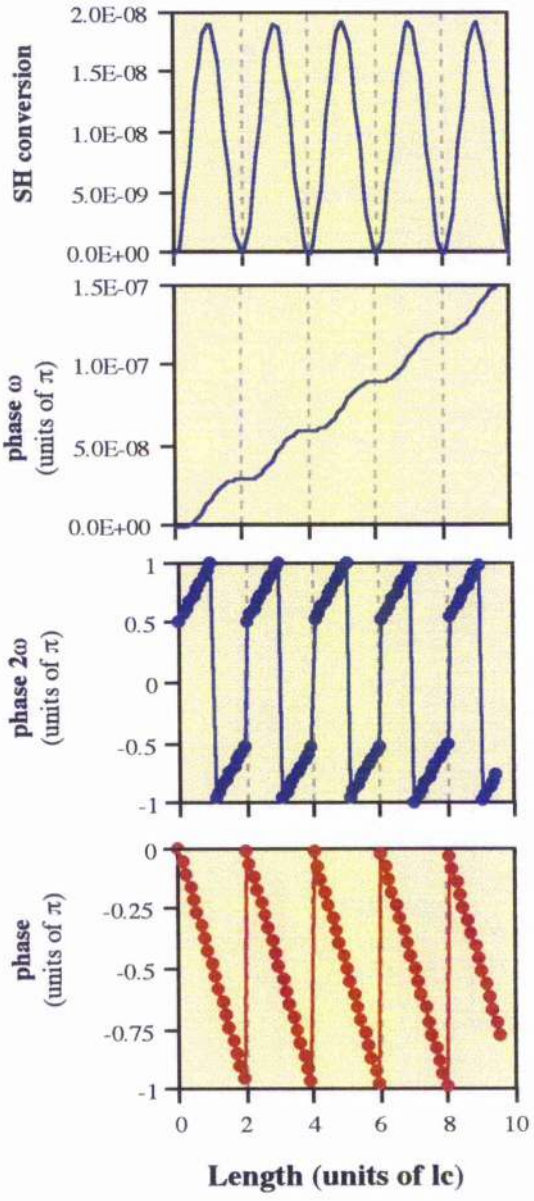

Fig 5.5. The **SH conversion** efficiency is the ratio between the SH and the initial fundamental power. The nonlinear phase of the fundamental (**phase** ω) and SH (**phase 2ω**), is the phase terms of $\hat{E}^{\omega}$ and $\hat{E}^{2\omega}$ in Eq 5.4. The phase condition for up-conversion and down-conversion of Eq 5.12 and 5.13 is labelled as **phase**. These values were obtained by numerically solving Eq 5.4 using the Runge- Kutta method for a $LiNbO_3$ waveguide 0.1 mm long, effective area of 2.1×10^{-7} m^2, and 100 W input power. The d_{33} nonlinear coefficient was used. Operational wavelength 1.55 μm.

5.2.6. Quasi-Phase Matching

In SHG, a fundamental wave with frequency ω and wavelength λ interacts with the second-order nonlinear susceptibility of the material to produce a polarisation wave at the second harmonic frequency 2ω. Since the polarisation wave is forced by the fundamental wave, it travels with the same velocity, determined by n_{ω}. The polarisation wave radiates a free second-harmonic wave which travels at a velocity determined by $n_{2\omega}$. In general $n_{2\omega} > n_{\omega}$ because of normal dispersion in the material, so that the fundamental and second harmonic wave travel with different phase velocities. To a first approximation we can say that the direction of power flow from one wave to another is determined by the relative phase between the waves. The continuous phase slip between these waves leads to an alteration in the direction of the flow of power. The alteration in the direction of the power flow leads to a repetitive growth and decay of the second harmonic intensity along the length of the interaction (see Fig 5.5). The distance over which the relative phase of the two waves changes by π is the coherence length, l_c

$$l_c = \frac{\lambda}{4(n_{2\omega} - n_{\omega})} = \frac{\pi}{\Delta k} \qquad \text{Eq 5.10}$$

which is also the half period of the growth and decay cycle of the second harmonic.

If the refractive indices can be matched by some means (i.e. $n_{2\omega} = n_{\omega}$), the second harmonic field grows linearly with distance in the medium, and thus the intensity grows quadratically. This condition is known as phase matching (see Fig 5.6).

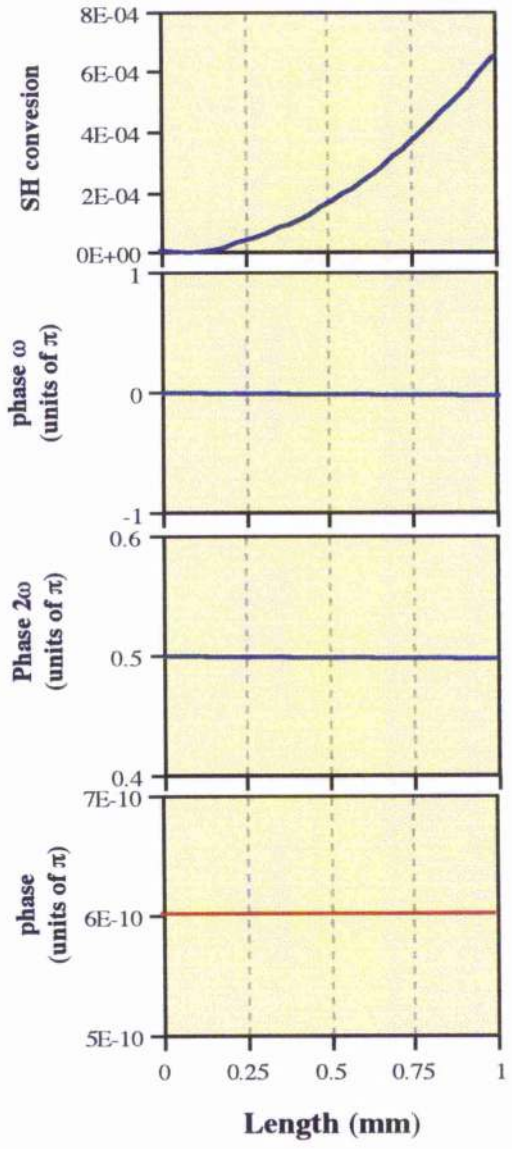

Fig 5.6. Representation of the SH conversion efficiency, the nonlinear phase shift of the fundamental and SH, and the up-conversion and down-conversion condition of Eq 5.12 and 5.13 for a phase marched waveguide. All the parameters and definitions are those of Fig 5.5 except for the effective index for the fundamental and SH. Here they have artificially been set to be equal; n_{ω}=$n_{2\omega}$=2.

Here, we propose an alternative, more general, condition for up-conversion and down conversion in SHG, depending on the nonlinear phases of the fundamental and SH, and the phase mismatch (Δk). From the coupled differential equations (Eq 5.4), the variation of the second harmonic electric field with propagation is given by:

$$\frac{\partial \hat{E}^{2\omega}}{\partial z} = \frac{i\omega}{cn_{2\omega}} d_{eff}(\omega,\omega)\left(\hat{E}^{\omega}\right)^2 \exp(i\Delta kz)$$

Eq 5.11

and using Eulers formula for the first order, it can be shown that the condition for up-conversion can be expressed as:

$$\left|Phase^{2\omega}_{nonlinear} - \left(\Delta kz + \frac{\pi}{2} + 2Phase^{\omega}_{nonlinear}\right)\right| < \frac{\pi}{2}$$

$$Phase^{2\omega}_{nonlinear} = Phase\left(\hat{E}^{2\omega}\right)$$

$$Phase^{\omega}_{nonlinear} = Phase\left(\hat{E}^{\omega}\right) \qquad Eq\ 5.12$$

$$\Delta kz + \frac{\pi}{2} \in [0, 2\pi]$$

Where $\hat{E}^{2\omega}$ and $\hat{E}^{\omega}$ are obtained from Eq 5.4. The derivation of this expression is outlined in more detail in Appendix 6.

Using the same arguments as for Eq 5.12, the SH harmonic converts into fundamental (i.e. down- conversion)

when:

$$\left|Phase^{2\omega}_{nonlinear} - \left(\Delta kz + \frac{\pi}{2} + 2Phase^{\omega}_{nonlinear}\right)\right| > \frac{\pi}{2} \qquad \text{Eq 5.13}$$

and neither down conversion or up conversion occurs when:

$$\left|Phase^{2\omega}_{nonlinear} - \left(\Delta kz + \frac{\pi}{2} + 2Phase^{\omega}_{nonlinear}\right)\right| = \frac{\pi}{2} \qquad \text{Eq 5.14}$$

In Fig 5.5 we can see how the condition for up-conversion and down-conversion is related to an increase and decrease of the SH conversion. The condition of Eq 5.14 corresponds to the transitions from up-conversion to down-conversion at $z \approx nl_c$ where n is 1,2,3,.....

In a phase matched situation : (see Fig 5.6)

$$\left|Phase^{2\omega}_{nonlinear} - \left(\Delta kz + \frac{\pi}{2} + 2Phase^{\omega}_{nonlinear}\right)\right| = 0 \qquad \text{Eq 5.15}$$

which corresponds to the most efficient case.

If phase matching does not exist (i.e. $n_{\omega} \neq n_{2\omega}$), a continuous growth of the SH can be obtained by controlling the relative phase of the SH and fundamental. This can be done by periodically modulating the nonlinear and/or linear properties of the material. In this situation, the period compensates for the phase difference between the SH and fundamental, this is called quasi-phase matching (QPM).

5.2.6.1. Domain reversal quasi-phase matching.

If, after the fundamental and SH have propagated a distance l_c we reverse the sign of the nonlinear coefficient, the direction of the flow of power is reversed and the growth of the SH is regained, see Fig 5.7. The change in the sign of the nonlinear coefficient is equivalent to introducing a phase π in Eq 5.12. This means that after $z=l_C$, by changing the sign of the nonlinear coefficient, we maintain Eq 5.12 in the condition for up-conversion, see Fig 5.7.

5.2.6.2. Modulation of the propagation constant quasi-phase matching.

The modulation of the propagation constant implies a modulation of n_ω, $n_{2\omega}$ and Δk in Eq 5.4. Modulation of the phase mismatch (Δk) is obtained only if the modulation of the propagation constant of the fundamental is different from the modulation of the propagation constant of the SH. In a typical Ti:$LiNbO_3$ waveguide the modulation of the propagation constant on its own (without the modulation in the phase mismatch) results in a very inefficient quasi-phase matching process.

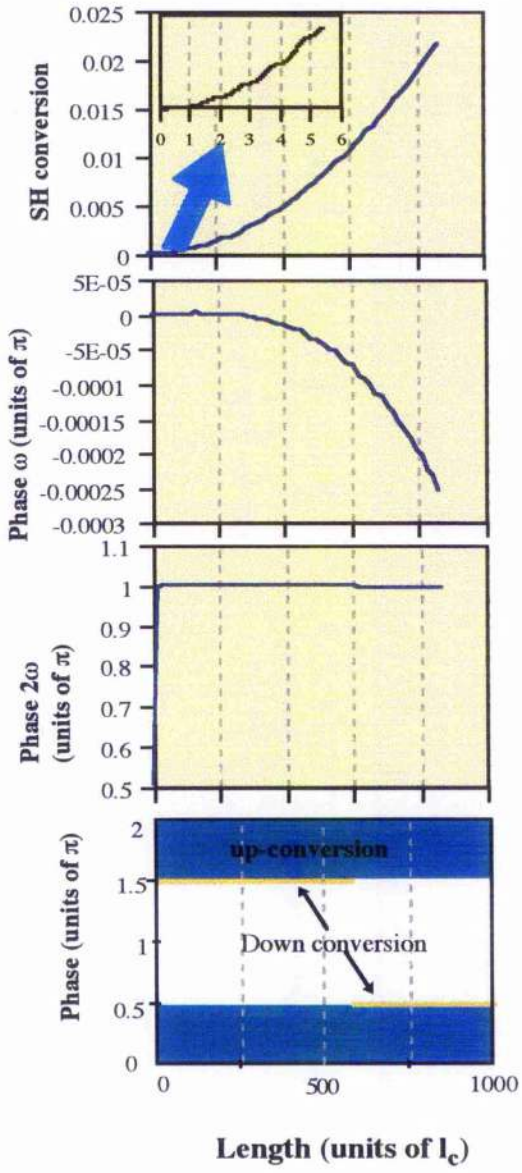

Fig 5.7. Representation of the SH conversion efficiency, the nonlinear phase shift of the fundamental and SH, and the up-conversion and down-conversion condition of Eq 5.12 and 5.13 for a waveguide with domain reversal. All the parameters and definitions are those of Fig 5.5. Period 18.5 μm and a duty-cycle 0.5. The operational wavelength is 1.5368 μm.

Here, unlike domain reversal QPM, we do not try to suppress the down conversion process. At the start of the propagation, the periodic modulation of the phase mismatch does not have a large effect on the net conversion from the fundamental to the SH, but as the optical field propagates in the PSW, the modulation of the phase mismatch has an accumulative effect in the up-conversion / down- conversion equilibrium. This can be seen in Fig 5.8, where the condition for up- conversion (as given by Eq 5.12) dominates the condition for down-conversion (given by Eq 5.13).

5.2.6.3. Modulation of the propagation constant and sign of the nonlinear coefficient quasi-phase matching.

The combined effect of domain reversal and periodic modulation of the phase mismatch is not easy to predict. At the beginning of propagation the influence of the PSW on the conversion efficiency is small (see Fig 5.9), and therefore the phase matching process is similar to pure domain reversal. But after relatively long

propagating distances, the accumulative effect of the PSW starts to affect the SHG.

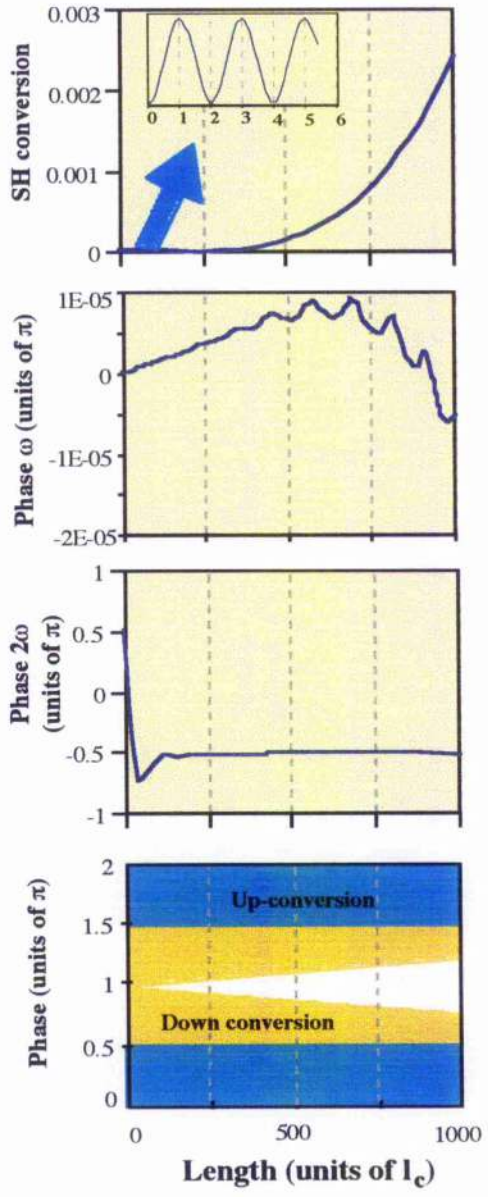

Fig 5.8. Representation of the SH conversion efficiency, the nonlinear phase shift of the fundamental and SH, and the up-conversion and down-conversion condition of Eq 5.12 and 5.13 for a PSW with a difference in the modulations of the propagation constant of the fundamental and SH of 10^{-5}. All the parameters and definitions are those of Fig 5.5. The period of the modulation is 18.5 μm and the duty-cycle 0.5. The operational wavelength is 1.5368 μm.

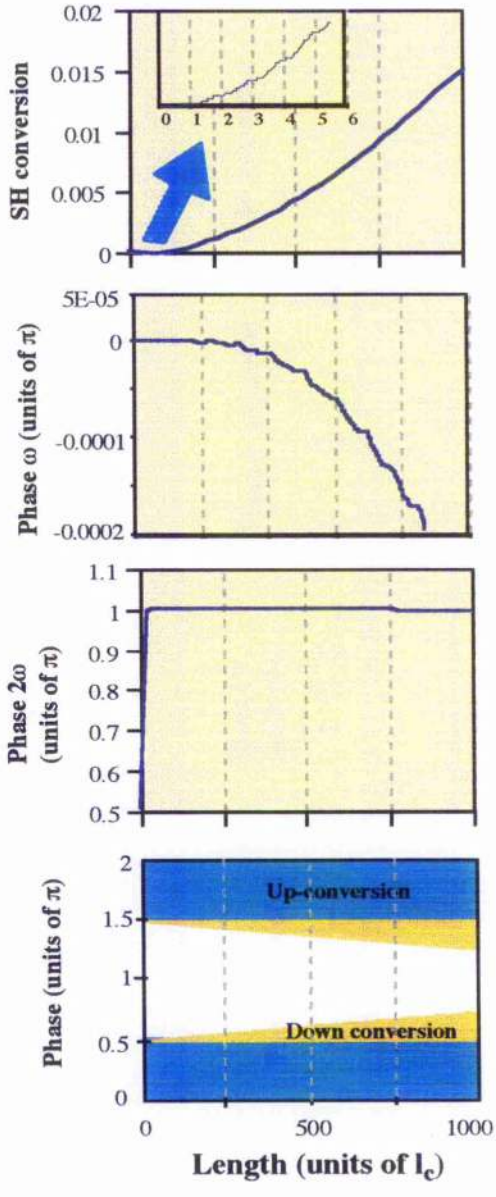

Fig 5.9. Representation of the SH conversion efficiency, the nonlinear phase shift of the fundamental and SH, and the up-conversion and down-conversion condition of Eq 5.12 and 5.13 for a PSW with a modulation in the propagation constant of the fundamental and SH, and domain reversal. All the parameters and definitions are those of Fig 5.5. The period of the modulation is 18.5 μm and the duty-cycle 0.5. The operational wavelength is 1.5368 μm.

5.2.7. Quasi-phase matching period.

In the case of domain reversal QPM the sign of the nonlinear coefficient has to be changed every coherent length, l_c. Therefore the period of the modulation, Λ, is twice the coherent length. Using Eq 5.10 we obtain:

$$\Lambda = 2l_c = \frac{2\pi}{\Delta k} = \frac{\lambda_\omega}{2(n_{2\omega} - n_\omega)} \qquad \text{Eq 5.16}$$

We can also view this as a grating assisted process, where the spatial harmonics of the grating are used to compensate for the phase mismatch. In the case of domain reversal QPM we modulate the nonlinear coefficient. In the case of PSW QPM we modulate the phase mismatch. In both situations we can express the periodic properties in the form of a Fourier series:

$$a(z) = \sum_{q=-\infty}^{\infty} a_q \exp(-iq\mathrm{K}z) \qquad \text{Eq 5.17}$$

Where a is either the nonlinear coefficient of the phase mismatch, and K is the spatial frequency of the grating:

$$\mathrm{K} = \frac{2\pi}{\Lambda} \qquad \text{Eq 5.18}$$

QPM takes place when

$$\Delta k + q\mathrm{K} = 0 \qquad q = 1, 2, 3, \cdots \qquad \text{Eq 5.19}$$

Using Eq 5.18 and Eq 5.19 we obtain that the phase matching period is :

$$\Lambda = \frac{2\pi}{\Delta k} = \frac{\lambda_\omega}{2(n_{2\omega} - n_\omega)} \qquad \text{Eq 5.20}$$

Which is the same as in Eq 5.16.

5.2.8. Detuning curves.

The conversion from the fundamental wavelength to the SH wavelength depends upon the phase mismatch, Δk. At phase matching (i.e. $\Delta k = 0$) we get maximum conversion from the fundamental to the SH. As we move away from the phase matched condition the conversion efficiency is reduced. Similarly for QPM, but now the maximum efficiency occurs at $\Delta k + 2\pi/\Lambda = 0$. Therefore a detuning curve represents the SH conversion efficiency as we detune from phase matching. Due to the dependency of Δk on the wavelength (see Fig 5.10) the representation of the SH conversion against the wavelength results in a detuning curve, this can be seen in Fig 5.11.

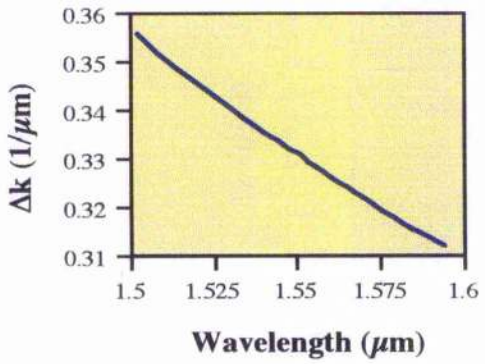

Fig 5.10. Dependency of the phase mismatch on the wavelength. For the case in which the e-ray of the fundamental interacts with the e-ray of the SH through the d_{33} coefficient. The refractive index is that of the $LiNbO_3$ substrate.

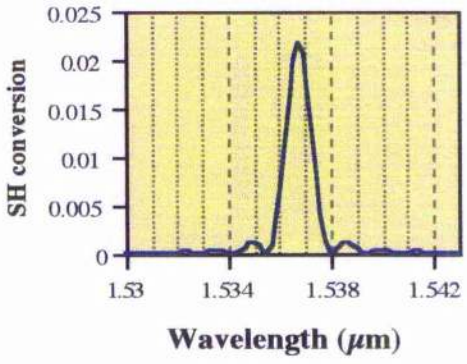

Fig 5.11. Dependency of the SH conversion efficiency as a function of the wavelength for the waveguide of Fig 5.7. For QPM domain reversal. The duty-cycle of domain reversal is 0.5. Δn^{ω}=0.000205, $\Delta n^{2\omega}$=0.000479, The substrate refractive indices corresponds to those of $LiNbO_3$. The effective area is $2{,}1 \times 10^{-7}$ and the input power at the fundamental wavelength is 100 W.

5.3. SHG in uniform PSWs.

Many authors believe that the propagation constant in a PSW is modulated along the waveguide, and propose to use this effect for SHG [5, 6], or even if they do not propose to use it, they study its repercussions in domain reversal SHG [7]. In opposition to this, we believe that a PSW sustains a mode, and that the propagation constant is characteristic of the mode, and therefore, is not modulated along the direction of propagation.

To our knowledge there is not a theoretical description of the detuning curves for waveguides with a modulation in the propagation constant (assuming the propagation constant can be modulated). In this section we will show the experimental detuning curves of a uniform PSW, and compare them with our theoretical detuning curves assuming:

- Domain reversal only,
- Domain reversal and modulation of the propagation constant,
- Modulation of the propagation constant only

We will show that the only possible way to reconcile experimental and theoretical results is by not considering a modulation in the propagation constant of the PSW.

5.3.1. Theoretical detuning curves.

The shape of the detuning curves depends on the length of the device, and on the conversion efficiency. The waveguides considered here are 9 mm long, with a conversion efficiency of about 1.7% with 100 W pump. Therefore, the effective area is 2.08×10^{-7} m^2 (see Appendix 7). The wavelength at which quasi-phase matching (QPM) takes place depends on the period and effective indices of the SH and fundamental. The device was designed to operate at 1.55 μm. At this wavelength, the QPM period is about 19 μm, depending on the fabrication conditions. Due to the diffused nature of the PSWs the average increase in the refractive index, and therefore, the propagation constant is difficult to obtain. For this reason, in this work, the difference in the refractive index between the SH and fundamental is a fitting parameter.

The detuning curve for a domain reversal waveguide has been shown in Fig 5.11. In this section we will concentrate on the effects that a modulation of the propagation constant will have on SHG.

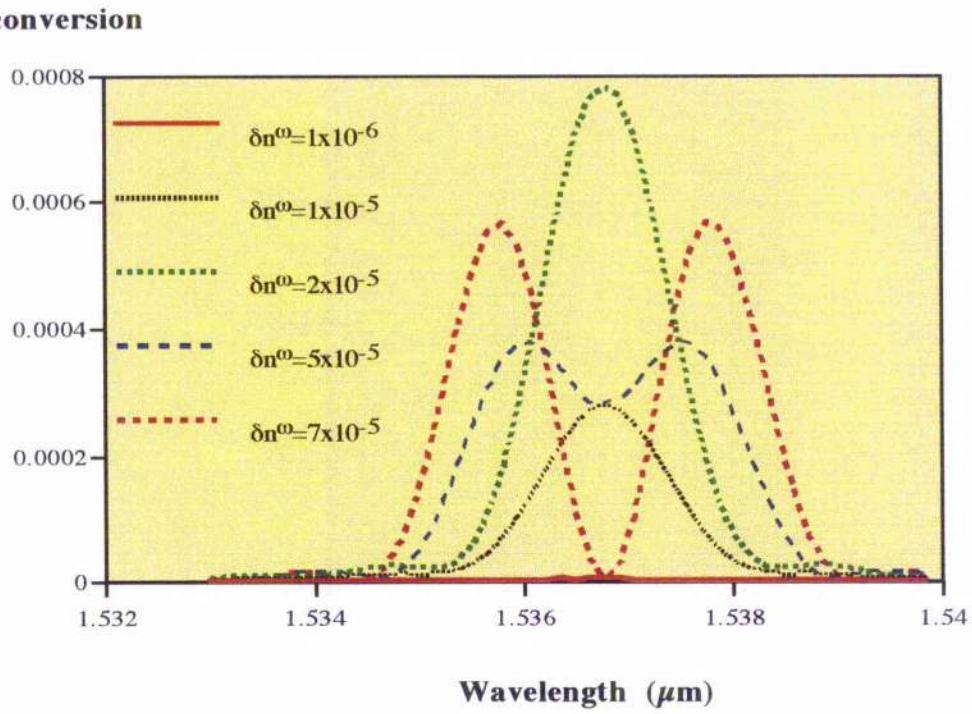

Fig 5.12. Detuning curves for waveguides where the propagation constant has been modulated. The same conditions as those of Fig 5.11, except for the modulation of the effective index and sign of the nonlinear coefficient. δn^{ω} and $\delta n^{2\omega}$ are the modulation in the effective index for the fundamental and SH respectively, we have set $\delta n^{2\omega} = 0$. The duty-cycle in the modulation of the effective index is 0.5. There is no modulation in the sign of the nonlinear coefficient. The effective area is $2.08 \times 10^{-7}\ m^2$. and the input power is 100 W. Δn^{ω}=0.000205 and $\Delta n^{2\omega}$=0.000479.

The detuning curves for the case where only the propagation constant is modulated can be seen in Fig 5.12. It is not shown here but the detuning curve depends on the difference in modulation of the propagation constants of the fundamental and SH and not on its individual values (i.e. the effect is due to the modulation of the phase mismatch, Δk). δn^{ω} and $\delta n^{2\omega}$ are the modulation in the effective index for the fundamental and SH respectively. To simplify we assume that $\delta n^{2\omega} = 0$. Therefore in Fig 5.12 δn^{ω} is an indication of the value of the difference between δn^{ω} and $\delta n^{2\omega}$. The first thing to be noticed is that if the difference between δn^{ω} and $\delta n^{2\omega}$ is large enough we have two peaks at which QPM takes place. One peak corresponds to

$$l_1 = l_c \qquad \text{Eq 5.21}$$

and the other to

$$l_2 = l'_c \qquad \text{Eq 5.22}$$

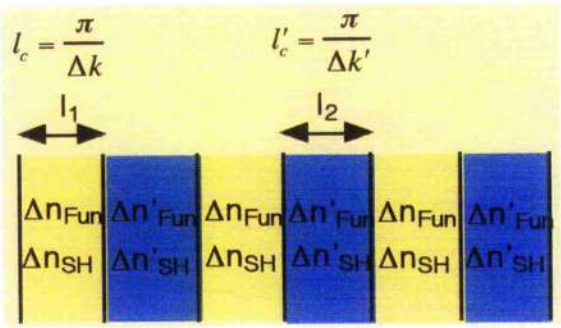

Fig 5.13. Condition for phase matching in a waveguide with a modulation of the phase mismatch.

The definitions of l_1, l_2, l_c, l'_c can be seen in Fig 5.13.

The second point we notice in Fig 5.12 is that a small modulation in δn^{ω} does not produce any significant SHG. As we increase δn^{ω} the efficiency increases up to a certain point, and then starts to decrease. If we increase δn^{ω} further the detuning curve splits in two.

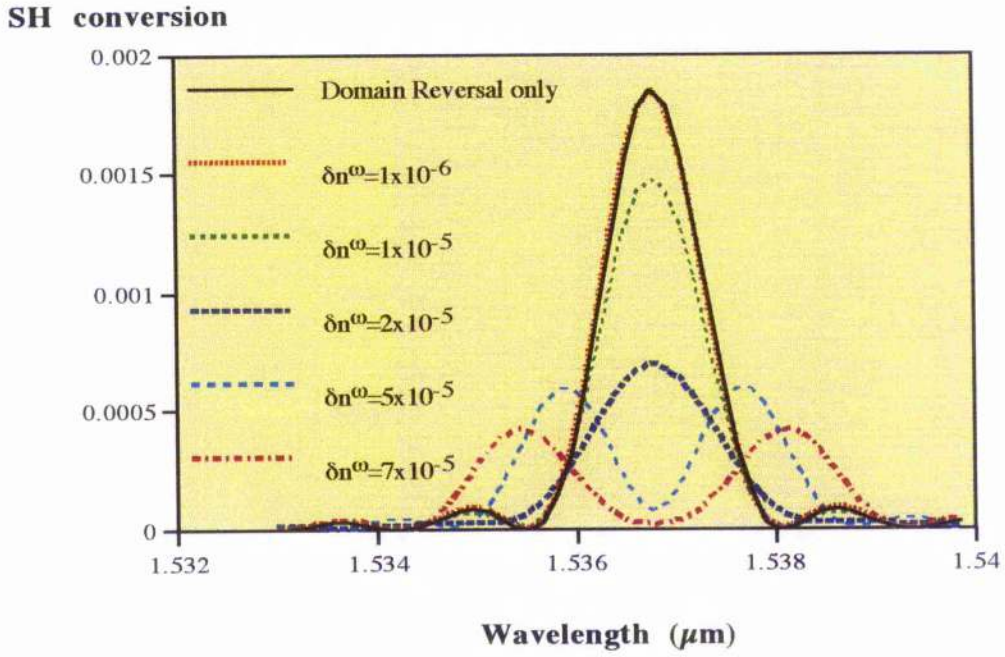

Fig 5.14. Detuning curves for waveguides where the propagation constant and the sign of the nonlinear coefficient had been modulated. Same conditions as those of Fig 5.11, except for the modulation of the effective index. $\delta\Delta n^{\omega}$ and $\delta\Delta n^{2\omega}$ are the modulation in the effective index for the fundamental and SH respectively, we have set $\delta\Delta n^{2\omega} = 0$. The duty-cycle in the modulation of the effective index and sign of the nonlinear coefficient is 0.5. The effective area is $2.08\times10^{-7}\ m^2$, and the input power is 100 W. Δn^{ω}=0.000205 and $\Delta n^{2\omega}$=0.000479.

The detuning curves for the case where we modulate both the phase mismatch and the sign of the nonlinear coefficient can be seen in Fig 5.14. As in Fig 5.12 we set $\delta n^{2\omega} = 0$ and vary δn^{ω}. The more efficient case corresponds to no modulation of the phase mismatch, as the modulation increases, the efficiency of the SHG process is reduced, and at a certain value of δn^{ω} the detuning curve shows two peaks.

5.3.2. Experimental results.

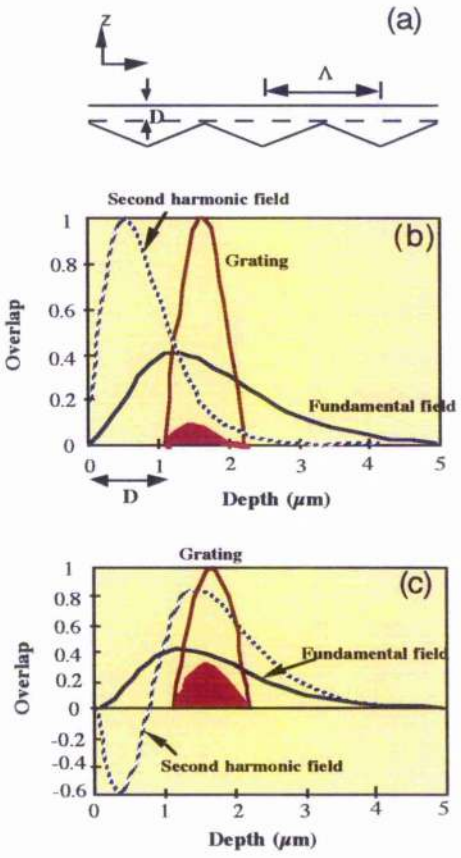

Fig 5.15. Schematic representation of a) the shape of the ferroelectric domain after Ti in-diffusion, and the overlap integral of the fundamental and SH modes with a function that described the spatial variation of the ferroelectric domain grating, for b) the SH in the TM_{00} mode and c) for the SH in the TM_{01} mode[8]

PSWs were fabricated in $LiNbO_3$ by in-diffusing 100 nm of Ti at 1050 °C for 13 hours. The Ti strips were patterned onto both positive and negative faces of the $LiNbO_3$ substrate, the segments were 5 μm wide, with periods ranging from 15.8 to 19.8 μm and duty-cycle of 0.55. For the case of the Ti in-diffused onto the negative z face, the Ti only increases the refractive index. For the case of Ti in-diffusion onto the positive face the indiffusion process increased the refractive index, and produced a reversal of the domain as described in Chapter 2 . Due to effects such as titanium lateral diffusion and lithium outdiffusion, the typical shape of the ferroelectric polarisation obtained is shown schematically in Fig 5.15. The net results are thus the combination of two homogeneous materials with opposite ferroelectric polarisations separated by a periodic boundary. Only the section of the fundamental and SH modes that propagate within the periodic boundary result in SHG.

At the SH wavelengths more than one mode ($TM_{00}^{2\omega}$, $TM_{01}^{2\omega}$, $TM_{02}^{2\omega}$, ...) are supported by the waveguide, and each of these modes can interact with the mode at the fundamental wavelength (TM_{00}^{ω}) to produce SHG:

$$TM_{00}^{\omega} + TM_{00}^{\omega} \Rightarrow TM_{00}^{2\omega}$$
$$TM_{00}^{\omega} + TM_{00}^{\omega} \Rightarrow TM_{01}^{2\omega}$$
$$TM_{00}^{\omega} + TM_{00}^{\omega} \Rightarrow TM_{02}^{2\omega}$$
$$\vdots$$

For a given period, QPM takes place at a different wavelength for each of the SH modes, since they have different propagation constants. The more efficient interaction is the one in which the overlap between the fundamental and SH is larger in the area where domain reversal exists. As we can see in Fig 5.15 the maximum overlap takes place for the $TM_{00}^{\omega} + TM_{00}^{\omega} \Rightarrow TM_{01}^{2\omega}$ interaction. In these situations, the effective area is the overlap integral between the fundamental mode, the SH modes and a function given by the grating [4].

All of the detuning curves and phase matching wavelengths were obtained by Carlos Treviño Palacios at CREOL, University of Central Florida. The laser source used in the experiments was a synchronously pumped mode-locked (F^{2+})NaCl:OH color-center laser operating in mode-locked (76 MHz, 6-ps pulses, assuming a Gaussian pulse Shape). The peak power of the laser was selected to avoid substantial mode competition between adjacent modes [9].

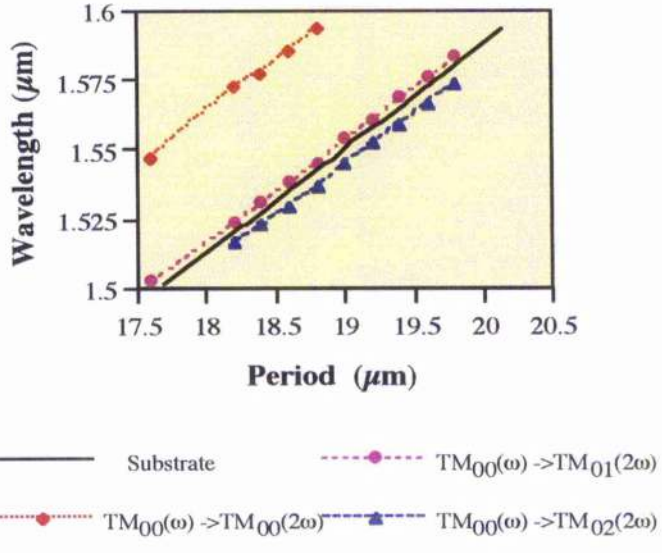

Fig 5.16. Wavelength at which QPM takes place for PSW with different periods but the same duty-cycle. The solid line represents the material dispersion of the SHG process.

In Fig 5.16 we can see the phase matching wavelength as a function of the period, for PSWs fabricated onto the positive face (domain reversal exists). Each discontinuous line corresponds to phase matching of the TM_{00}^{ω} mode width different modes of the SH. The solid line corresponds to the dispersion for the case where the fundamental and SH propagate in the substrate. As we can see the dispersion for

the guided modes and the substrate is the same. This can be used to design waveguides for different operating wavelengths. The average conversion efficiencies for these waveguides were 1.5 % with a 100 W pump (for 9 mm long waveguides), in this situation the effective area is $2.08 \times 10^{7}\ m^{2}$.

We propose two models to describe the index distribution in a PSW:

- Model 1. We assume that there is no diffusion in the direction of propagation, and that the diffusion underneath the Ti segments is that of a continuous waveguide (as described in section 2.3.1., Chapter 2). Then the increase in the refractive index is averaged along one period according to Eq 1.1 of Chapter 1. In this model we assume no increase in the refractive index between the Ti segments.

- Model 2. We calculate the Ti distribution after in-diffusion for one single segment. To do this we assume the diffusion has a Gaussian distribution in the depth direction and a Error function distribution in the lateral directions:

$$C(x,y,z) = C_o \exp\left(-\frac{z^2}{D_z^2}\right)\left[erf\left(\frac{W+2y}{2D_y}\right) + erf\left(\frac{W-2y}{2D_y}\right)\right]\left[erf\left(\frac{W+2x}{2D_x}\right) + erf\left(\frac{W-2x}{2D_x}\right)\right]$$

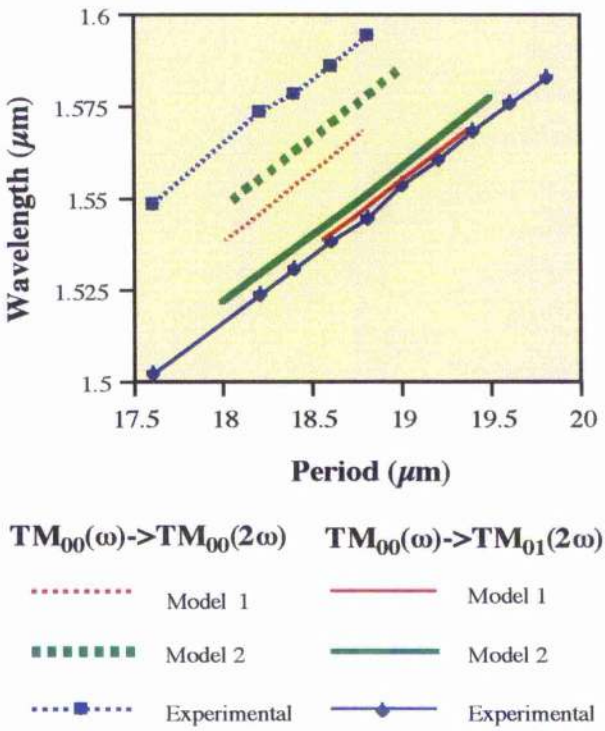

Fig 5.17. A comparison between the QPM wavelength obtained experimentally and that obtained using the models 1 and 2 described in the text.

C_0 is chosen so that the final total number of atoms of Ti are the same as the initial number of atoms. Then we average the Ti concentration along one period, and from this Ti distribution the index distribution is obtained using the equation of section 2.3.2.2. in Chapter 2.

In both models the effective index of the waveguide was obtained by entering the index distribution into a mode solver. In Fig 5.17, the results obtained from both models have been compared against the

experimental results. As we can see both models describe accurately the case of weakly guided modes, but they cannot be used to predict the QPM wavelength for the stronger confined modes. We believe that a more accurate model has to be developed to obtain the Ti distribution in PSWs, as well as a new relationship between the Ti concentration and the increase of the refractive index.

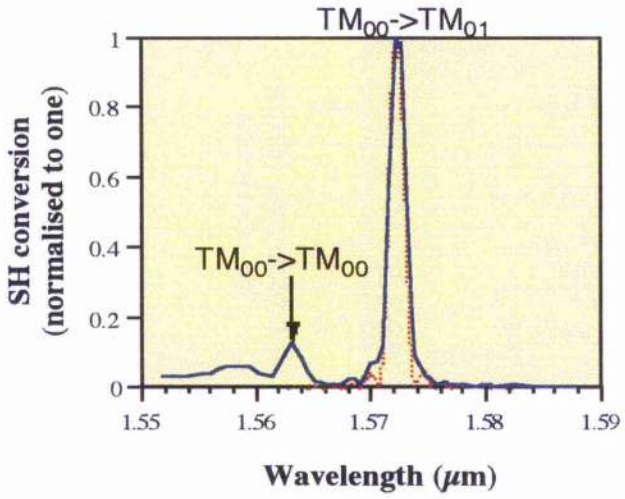

Fig 5.18. Typical SHG wavelength scan for a 0.9 mm long uniform PSW of period 19.5 μm and duty-cycle 0.55. The input power is 100 w and the effective area 2.1×10^{-7} m^2. The solid line represents the experimental result and the dotted line is the theoretical prediction. Assuming only a modulation on the sign of the nonlinear coefficient. The theoretical curve was displaced to the left by 2.32 nm to compensate for the discrepancy between the experimental and theoretical QPM wavelength of Fig 5.17

For the case of the $TM_{00}^{\omega} \rightarrow TM_{01}^{2\omega}$ interaction, the difference between the QPM wavelength obtained with model number 1 and that obtained experimentally is 2.32 nm, and from now on we will use this value to fit our model to the experimental results. No other fitting will be implemented.

A typical SHG wavelength scan can be seen in Fig 5.18 .We can see two different peaks corresponding to the interactions between the TM_{00} mode at the fundamental wavelength with two different modes at the SH wavelength. The height of the peaks depends on the effective area.

Using the same experimental set-up we were unable to find QPM SHG for Ti:$LiNbO_3$ PSW fabricated onto the negative face of the $LiNbO_3$ substrate (where domain reversal does not take place). Both, the waveguides fabricated onto the positive and negative face, were processed under exactly the same conditions.

5.3.3. Comparison of experimental and theoretical results.

After comparing the experimental and theoretical detuning curves, the following conclusions can be obtained:

1 QPM SHG is very different for PSWs fabricated on the positive and negative face of $LiNbO_3$. For waveguides fabricated on the positive face, the conversion efficiency was as big as 5%, while no QPM was observed in PSWs fabricated on the negative face. The QPM SHG obtained in the former case is due to domain reversal, and the mechanism for this can be seen in section 2.3.1.5. of Chapter 2.

2 The absence of QPM SHG for PSWs fabricated on the negative face of the $LiNbO_3$ substrate indicates that there is no modulation of the phase mismatch, or if there is any, it is small: $\delta(n^{2\omega}-n^{\omega})<1\times10^{-5}$ (see Fig 5.12). Here, $n_{2\omega}$ and n_{ω} are the effective indices at the SH and fundamental wavelength respectively, and $\delta(n^{2\omega}-n^{\omega})$ is the modulation in the difference. We were able to resolve QPM SHG 75000 times smaller than the input power at the fundamental wavelength. i.e. we should be able to detect QPM SHG with an efficiency of 0.0013 %.

3 The absence of two peaks in the detuning curve for the PSWs fabricated on the positive face of $LiNbO_3$ indicates that if there is any modulation of the phase mismatch, it is small: $\delta(n^{2\omega}-n^{\omega})<5\times10^{-5}$ (see Fig 5.14).

4 The absence of QPM SHG for PSWs fabricated on the negative face of $LiNbO_3$ indicates that neither of the following QPM SHG interactions take place :

$$TM_{00}^{\omega} + TM_{00}^{\omega} \Rightarrow TM_{00}^{2\omega}$$
$$TM_{00}^{\omega} + TM_{00}^{\omega} \Rightarrow TM_{01}^{2\omega}$$

and therefore the difference in modulation of the effective index of the TM_{00} and TM_{01} modes of the SH is smaller than 1×10^{-5}. This is a direct consequence of point 2 in this section. It is noted that the difference in the effective index between the TM_{00} and TM_{01} modes of the SH is 2.8×10^{-3}.

5 Fig 5.17 and Fig 3.4 of Chapter 3 indicate that there is a diffusion of Ti in the direction of propagation. We do not have a good model to describe the exact distribution of Ti concentration in PSWs, but from the results summarised in Fig 5.17, the TM_{00} and TM_{01} modes of the SH "see" different distributions of Ti concentrations. The TM_{00} mode of the SH appears to "see" a smaller duty-cycle than the TM_{01} mode. Due to the diffuse nature of the Ti:$LiNbO_3$ waveguides, we expect the TM_{00} mode of the SH to "see" a larger modulation of the refractive index than the TM_{01} mode.

6 If we put all the above points together we can conclude that the modulation in the phase mismatch is very small: $\delta(n^{2\omega}-n^{\omega})<1\times10^{-5}$. We can also conclude that the difference in the modulation of the propagation constant of the TM_{00} and TM_{01} modes of the SH is very small: $\delta n_{00}-\delta n_{01}<1\times10^{-5}$, despite the large difference between the effective indices of these two modes ($n_{00}-n_{01}=0.0028$). The reasons for this can be:

- The modulation of the propagation constant is the same for all modes and wavelengths involved. But there is evidence that indicates a different modulation of the refractive index for different modes.
- The modulation of the propagation constant is very small for all modes due to the reduction in the modulation of the refractive index as a consequence of the diffusion of Ti along the direction of propagation. But, again we have evidence that indicates that the TM_{00} mode of the SH may "see" a significant modulation of the refractive index.
- There is no modulation in the propagation constant of the PSWs modes.

At this point we cannot say which of these three situations occurs in our experiments. The only thing that the experimental detuning curves indicates is that, to the accuracy of our experimental set-up, the PSWs described in this Chapter behave as continuous waveguides in QPM SHG, and therefore in any other phase matching experiments.

5.4. Tuning curves of chirped PSWs.

In this section we will show the tuning curves obtained for chirped waveguides. In all of the analysis, we do not assume a modulation in the propagation constant.

Chirped waveguides have many applications. By making the bandwidth broader the device can compensate for changes of the working conditions and uncertainty due to the fabrication process. As well as controlling the bandwidth, chirped waveguides can be used to reduce the side lobes of any grating assisted coupling, and for the particular case of SHG, chirped waveguides can be used to generate a large nonlinear phase shift (due to cascaded second order nonlinearities[10]), in a region where the power of the fundamental is not depleted by SHG.

To fabricate the chirped waveguide, the total length of the device was divided in 30 or 60 different sections, where each section is formed by uniform PSWs with a period depending on the position of the section in the waveguide. To work on the

centre of the tuning range of the laser, the chirped PSW had an starting period of 18.5 μm and a final period of 19.5 μm.

We fabricated PSWs with three different period distributions:

- 1 cm long quadratic chirp waveguide. Starting period 18.5 μm final period 19.5 μm. The spatial distribution of the periods can be seen in Fig 5.19

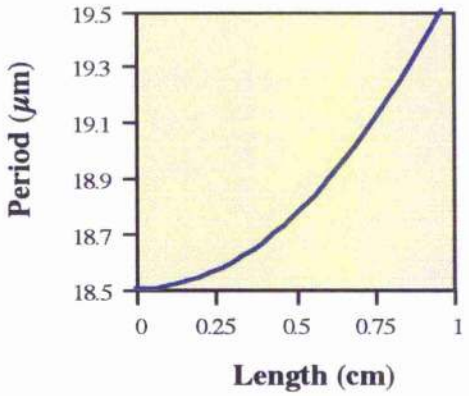

Fig 5.19

- 0.5 cm long quadratic chirp waveguide, starting period 18.5 μm final period 19.5 μm, followed by 0.5 cm long uniform PSW of period 19.5 μm. The spatial distribution of the periods can be seen in Fig 5.20

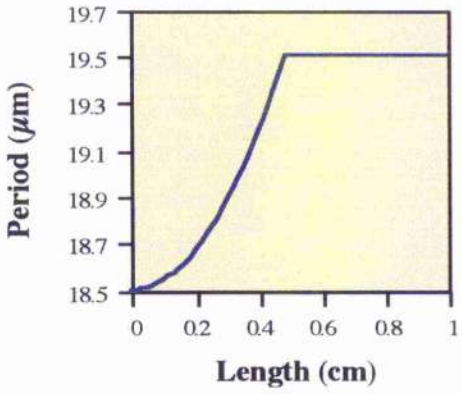

Fig 5.20.

- 0.5 cm long quadratic chirp waveguide, starting period 18.5 μm final period 19.5 μm, followed by 0.5 cm long uniform PSW of period 19 μm. The spatial distribution of the periods can be seen in Fig 5.21

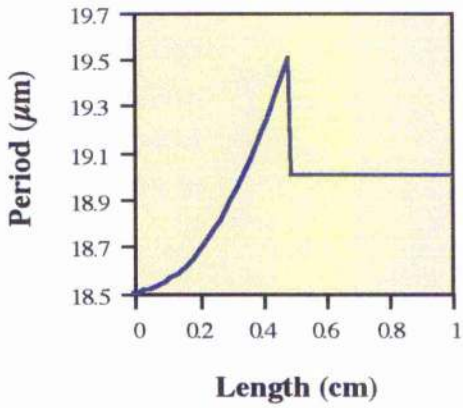

Fig 5.21.

The waveguides were fabricated by patterning 100 nm of Ti into the positive face of z-cut $LiNbO_3$, and diffused at 1050 °C for 13 hours. As a consequence of the cutting /polishing process, the final length of the devices was shorter than the nominal one, about 1 mm shorter. This problem could be avoided by fabricating an input/output (I/O) section with the same duty-cycle and a different period than that required for SHG. In this situation there is good coupling between the I/O section and the remainder of the waveguide, and SHG is inhibited in the I/O section.

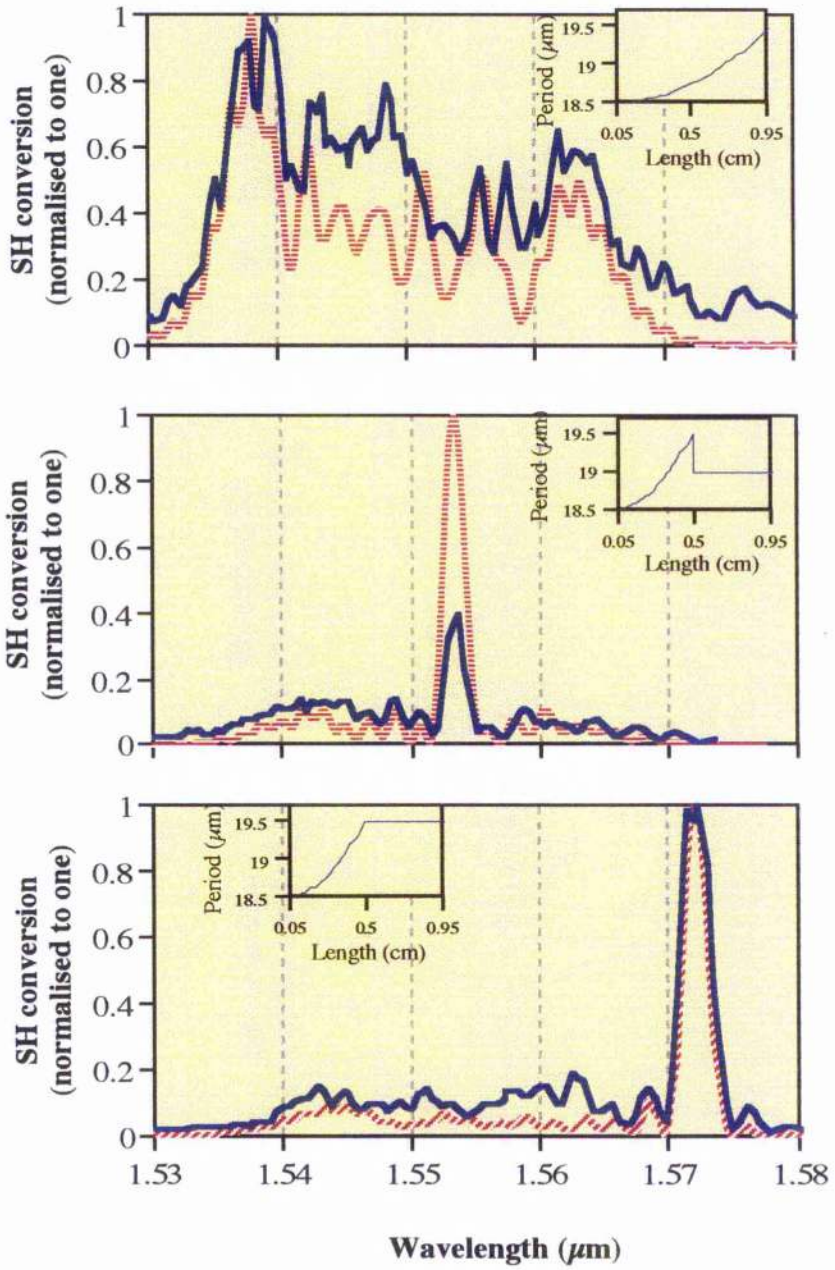

Fig 5.22. Wavelength scan for SHG in chirp waveguides. The spatial distribution of the period for each waveguide can be seen in the insert. The solid line corresponds to experimental measurements and the dotted lines are the numerical simulations

The experimental detuning curves for the chirped waveguides together with the ones obtained by solving the coupled differential equation of Eq 5.4 can be seen in Fig 5.22. To obtain the theoretical curves we assumed that our waveguides were 0.9 cm long (0.5 mm was removed from each end by polishing). The effective area was calculated from the efficiency of the experimental process. The propagation constant for the fundamental and SH were obtained with a mode solver using an average Ti concentration as described by model 1 in section 5.3.2. of this Chapter, and then the curves were shifted 2.32 nm to the left to compensate for the discrepancies between the predicted and actual values of the phase matching wavelength in Fig 5.17 . The duty cycle was set to be 0.55.

The agreement between experimental and theoretical results indicates that is possible to design and fabricate chirped waveguides to meet specific need. However, there are certain differences between the experimental and theoretical results. From our simulation, the relative position of all the other features of the tuning curves are very dependent on properties of the waveguide such as:

- Difficulty to precisely determine the length of the waveguide and dependency of the detuning curve on input the coupling; Which can be solved by introducing a I/O section
- Mode competition, as at certain wavelengths more than one mode may be excited [6]. A more complex model has to be implemented to account for this.
- Phase errors introduced during fabrication.

The experimental detuning curves were obtained with 6 ps pulses, that for the case of a transform limited Gaussian pulse have an approximately bandwidth of 0.6 nm. While the theoretical detuning curves were solved for one of the Fourier components, i.e. an infinitely small bandwidth.. This is not of great consequence to the results of Fig 5.22, as the theoretical detuning curves do not experience a large variation in conversion efficiency within 0.6 nm.

To investigate the influence of the number of sections with different periods in which a chirp waveguide is divided, we fabricated chirp PSWs with 30 and 60 different periods. The wavelength scan of this waveguide can be seen in Fig 5.23. The spatial distribution of the period can be seen in the insert, the chirp region corresponds to the first 5 mm of the waveguide. The agreement between both sets of results indicates that only 30 different periods are required to generate the spectrum of a chirp waveguide. This is in agreement with our numerical simulation.

A quadratic chirp is very attractive for all-optical switching. In a second order nonlinear interaction, at the phase matching condition we have conversion from the fundamental to the SH, as we depart from this condition the SH reconverts to the fundamental and this process is associated with a nonlinear phase shift of the fundamental [6]. For efficient all-optical switching to take place, a large nonlinear phase shift has to exist at a wavelength were the conversion to the SH is small.

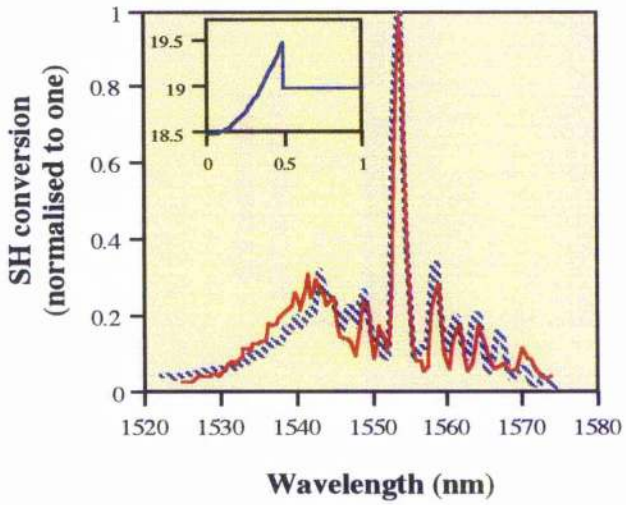

Fig 5.23. Wavelength scan for SHG in chirp PSW, the period distribution along the waveguide can be seen in the insert. The chirp section consist of 30 (continuous line) and 60 (dotted line) different periods.

As the SHG efficiency increases, the side lobes of a uniform PSW increase. To avoid loss of the signal to the SH we have to operate relatively far away from phase matching. But here the nonlinear phase shift is small, this can be seen in Fig 5.24 . To avoid this problem we can use a chirped waveguide, which reduces the size of the side lobes, but still maintains a large nonlinear phase shift. The different chirp structures under consideration can be seen in Fig 5.24 . These results were produced by the same numerical simulation used to predict the conversion efficiency in Fig 5.22.

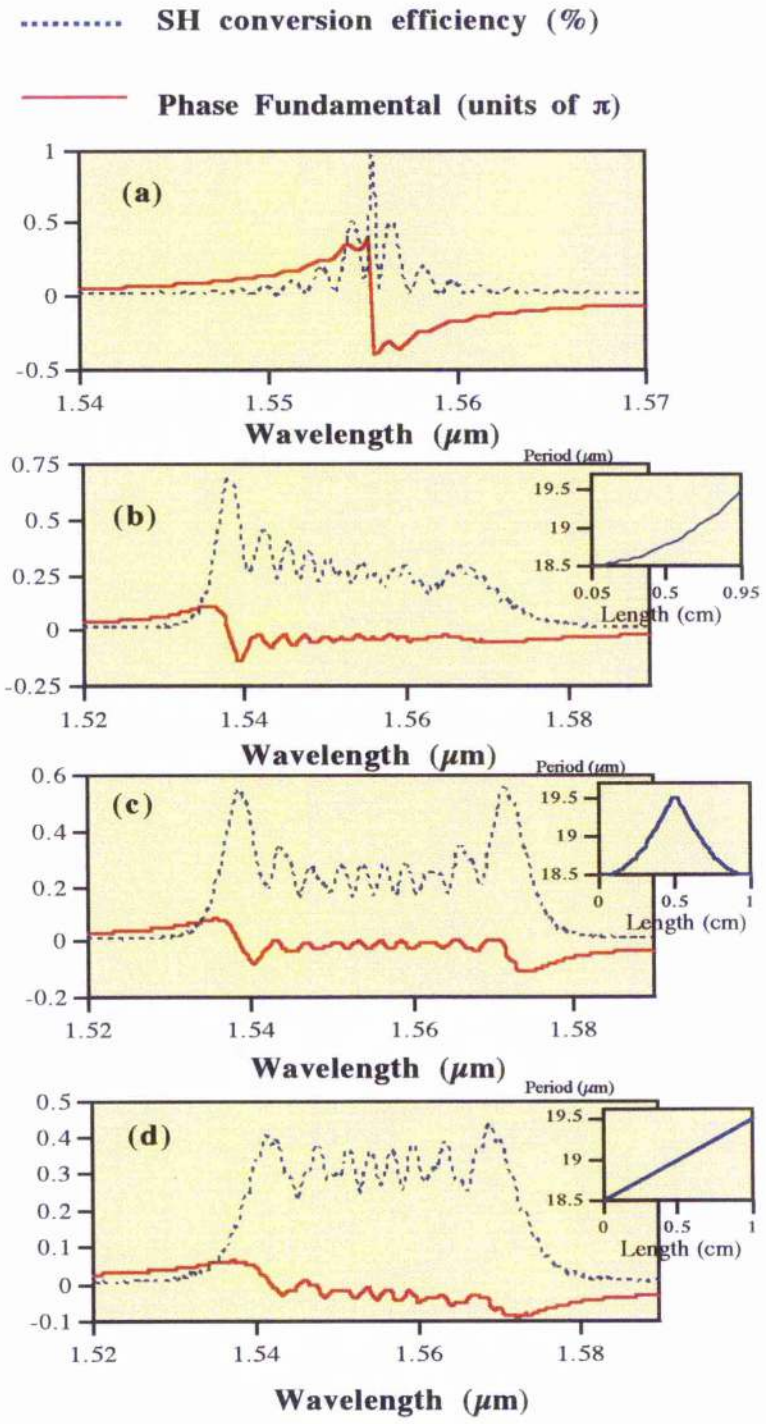

Fig 5.24. Detuning curves obtained by numerically solving the coupled differential equations that govern SHG (Eq 5.4) for (a) a uniform PSW and (b)(c)(d) different chirp PSWs. The period distribution can be seen in the insert. The solid lines corresponds to the nonlinear phase shift experiences by the fundamental frequency and the dotted line is the power conversion efficiency. The parameters in this simulation are the same as those used before in Fig 5.22, the only difference is that the waveguides are 1 cm long and the effective area is 3.5×10^{-10} m^{-2} to increase the conversion efficiency.

5.5. Conclusion.

We have generated a novel condition for up-conversion and down conversion in SHG that can be applied to any circumstance.

We were able to obtain SHG at about 1.55 μm using Ti:$LiNbO_3$ PSWs fabricated onto the positive face of $LiNbO_3$. None of the effects resulting from a modulation of the propagation constant could be measured; We did not observe QPM SHG in waveguides fabricated on the negative face of $LiNbO_3$. No deviation in the shape of the detuning curves from that predicted by a purely domain reversal SHG interaction was observed To the resolution of our measurements, any phase matching process in $LiNbO_3$ follows the same mechanisms as any continuous waveguide.

We observed that the dispersion of the phase matching wavelength is that of the $LiNbO_3$ substrate, therefore, once we know the phase matching wavelength for one period, for one set of fabrication conditions, we can obtain the phase matching wavelength for a different period. Waveguides fabricated independently, but with the same fabrication conditions, have the same phase matching wavelength.

The set of partial differential equations used to describe SHG, and the method employed to solve them has proven accurate in predicting the detuning curves of QPM SHG for uniform and chirped periods. We have shown that we can fabricate and model chirped waveguides. These chirped waveguides can be used in all-optical switching (based on cascaded second order nonlinearity) to reduce the losses of the signal to the SH and still maintain large nonlinear phase shift.

5.6. References.

[1]Z Weissman, A Hardy, M Katz, M Oron, and D Eger, "Second harmonic generation in Bragg-resonant quasi-phase matched periodically segmented waveguides", Optics Letters, **20**, pp. 674-676, (1995).

[2] J Khurgin, S Colak, R. Stolzenberg, and R N Bhargava, "Mechanism for efficient blue second-harmonic generation in periodically segmented waveguides", Appl.. Phys. Lett., **57**, pp. 2540--2542, (1990).

[3] C Q Xu, H Okayama, and M Kawahara, "Optical Frequency Conversion in Nonlinear Medium with Periodically Modulated Linear and Nonlinear Optical Parameters", IEEE J Quantum Electron., **31**, pp. 981--987, (1985)

[4] M M Fejer, G A Magel, D H Jundt, and R L Byer, "Quasi-Phase-Matched Second Harmonic Generation: Tuning and Tolerances", IEEE J Quantum Electron., **28**, pp. 2631--2654, (1992)

[5] J Khurgin, S Colak, R. Stolzenberg, and R N Bhargava, "Mechanism for efficient blue second-harmonic generation in periodically segmented waveguides", Appl.. Phys. Lett., **57**, pp. 2540--2542, (1990).

[6] C Q Xu, H Okayama, and M Kawahara, "Optical Frequency Conversion in Nonlinear Medium with Periodically Modulated Linear and Nonlinear Optical Parameters", IEEE J Quantum Electro., **31**, pp. 981--987, (1985)

[7]M M Fejer, G A Magel, D H Jundt, and R L Byer, "Quasi-Phase-Matched Second Harmonic Generation: Tuning and Tolerances", IEEE J Quantum Electro., **28**, pp. 2631--2654, (1992)

[8] M L Bortz, S J Field, M M Fejer, D W Nam, R G Waarts, and D F Welch, "Noncritical quasi-phase matched second harmonic generation in an annealed proton-exchange $LiNbO_3$ waveguide", IEEE Transactions on Quantum electronics, **30**, no 12, pp. 2953--2960, 1994.

[9] C G Trevino-Palacios, G I Stegeman, M P De Micheli, P Baldi, S Nouch, D B Ostrowsky, D Delacourt, and M Papuchon, Appl. Phys. Lett. **67**, (1995).

[10]G. I. Stegeman, D. J. Hagan, and L. Torner, "$\chi^{(2)}$ cascading phenomena and their applications to all-optical signal processing, mode-locking, pulse compression and solitons", Optical and Quantum Electronics, **28**, pp. 1691--1740, (1996).

6

Conclusions

We were able to fabricate Ti:$LiNbO_3$ PSWs for different fabrication conditions, with duty cycles ranging from 0.3 to 0.65, and periods ranging from 15 μm to 20 μm (Chapter 3). In all these cases the cut-off wavelength of the PSWs had been predicted. The model used represented the PSWs by a continuous waveguide with the same width and height as the PSW, but in which the average index difference, $\Delta n'$, is given by Eq 6.1:

$$\Delta n' = \eta \Delta n \qquad \text{Eq 6.1}$$

where η is the duty-cycle and Δn is the increase in the refractive index due to Ti indiffusion. In the case of step index waveguides, Eq 6.1 represents the weighted average of the index along the direction of propagation. In Chapter 4 we have shown that the mode size of a PSW and its equivalent continuous waveguide are the same for the case of step index waveguides. But, for diffused waveguides, for example Ti:$LiNbO_3$, Eq 6.1 can only be used in certain cases. In Chapter 5 we have shown that Eq 6.1 can only be applied to the case of weakly guided modes. To use Eq 6.1 in the context of Ti:$LiNbO_3$ waveguides, we assume no titanium diffusion in the direction of propagation, and a invariant index distribution in the cross section underneath the Ti segments (model 1 of section 5.3.2., Chapter 5). A more accurate model will need to include the diffusion in the direction of propagation. In Chapter 5 we have shown that it is difficult to obtain the Ti distribution, and therefore the average index distribution cross section of PSWs. We have shown that the models available cannot be applied to PSWs. In this work we have shown that Eq 6.1 can be applied to PSWs with periods between 15 and 30 μm and duty-cycles ranging from 0.2 to 1. In the case of diffused waveguides, Eq 6.1 can only be used for weakly guides modes and in the case of step index waveguides Eq 6.1 can be used at least for a Δn=0.02.

In Chapter 3, we noticed that the reduction in the cut-off wavelength due to the segmentation, has to be considered to fabricate waveguides that guide at given wavelengths and polarisation.

The equivalent continuous model of PSWs can be used to describe all of the properties of PSWs except for the segmentation losses. Using a 3D FD BPM we were able to show that PSWs maintain "modes" and we were able to estimate the segmentation losses for step index PSWs. We have demonstrate that the "modes" of PSWs are a three dimensional function, and correspond to the optical field distribution in one period of a PSW. We have shown that a 3D representation of the PSWs is necessary to evaluate the radiation losses, both in towards the substrate and in the lateral direction.

Using quasi-phase matched SHG we have investigated the linear behaviour of PSWs. To the resolution of our experiments, the PSWs described in Chapter 5 behave as continuous waveguides in QPM SHG, and therefore in any other phase matched experiments. We also demonstrated how the period of the PSWs can be chirped to modify the phase matching curves.

The control of the refractive index with the duty-cycle, and the phase matching wavelength with the period, make PSWs an attractive component of integrated optical circuits.

Appendix. 1

Noncentrosymmetric crystals and second order nonlinearities.

Part 1.

Here we are going to discuss the conditions in which the nonlinear coefficients are zero.

From symmetry considerations, in the case of centrosiymetric material the electric field of the EM wave and the components of the nonlinear polarisation wave createed have the following relationship:

$$\begin{aligned} E_x &= -E_x \qquad p_x = -p_x \\ E_y &= -E_y \qquad p_y = -p_y \\ E_z &= -E_z \qquad p_z = -p_z \end{aligned} \qquad \text{Eq A1.1}$$

Where E_x, E_y, E_z, p_x, p_y, p_z are defined in Chapter 2, section 2.2.5. The nonlinear polarisation is given by:

$$p_p^{NL} = 2\varepsilon_0 d_{pqr} E_q E_r \qquad \text{Eq A1.2}$$

$$p = x, y, z$$
$$q = x, y, z.$$
$$r = x, y, z$$

In the case of centrosymmetric crystals, using Eq A1.1 and A1.2 we obtain:

$$p_p^{NL} = 2\varepsilon_0 d_{pqr}\left(-E_q\right)\left(-E_r\right) \qquad \text{Eq A1.3}$$

Since Eq A1.2 and A1.3 describe the same process, then

$$d_{pqr} = -d_{pqr} \qquad \text{Eq A1.4}$$

and therefore $d_{pqr}=0$

Crystals with 3m point group symmetry (case of $LiNbO_3$) are centrosymmetric in the x direction and noncentrosymmetric in the y and z direction, as discussed in Chapter 2, section 2.2.2. Therefore

$$\begin{aligned} E_x &= -E_x \qquad p_x = -p_x \\ E_y &\neq -E_y \qquad p_y \neq -p_y \\ E_z &\neq -E_z \qquad p_z \neq -p_z \end{aligned} \qquad \text{Eq A1.5}$$

Therefore:

$$\left.\begin{aligned} p_x^{NL} &= 2\varepsilon_0 d_{xxx} E_x E_x \\ -p_x^{NL} &= 2\varepsilon_0 d_{xxx}(-E_x)(-E_x) \end{aligned}\right\} \Rightarrow \quad d_{xxx} = 0$$

$$\left.\begin{aligned} p_x^{NL} &= 2\varepsilon_0 d_{xyy} E_y E_y \\ -p_x^{NL} &= 2\varepsilon_0 d_{xyy} E_y E_y \end{aligned}\right\} \Rightarrow \quad d_{xyy} = 0 \qquad \text{Eq A1.6}$$

$$\left.\begin{aligned} p_z^{NL} &= 2\varepsilon_0 d_{zzz} E_z E_z \\ p_z^{NL} &= 2\varepsilon_0 d_{zzz} E_z E_z \end{aligned}\right\} \Rightarrow \quad d_{xyy} \neq 0$$

The remaining nonlinear coefficients can be obtained in the same form.

Since no physical significance can be attached to an exchange of E_q and E_r in Eq A1.2, it follows that $d_{pqr}=d_{prq}$. We therefore can replace the subscripts "qr" by a single symbol according to the piezoelectric contraction.

xx=1 yy=2 zz=3 yz=zy=4 xz=zx=5 xy=yx=6 Eq A1.7

Part 2.

Here we are going to discuss the sign of the nonlinear coefficient in $LiNbO_3$ domains with different orientations.

For a crystal with 3m point group symmetry:

$$\begin{aligned} E_x^+ &= E_x^- \qquad p_x^+ = p_x^- \\ E_y^+ &= -E_y^- \qquad p_y^+ = -p_y^- \\ E_z^+ &= -E_z^- \qquad p_z^+ = -p_z^- \end{aligned} \qquad \text{Eq A1.8}$$

as discussed in Chapter 2, section 2.2.2. The subscripts "+" and "-" represents domains with one orientation and the opposite. Then , using Eq A1.2 and Eq A1.8 we have

$$\left.\begin{aligned} p_x^- &= 2\varepsilon_0 d_{xxz} E_x^+ E_z^+ \\ p_x^- &= 2\varepsilon_0 d_{xxz} E_x^- \left(-E_z^-\right) \end{aligned}\right\} \Rightarrow \begin{cases} d_{xxz}^+ = d_{xxz}^- \\ d_{15}^+ = d_{15}^- \end{cases}$$

$$\left.\begin{aligned} p_y^+ &= 2\varepsilon_0 d_{yyy} E_y^+ E_y^+ \\ \left(-p_y^-\right) &= 2\varepsilon_0 d_{yyy}\left(-E_y^-\right)\left(-E_y^-\right) \end{aligned}\right\} \Rightarrow \begin{cases} d_{yyy}^+ = d_{yyy}^- \\ d_{22}^+ = d_{22}^- \end{cases} \qquad \text{Eq A1.9}$$

$$\left.\begin{aligned} p_z^+ &= 2\varepsilon_0 d_{zzz} E_z^+ E_z^+ \\ \left(-p_z^-\right) &= 2\varepsilon_0 d_{zzz}\left(-E_z^-\right)\left(-E_z^-\right) \end{aligned}\right\} \Rightarrow \begin{cases} d_{zzz}^+ = d_{zzz}^- \\ d_{33}^+ = d_{33}^- \end{cases}$$

Appendix 2

Derivation of the Fresnel equation.

Maxwells equations in an linear and isotropic medium, with no free charges, and with no sources of electromagnetic (EM) waves (we assumed the EM waves are produced by a distant source of accelerated charges : $\rho=(\underline{r},t)$ and $J(\underline{r},t)$) are as follow

$$\underline{\nabla}\times\underline{H}=\underline{J}+\frac{\partial\underline{D}}{\partial t}\quad(\underline{J}=\sigma\underline{E})$$

$$\underline{\nabla}\times\underline{E}=-\mu\frac{\partial\underline{H}}{\partial t}$$

$$\underline{\nabla}\cdot(\varepsilon\underline{E})=\rho\quad(\rho=0,\quad\text{no free charges})\qquad\text{Eq A2.1}$$

$$\left(\underline{D}=\varepsilon\underline{E},\quad\varepsilon=\varepsilon_0\varepsilon_r\right)$$

We have consider that the only current density, $\underline{J}$, is due to the passive response of a ohmic medium to the electric field of the EM field. In isotropic waveguides the relative permittivity and relative permeability are not tensors but scalars. From Maxwells equations the following vectorial wave equation can be obtained [1]:

$$\underline{\nabla}^2\underline{E}-\mu\varepsilon\frac{\partial^2\underline{E}}{\partial t^2}-\sigma\mu\frac{\partial\underline{E}}{\partial t}=-\underline{\nabla}\left(\frac{1}{\varepsilon}\underline{E}\underline{\nabla}\varepsilon\right)\qquad\text{Eq A2.2}$$

An overview of the different vectorial equations used to study waveguides can be found in Reference [1].

The term,

$$-\underline{\nabla}\left(\frac{1}{\varepsilon}\underline{E}\underline{\nabla}\varepsilon\right),\qquad\text{Eq A2.3}$$

accounts for the polarisation properties of the waveguide by virtue of its cross-section geometry and refractive index profile. This term is responsible for the hybrid modes. Ignoring this term completely disregards the polarisation properties of the

waveguide structure and leads to the scalar wave equation [2]. In homogeneous regions this term is zero, however, the term is non-zero along material interfaces.

If we assume the field varies as

$$\underline{E}(x,y,z,t) = \mathrm{Re}\left[\underline{E}(x,y,z)\exp(i\omega t)\right] \qquad \text{Eq A2.4}$$

and if we neglect the term given in Eq A2.3 in Eq A2.2, we obtain the Helmholtz equation (scalar wave equation)

$$\nabla^2 \underline{E} + k^2(\underline{r},\omega)\underline{E} = 0 \qquad \text{Eq A2.5}$$

where we assumed $\underline{\nabla}^2 = \nabla^2$, which is true if the electric field $\underline{E}$ have Cartesian co-ordinates . k is the propagation constant of the mode, given by:

$$k^2(\underline{r},\omega) = \omega^2\mu\varepsilon(\underline{r},\omega) + i\omega\mu\sigma(\underline{r},\omega) \qquad \text{Eq A2.6}$$

Here we allowed a possible dependency of ε on the position $\underline{r}$. The complex term in k^2 indicates that the material present some losses (σ>0) or gain (σ<0). Most commonly, k is expressed in terms of the refractive index "n" as:

$$k^2(\underline{r},\omega) \equiv k_0^2 n^2(\underline{r},\omega) \qquad \text{Eq A2.7}$$

where

$$k_0 \equiv \frac{\omega}{c} = \frac{2\pi}{\lambda_0} \qquad \text{Eq A2.8}$$

and

$$n^2(\underline{r},\omega) \equiv \frac{\varepsilon(\underline{r},\omega)}{\varepsilon_0} + i\frac{\sigma}{\omega\varepsilon_0} \qquad \text{Eq A2.9}$$

In the case of dielectrics σ=0, and therefore the refractive index is

$$n^2(\underline{r},\omega) \equiv \frac{\varepsilon(\underline{r},\omega)}{\varepsilon_0} \qquad \text{Eq A2.10}$$

But, even if σ=0 is zero, we have to remember that the permittivity, ε, has a complex component which introduce a complex term in "k" of Eq A2.5 and therefore losse (or material absorption). However, if we operate at a wavelength away from the resonance of the material this component is zero and absorption does not take place.

In the remainder of the Appendix, we assume that σ=0 and that we are away from material resonances, and therefore losses do not accur.

To solve Eq A2.5, we need some boundary conditions. The kind of boundary conditions we are considering is that of a nearly plane wave in which the flow of energy is predominantly along a single direction (+z in this case). Then, we can limit our derivation to a single transverse field component E, taking E as

$$E = \psi(x,y,z)\exp(-ik_r z) \qquad \text{Eq A2.11-a}$$

$$k_r = \frac{n_r \omega}{c} \qquad \text{Eq A2.11-b}$$

Where k_r is the average propagation constant of the electric field distribution (when propagating through the waveguide). If a small number of propagating modes is of interest, the effective propagation constant (k_r) should be chosen to be representative of this subset.

Then, the electric field that we are propagating has the following expression

$$\underline{E}(x,y,z,t) = \psi(x,y,z)\exp\left(i(\omega t - k_r z)\right)\hat{u} \qquad \text{Eq A2.12}$$

Where $\hat{u}$ is the unitary vector in the direction of the component that we are propagating.

By substituting $E = \psi(x,y,z)\exp(-ik_r z)$ into the scalar form of the Helmholtz equation (Eq A2.5), we obtain

$$2jk_0 n_r \frac{\partial \psi}{\partial z} = \frac{\partial^2 \psi}{\partial x^2} + \frac{\partial^2 \psi}{\partial y^2} + k_0^2\left(n^2(x,y,z,\omega) - n_r^2\right)\psi + \frac{\partial^2 \psi}{\partial z^2} \qquad \text{Eq A2.13}$$

and assuming that the longitudinal variation is slow enough that

$$k_r \frac{\partial \psi}{\partial z} \rangle\rangle \frac{\partial^2 \psi}{\partial z^2}$$
$$k_r^2 \frac{\partial \psi}{\partial z} \rangle\rangle \frac{\partial^2 \psi}{\partial z^2} \qquad \text{Eq A2.14}$$

we obtain the Fresnel equation or the paraxial wave equation for polarisation elements of the electric field

$$\boxed{-2jk_0 n_r \frac{\partial \psi}{\partial z} + \frac{\partial^2 \psi}{\partial x^2} + \frac{\partial^2 \psi}{\partial y^2} = -k_0^2 \left(n^2(x,y,z,\omega) - n_r^2 \right) \psi} \qquad \text{Eq A2.15}$$

The Fresnel equation correctly describes waves with a relatively small angular spread, $\delta\theta \approx 15°$ [3], about a direction $\theta \approx \cos^{-1}\left(k_r / k_{max}\right)$ with respect to the optical axis. We will refer to n_r as the reference refractive index, which will take the value of the refractive index of the substrate. $n(x,y,z,\omega)$ represents the index profile of the waveguide for a given frequency. To include larger angular spread (wide angle scalar wave equation) the second derivative of ψ with z in Eq A2.13 has to be included.

[1] K S Chiang, "Review of numerical and approximate methods for the modal analysis of general optical dielectric waveguides", Optical and Quantum Electronics, **26**, pp s113--s134, (1994).
[2] A. W. Snyder and J D Love, "Optical waveguide theory", J W Arrowsmith Ltd. Bristol, 1983.
[3] D Yevick, " A guide to electric field propagation techniques for guide-wave optics", Optical Quant. Electron., **26**, pp. s185-s197, (1994)

Appendix 3

Slowly Varying Envelope Approximation

The propagation of light in structures with second order nonlinear effects can be studied using a system of coupled differential equations. This system of equations is derived from Maxwell's Equations using a number of approximations.

Maxwell's equations in an linear and isotropic medium, with no free charges, and with no sources of electromagnetic (EM) waves (we assumed the EM waves are produced by a distant source of accelerated charges : $\rho=(\underline{r},t)$ and $J(\underline{r},t)$) are as follows

$$\underline{\nabla}\times\underline{H}=\underline{J}+\frac{\partial\underline{D}}{\partial t}\quad(\underline{J}=\sigma\underline{E})$$

$$\underline{\nabla}\times\underline{E}=-\mu\frac{\partial\underline{H}}{\partial t}$$

$$\underline{\nabla}\cdot(\varepsilon\underline{E})=\rho\quad(\rho=0,\quad\text{no free charges})\qquad\text{Eq A3.1}$$

$$\left(\underline{D}=\varepsilon\underline{E}+\underline{p}^{NL},\quad\varepsilon=\varepsilon_0\varepsilon_r\right)$$

We have consider that the only current density $\underline{J}$ is due to the passive response of an ohmic medium to the electric field of the EM field. In anisotropic waveguides the relative permittivity and relative permeability are not tensors but scalars.

If we only use one of the Fourier components of $\underline{E}(x,y,z,t)$:

$$\underline{E}(x,y,z,t)=\underline{E}^{\omega}(x,y,z)\exp(-i\omega t)\qquad\text{Eq A3.2}$$

Then the following wave equation can be obtained

$$\nabla^2\underline{E}^{\omega}=\underline{E}^{\omega}\left[-i\omega\mu_0\sigma-\omega^2\mu_0\varepsilon\right]-\mu_0\omega^2\underline{p}^{NL}(\omega)\qquad\text{Eq A3.3}$$

We assume we have a **forward propagating EM plane wave** (propagating in the +z direction):

$$\underline{E}^{\omega}=\hat{\underline{E}}^{\omega}(z)\exp(ikz)\qquad\text{Eq A3.4}$$

and we assume that its amplitude, $\hat{\underline{E}}^{\omega}$, will only vary on propagation, i.e. is only a function of z, then:

$$\nabla^2 \rightarrow \frac{\partial^2}{\partial z^2} \qquad \text{Eq A3.5}$$

If the envelope $\hat{\underline{E}}^{\omega}(z)$ varies much less rapidly than $\exp(ikz)$, then

$$\frac{\partial^2 \hat{\underline{E}}^{\omega}(z)}{\partial z^2} << 2ik\frac{\partial \hat{\underline{E}}^{\omega}(z)}{\partial z} \qquad \text{Eq A3.6}$$

Therefore, if we apply the approximations of Equations A3.4, A3.5 and A3.6 to Equation A3.3, we reduce it to a first order differential equation:

$$\boxed{\frac{\partial \hat{\underline{E}}^{\omega}(z)}{\partial z} = -\frac{\alpha}{2}\hat{\underline{E}}^{\omega}(z) + \frac{i\omega^2\mu_0}{2k}\underline{p}^{NL}(\omega)\exp(-ikz)} \qquad \text{Eq A3.7}$$

where α accounts for the material absorption associated with the conductivity, σ, of the medium:

$$\alpha = \frac{\omega\mu_0\sigma}{k} \qquad \text{Eq A3.8}$$

In Eq A3.7, k is the propagation constant of a plane wave propagating in a medium that extends to infinity in the transversal direction.

Equation A3.7 is relevant for any order of nonlinearity. However, in this Appendix, we are only interested in second order nonlinearities, where the interaction between two waves of frequency ω_1 and ω_2, produce a polarisation at the sum frequency $\omega_3 = \omega_1 + \omega_2$. In this case the nonlinear polarisation term is (see Appendix 4):

$$\underline{p}^{NL}(\omega_3) = \varepsilon_0\chi^{(2)}(\omega_1,\omega_2):\underline{E}^{\omega_1}\underline{E}^{\omega_2} \qquad \text{Eq A3.9}$$

Using the contracted d-tensor notation and Eq A3.4 for ω_1 and ω_2 we have

$$\underline{p}^{NL}(\omega_3) = 2\varepsilon_0 d(\omega_1,\omega_2):\hat{\underline{E}}^{\omega_1}\hat{\underline{E}}^{\omega_2}\exp\left[i(k_1+k_2)z\right] \qquad \text{Eq A3.10}$$

where,

$$d(\omega_1,\omega_2)=\frac{\chi^{(2)}(\omega_1,\omega_2)}{2} \qquad \text{Eq A3.11}$$

Then substituting Eq A3.10 into Eq A3.7, the progression of the EM wave at ω_3 is described by

$$\frac{\partial\hat{\underline{E}}(\omega_3)}{\partial z}=-\frac{\alpha_3}{2}\hat{\underline{E}}(\omega_3)+\frac{i\omega_3^2}{c^2k_3}d(\omega_1,\omega_2):\hat{\underline{E}}^{\omega_1}\hat{\underline{E}}^{\omega_2}\exp\left[i(k_1+k_2-k_3)z\right] \qquad \text{Eq A3.12}$$

However, the new electric field at ω_3, in combination with the field at ω_1 or ω_2, can produce fields at ω_2 or ω_1. Then,

$$\begin{cases}\dfrac{\partial\hat{\underline{E}}^{\omega_3}}{\partial z}=-\dfrac{\alpha_3}{2}\hat{\underline{E}}^{\omega_3}+\dfrac{i\omega_3^2}{c^2k_3}d(\omega_1,\omega_2):\hat{\underline{E}}^{\omega_1}\hat{\underline{E}}^{\omega_2}\exp(i\Delta kz)\\ \dfrac{\partial\hat{\underline{E}}^{\omega_1}}{\partial z}=-\dfrac{\alpha_1}{2}\hat{\underline{E}}^{\omega_1}+\dfrac{i\omega_1^2}{c^2k_1}d(\omega_3,-\omega_2):\hat{\underline{E}}^{\omega_3}\left(\hat{\underline{E}}^{\omega_2}\right)^*\exp(-i\Delta kz)\\ \dfrac{\partial\hat{\underline{E}}^{\omega_2}}{\partial z}=-\dfrac{\alpha_2}{2}\hat{\underline{E}}^{\omega_2}+\dfrac{i\omega_2^2}{c^2k_2}d(\omega_3,-\omega_1):\hat{\underline{E}}^{\omega_3}\left(\hat{\underline{E}}^{\omega_1}\right)^*\exp(-i\Delta kz)\end{cases} \qquad \text{Eq A3.13}$$

where

$$\Delta k=k_1+k_2-k_3. \qquad \text{Eq A3.14}$$

Note that $\hat{\underline{E}}^{-\omega_1}=\left(\hat{\underline{E}}^{\omega_1}\right)^*$

The set of coupled differential equations of Eq A3.13 can be rewritten by considering the following:

- Overall permutation symmetry $\Rightarrow d(\omega_3,-\omega_2)=d(\omega_3,-\omega_1)=d(\omega_1,\omega_2)=d$
- No conductivity $\Rightarrow \alpha_1=\alpha_2=\alpha_3=0$
- $d::\hat{\underline{E}}^{\omega_1}\hat{\underline{E}}^{\omega_2}=d_{eff}\hat{E}^{\omega_1}\hat{E}^{\omega_2}$ where $d_{eff}=d:\hat{\underline{e}}_1\hat{\underline{e}}_2$, $\hat{\underline{e}}_1$ and $\hat{\underline{e}}_2$ are unitary vectors in the direction of $\hat{\underline{E}}^{\omega_1}$ and $\hat{\underline{E}}^{\omega_2}$.

Then,

$$\begin{cases} \dfrac{\partial \hat{\underline{E}}^{\omega_3}}{\partial z} = \dfrac{i\omega_3}{cn_3} d_{eff} \hat{E}^{\omega_1} \hat{E}^{\omega_2} \exp(i\Delta kz) \\ \dfrac{\partial \hat{\underline{E}}^{\omega_1}}{\partial z} = \dfrac{i\omega_1}{cn_1} d_{eff} \hat{E}^{\omega_3} \left(\hat{E}^{\omega_2}\right)^* \exp(-i\Delta kz) \\ \dfrac{\partial \hat{\underline{E}}^{\omega_2}}{\partial z} = \dfrac{i\omega_2}{cn_2} d_{eff} \hat{E}^{\omega_3} \left(\hat{E}^{\omega_1}\right)^* \exp(-i\Delta kz) \end{cases} \qquad \text{Eq A3.15}$$

Where n_1, n_2 and n_3 are the effective indices of the propagating modes.

Appendix 4

Nonlinear polarisation terms.

The effect of the material in the electromagnetic (EM) radiation can be studied by considering that the incident EM field polarises the atoms in the material, thus creating a polarisation charge that modifies the incident field.

In free space, the electric field is related to the charges that produce it by

$$\nabla \underline{E} = \frac{\rho}{\varepsilon_0} \qquad \text{Eq A4.1}$$

where ρ is the charge density and ε_0 is the free space permittivity.

If we consider that the effect of the electric field is to polarise the atoms, then we create a polarisation charges, ρ_p, given by

$$\rho_p = -\nabla \underline{p} \qquad \text{Eq A4.2}$$

where $\underline{p}$ is the dipole momentum per unit volume.

Then, the total electric field in the medium depends on both the existing charge density, ρ, and the introduced polarisation charge, ρ_p.

$$\nabla \underline{E} = \frac{1}{\varepsilon_0}\left(\rho + \rho_p\right) = \frac{1}{\varepsilon_0}\left(\rho - \nabla \underline{p}\right) \quad \Rightarrow \quad \nabla\left(\varepsilon_0 \underline{E} + \underline{p}\right) = \rho \qquad \text{Eq A4.3}$$

The electric displacement, $\underline{D}$, is defined as

$$\underline{D} = \varepsilon_0 \underline{E} + \underline{p} \qquad \text{Eq A4.4}$$

This vector will account for the material properties .

In the linear case, when the incoming electric field is small, the contribution of the material to the total electric field is proportional to the incoming field, i.e.

$$\underline{p} \propto \underline{E}\ , \quad \underline{p} = \varepsilon_0 \chi \underline{E} \qquad \text{Eq A4.5}$$

then the electric displacement is

$$\underline{D} = \varepsilon_0 \underline{E} + \underline{p} = \varepsilon_0 (1+\chi)\underline{E} = \varepsilon_0 \varepsilon_r \underline{E} \qquad \varepsilon = \varepsilon_0 \varepsilon_r, \qquad \text{Eq A4.6}$$

The refractive index is related to the relative permittivity, ε_r, by:

$$n^2 = \varepsilon_r \qquad \text{Eq A4.7}$$

If the incoming electric field is large enough, the response of the material is not only proportional to the field, but also its square and higher powers. Therefore the polarisation and the displacement are proportional to the square and higher powers of the electric field.

$$\underline{p} = \varepsilon_0 \chi \underline{E} + \varepsilon_0 \chi^{(2)} \underline{E}^2 + \varepsilon_0 \chi^{(3)} \underline{E}^2 + \ldots \qquad \text{Eq A4.8}$$

χ is much larger than $\chi^{(2)}$, and $\chi^{(2)}$ is much larger than $\chi^{(3)}$. In this Appendix we will be interested in the quadratic nonlinear term, $\chi^{(2)}$. The interaction of light and matter thought $\chi^{(2)}$ is the second order nonlinear effect. In general χ, $\chi^{(2)}$, $\chi^{(3)}$ are tensors, to account for the material anisotropy.

In general for two incident optical fields at frequencies ω_1 and ω_2, the polarisation terms at $\omega_3 = \omega_1 + \omega_2$ are:

$$\begin{aligned} \underline{p}(\omega_3) &= \varepsilon_0 \chi(\omega_3)\underline{E}(\omega_3) + \varepsilon_0 \chi^{(2)}(\omega_1, \omega_2) : \underline{E}(\omega_1)\underline{E}(\omega_2) + \ldots \\ &= \underline{p}^{linear}(\omega_3) + \underline{p}^{NL}(\omega_3) + \ldots \end{aligned} \qquad \text{Eq A4.9}$$

where ":" stands for tensor multiplication. The polarisation terms at ω_1 and ω_1 are:

$$\underline{p}(\omega_1) = \varepsilon_0 \chi(\omega_1)\underline{E}(\omega_1) + \varepsilon_0 \chi^{(2)}(\omega_3, -\omega_2) : \underline{E}(\omega_3)\underline{E}(-\omega_2) + \ldots \qquad \text{Eq A4.10}$$

$$\underline{p}(\omega_2) = \varepsilon_0 \chi(\omega_2)\underline{E}(\omega_2) + \varepsilon_0 \chi^{(2)}(\omega_3, \omega_1) : \underline{E}(\omega_3)\underline{E}(-\omega_1) + \ldots \qquad \text{Eq A4.11}$$

Appendix 5

Use of the Runge-Kutta method to solve the coupled amplitude equations governing SHG.

The coupled differential equations governing SHG are

$$\begin{cases} \dfrac{\partial \hat{E}^{\omega}}{\partial z} = \dfrac{i\omega}{2cn_{\omega}} d_{eff}(2\omega,-\omega)\hat{E}^{2\omega}\left(\hat{E}^{\omega}\right)^{*}\exp(-i\Delta kz) \\ \dfrac{\partial \hat{E}^{2\omega}}{\partial z} = \dfrac{i\omega}{cn_{2\omega}} d_{eff}(\omega,\omega)\left(\hat{E}^{\omega}\right)^{2}\exp(i\Delta kz) \end{cases} \qquad \text{Eq A5.1}$$

$$\Delta k = 2k_{\omega} - k_{2\omega} = \frac{4\pi}{\lambda_{\omega}}\left(n_{\omega} - n_{2\omega}\right)$$

$$d_{eff}(2\omega,-\omega) = 2d_{eff}(\omega,\omega) \qquad \text{Eq A5.2}$$

This is an initial value problem where we propagate a solution over an interval. By far the most often used method of solving these equations is by the fourth-order Runge-Kutta method. For a first order differential equation

$$\frac{dy(x)}{dx} = f(x,y) \qquad \text{Eq A5.3}$$

the fourth-order Runge-Kutta formulas are as follows:

$$y_{n+1} = y_n + \frac{k_1}{6} + \frac{k_2}{3} + \frac{k_3}{3} + \frac{k_4}{6} + O\left(h^5\right) \qquad \text{Eq A5.4}$$

where

$$\begin{aligned} k_1 &= hf\left(x_n, y_n\right) \\ k_2 &= hf\left(x_n + \frac{h}{2}, y_n + \frac{k_1}{2}\right) \\ k_3 &= hf\left(x_n + \frac{h}{2}, y_n + \frac{k_2}{2}\right) \\ k_4 &= hf\left(x_n + h, y_n + k_3\right) \end{aligned} \qquad \text{Eq A5.5}$$

As can be seen, the solution at x(t+h) is obtained at the expense of evaluating the function f four times. The final formula agrees with the Taylor expansion up to, and including, the terms in h^4. The error therefore contains h^5 but no lower powers of h. Without knowing the coefficient of h^5 in the error, it is difficult to be precise about the local truncation error (i.e. the error due to the truncation of the Taylor series), in this situation we say that the local truncation error is "of the order of h^5 ", abbreviated by $O(h^5)$.

Other errors are due to the accumulative effects of all local truncation errors, and the round-off error.

In general higher order methods (a method is conventionally nth order if its error term is $O(h^{n+1})$) are more accurate in the problems that contemporary scientists like to solve, but this is not always true.

Then using the fourth order Runge-Kutta method we have that the electric field for the fundamental and second harmonic are

$$E_{n+1}^{\omega} = E_n^{\omega} + \frac{k_1^{\omega}}{6} + \frac{k_2^{\omega}}{3} + \frac{k_3^{\omega}}{3} + \frac{k_4^{\omega}}{6} + O(h^5)$$
$$E_{n+1}^{2\omega} = E_n^{2\omega} + \frac{k_1^{2\omega}}{6} + \frac{k_2^{2\omega}}{3} + \frac{k_3^{2\omega}}{3} + \frac{k_4^{2\omega}}{6} + O(h^5) \qquad \text{Eq A5.6}$$

where

$$k_1^{\omega} = hf^{\omega}\left(z_n, E_n^{\omega}, E_n^{2\omega}\right)$$
$$k_2^{\omega} = hf^{\omega}\left(z_n + \frac{h}{2}, E_n^{\omega} + \frac{k_1^{\omega}}{2}, E_n^{2\omega} + \frac{k_1^{2\omega}}{2}\right)$$
$$k_3^{\omega} = hf^{\omega}\left(z_n + \frac{h}{2}, E_n^{\omega} + \frac{k_2^{\omega}}{2}, E_n^{2\omega} + \frac{k_2^{2\omega}}{2}\right)$$
$$k_4^{\omega} = hf^{\omega}\left(z_n + h, E_n^{\omega} + k_3^{\omega}, E_n^{2\omega} + k_3^{2\omega}\right) \qquad \text{Eq A5.7}$$
$$f^{\omega}\left(z, E^{\omega}, E^{2\omega}\right) = \frac{\partial E^{\omega}}{\partial z}$$

$$
\begin{aligned}
k_1^{2\omega} &= hf^{2\omega}\left(z_n, E_n^{\omega}, E_n^{2\omega}\right) \\
k_2^{2\omega} &= hf^{2\omega}\left(z_n + \frac{h}{2}, E_n^{\omega} + \frac{k_1^{\omega}}{2}, E_n^{2\omega} + \frac{k_1^{2\omega}}{2}\right) \\
k_3^{2\omega} &= hf^{2\omega}\left(z_n + \frac{h}{2}, E_n^{\omega} + \frac{k_2^{\omega}}{2}, E_n^{2\omega} + \frac{k_2^{2\omega}}{2}\right) \\
k_4^{2\omega} &= hf^{2\omega}\left(z_n + h, E_n^{\omega} + k_3^{\omega}, E_n^{2\omega} + k_3^{2\omega}\right) \\
f^{2\omega}\left(z, E^{\omega}, E^{2\omega}\right) &= \frac{\partial E^{2\omega}}{\partial z}
\end{aligned}
\qquad \text{Eq A5.8}
$$

Appendix 6.

Conditions for up-conversion and down-conversion.

Here we present a new method to determine the conditions for up-conversion and down-conversion.

The variation of the second harmonic electric field with propagation is given by

$$\frac{\partial \underline{\hat{E}}^{2\omega}}{\partial z} = \frac{i\omega}{cn_{2\omega}} d_{eff}(\omega,\omega)\left(\hat{E}^{\omega}\right)^2 \exp(i\Delta kz) \qquad \text{Eq. A6.1}$$

Using Eulers formula for the first order:

$$\text{if} \quad E' = f(z, E(z)) \quad \Rightarrow E(z+h) = E(z) + hE'(z) \qquad \text{Eq. A6.2}$$

Eq 1 becomes:

$$\underline{\hat{E}}^{2\omega}(z+h) = \underline{\hat{E}}^{2\omega}(z) + h\frac{i\omega}{cn_{2\omega}} d_{eff}(\omega,\omega)\left(\hat{E}^{\omega}\right)^2 \exp(i\Delta kz) \qquad \text{Eq. A6.3}$$

Up-conversion takes place if:

$$\left|\underline{\hat{E}}^{2\omega}(z+h)\right| > \left|\underline{\hat{E}}^{2\omega}(z)\right| \qquad \text{Eq. A6.4}$$

and down conversion takes place if:

$$\left|\underline{\hat{E}}^{2\omega}(z+h)\right| < \left|\underline{\hat{E}}^{2\omega}(z)\right| \qquad \text{Eq. A6.5}$$

To obtain the phase condition for up-conversion and down-conversion, we express the electric field for the harmonic and second harmonics in terms of its amplitude and phase:

$$\begin{aligned} \underline{\hat{E}}^{2\omega}(z+h) &= \left|\underline{\hat{E}}^{2\omega}\right| \exp\left(i\alpha^{2\omega}\right) \\ \underline{\hat{E}}^{\omega}(z) &= \left|\underline{\hat{E}}^{\omega}\right| \exp\left(i\alpha^{\omega}\right) \end{aligned} \qquad \text{Eq. A6.6}$$

Then using Eq A6.6 in Eq A6.3 we obtain:

$$\left|\hat{\underline{E}}^{2\omega}(z+h)\right|\exp\left(i\alpha^{2\omega}+k^{2\omega}h\right)=\left|\hat{\underline{E}}^{2\omega}(z)\right|\exp\left(i\alpha^{2\omega}\right)+h\frac{\omega}{cn_{2\omega}}d_{eff}(\omega,\omega)\left|\hat{E}^{\omega}\right|^{2}\exp\left(i\frac{\pi}{2}+i2\alpha^{\omega}+i\Delta kz\right)$$

Eq. A6.7

For the two terms in the right hand side of Eq. A6.7 to add constructively their phase difference needs to be smaller than $\pi/2$, In this situation, the condition of Eq A6.4 is fulfilled, and up-conversion takes place. The phase difference in the terms in the right hand side of Eq. A6.7 is:

$$\left(\alpha^{2\omega}\right)-\left(\frac{\pi}{2}+2\alpha^{\omega}+\Delta kz\right) \qquad \text{Eq A6.8}$$

Then the condition for up-conversion is:

$$\left|\alpha^{2\omega}-\left(\frac{\pi}{2}+2\alpha^{\omega}+\Delta kz\right)\right|<\frac{\pi}{2} \qquad \text{Eq A6.9}$$

Using the same argument the condition for down-conversion is:

$$\left|\alpha^{2\omega}-\left(\frac{\pi}{2}+2\alpha^{\omega}+\Delta kz\right)\right|>\frac{\pi}{2} \qquad \text{Eq A6.10}$$

And the condition for neither up-conversion or down-conversion is:

$$\left|\alpha^{2\omega}-\left(\frac{\pi}{2}+2\alpha^{\omega}+\Delta kz\right)\right|=\frac{\pi}{2} \qquad \text{Eq A6.11}$$

At phase matching we have:

$$\left|\alpha^{2\omega}-\left(\frac{\pi}{2}+2\alpha^{\omega}+\Delta kz\right)\right|=0 \qquad \text{Eq A6.12}$$

Appendix 7

Internal normalised conversion efficiency and effective area.

The coupled differential equations governing SHG are:

$$\begin{cases} \dfrac{\partial \hat{\underline{E}}^{\omega}}{\partial z} = \dfrac{i\omega}{2cn_{\omega}} d_{eff}(2\omega,-\omega)\hat{E}^{2\omega}\left(\hat{E}^{\omega}\right)^{*}\exp(-i\Delta kz) \\ \dfrac{\partial \hat{\underline{E}}^{2\omega}}{\partial z} = \dfrac{i\omega}{cn_{2\omega}} d_{eff}(\omega,\omega)\left(\hat{E}^{\omega}\right)^{2}\exp(i\Delta kz) \end{cases} \qquad \text{Eq A7.1}$$

$$\Delta k = 2k_{\omega} - k_{2\omega} = \frac{4\pi}{\lambda_{\omega}}(n_{\omega} - n_{2\omega})$$

Let us assume that initially there is no light at the second harmonic (SH) frequency. Lets us also examine the case of low conversion efficiency such that any depletion of the fundamental frequency can be neglected, i.e.

$$\frac{\partial \hat{\underline{E}}^{\omega}}{\partial z} = 0 \qquad \text{Eq A7.2}$$

This simplification allows just one of the differential equations to be studied instead of the complete set. Hence, the evolution of the light at the SH frequency is given by:

$$\frac{\partial \hat{\underline{E}}^{2\omega}}{\partial z} = \frac{i\omega}{cn_{2\omega}} d_{eff}(\omega,\omega)\left(\hat{E}^{\omega}\right)^{2}\exp(i\Delta kz) \qquad \text{Eq A7.3}$$

Since $\hat{\underline{E}}^{\omega}$ is treated as constant (low conversion efficiency), this can be easily integrated along the length of the crystal to give

$$\begin{aligned} \hat{\underline{E}}^{2\omega}(L) &= \frac{\omega d_{eff}}{cn_{2\omega}}\left(\hat{E}^{\omega}\right)^{2}\frac{\left(e^{i\Delta kL}-1\right)}{\Delta k} \\ &= \frac{\omega d_{eff} L}{cn_{2\omega}}\left(\hat{E}^{\omega}\right)^{2} e^{i\Delta kL/2}\sin c\frac{\Delta kL}{2} \end{aligned} \qquad \text{Eq A7.4}$$

Now, the electric field can be written in terms of the irradiance,

$$I^{\omega} = \frac{\varepsilon_o c n(\omega)}{2} \left| E^{\omega} \right|^2 \qquad \text{Eq A7.5}$$

$$I^{2\omega}(L) = \frac{2\omega^2 d_{eff}^2}{\varepsilon_o c^3 n_{\omega}^2 n_{2\omega}} I^2 \left(I^{\omega} \right)^2 \sin c^2 \frac{\Delta k L}{2} \qquad \text{Eq A7.6}$$

and the intensity in terms of the power

$$I^{w} = \frac{P^{\omega}}{Area} \qquad \text{Eq A7.7}$$

Where "Area" is the effective area.

At the phase matching condition ($\Delta k = 0$), we obtain

$$\frac{P_{2\omega}}{P_{\omega}} = \frac{8\pi^2 d_{eff}^2}{\varepsilon_o c n_{\omega}^2 n_{2\omega} \lambda_{\omega}^2} L^2 \frac{P_{\omega}}{Area} \qquad \text{Eq A7.8}$$

where

$$\omega = \frac{2\pi c}{\lambda} \qquad \text{Eq A7.9}$$

Then, the effective area is:

$$Area = \frac{8\pi^2 d_{eff}^2}{\varepsilon_o c n_{\omega}^2 n_{2\omega} \lambda_{\omega}^2} L^2 \frac{P_{\omega}^2}{P_{2\omega}} \qquad \text{Eq A7.10}$$

The internal normalised conversion efficiency, η_o, defining as

$$P_{2\omega} = \eta_o P_{\omega}^2 L^2 \qquad \text{Eq A7.11}$$

is given by

$$\eta_o = \frac{8\pi^2 d_{eff}^2}{\varepsilon_o c n_{\omega}^2 n_{2\omega} \lambda_{\omega}^2} \frac{1}{Area} \qquad \text{Eq A7.12}$$

Appendix 8.

Spatial chirping of wavevector mismatch in $LiNbO_3$ segmented waveguides for engineering of specific second-harmonic generation detuning curves for cascading applications.

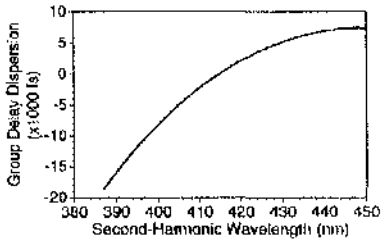

CTuJ1 Fig. 3. Predicted group delay dispersion versus second-harmonic wavelength for the ultrashort APM device.

mechanics of the design permit some prisms to be translated across the beam to adjust the temporal dispersion of both the fundamental input and the second-harmonic output. Figure 3 shows the predicted group delay dispersion for one set of prism positions. A fundamental pulse as short as 40 fs can generate a 40-fs second-harmonic pulse with this device, limited by third order temporal dispersion (TOD), not by conversion bandwidth. Also, the sign of the residual TOD is opposite that normally accumulated by propagation through optical elements, so that our ultrashort APM device could be used to compensate TOD in the other optics of an experimental application.

CVI Laser Inc., 361 Lindbergh Ave., Livermore, California 94550-9291

1. B.A. Richman, S.E. Bisson, R. Trebino, M.G. Mitchell, E. Sidick, A. Jacobson, Opt. Lett. 22, 1223–1225 (1997).

CTuJ2 **10:45 am**

Spatial chirping of wavevector mismatch in $LiNbO_3$ segmented waveguides for engineering of specific second-harmonic generation detuning curves for cascading applications

Carlos G. Treviño-Palacios, Daniel Ortega,* George I. Stegeman, J. Stewart Aitchison,*
Center for Research and Education in Optics and Lasers, University of Central Florida, P.O. Box 162700 Orlando, Florida 32826-2700;
E-mail: carlost@mail.creol.ucf.edu

A new aspect of second-order nonlinearities, namely the generation of large nonlinear phase shifts from cascading, has prompted a great deal of interest. To date high throughput all-optical switching using cascaded second-order nonlinearities has been experimentally demonstrated in temperature-tuned waveguide second-harmonic generation (SHG).[1] The success of these devices is based on the spatial nonuniform wavevector distribution and the unique nonlinear phase shift introduced by the temperature tuning method used for phase matching. In SHG, the fundamental and second-harmonic fields require some joint propagation and a specific wavevector mismatch distribution, which controls the local details of the energy exchange. With the development of quasi-phase-matching (QPM) techniques it is now possible to achieve the required, flexible, grating-assisted phase matching at almost any wavelength by spatial

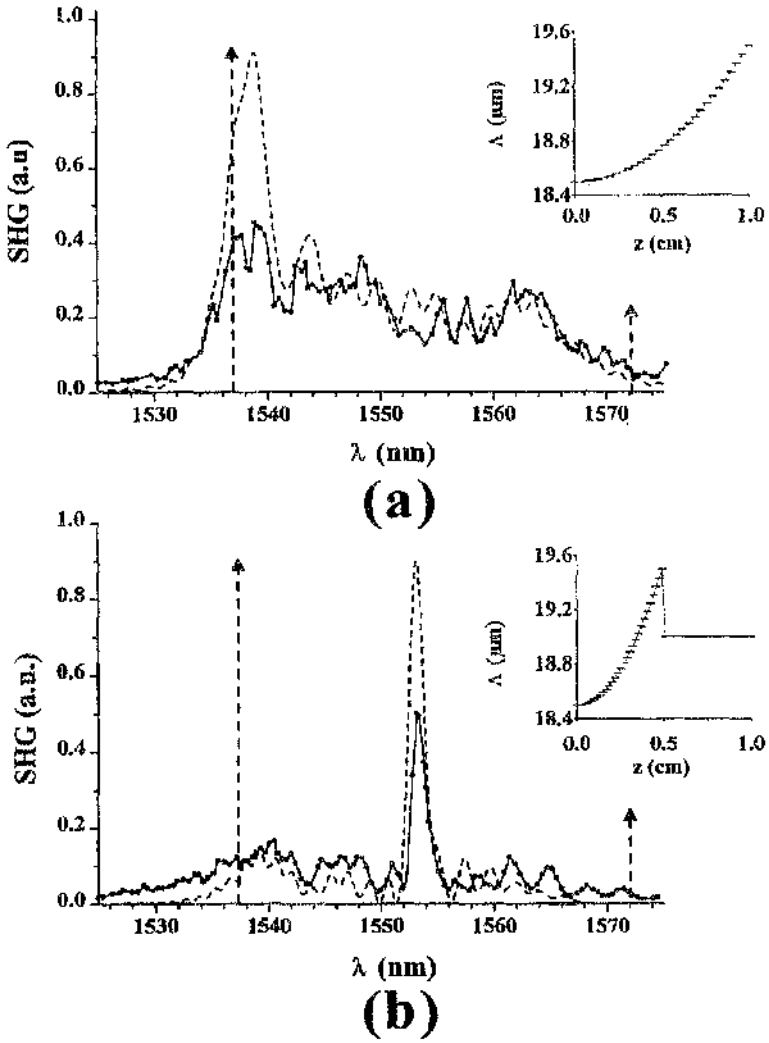

CTuJ2 Fig. 1. Typical SHG wavelength scans in a $LiNbO_3$ segmented waveguide with two different nonuniform chirped gratings (inserts). (a) Quadratic chirp and (b) quadratic chirp followed by a uniform grating. Dotted lines show the numerical simulation with the same parameters as the experimental ones. Phase-matching at the extreme values of the grating periods (18.5 and 19.5 μm) are shown with arrows at λ = 1537 and 1572 nm, respectively.

control of the grating period. Spatially varying (along the propagation path) the grating period now allows an all-optical switch using cascaded second-order nonlinearities to be implemented at room temperature.

We investigated the low depletion SHG response of an engineered, nonuniform wavevector distribution along the propagation axis. The specific variation in the wavevector mismatch was achieved by a nonuniform chirp (i.e., not a linear chirp) in the grating period of a $LiNbO_3$ segmented waveguide. The required chirp was synthesized by first calculating the smoothly varying wavevector mismatch needed to have the desired response function. As shown in Fig. 1 (inset), the distribution was discretized into different sections whose period was chosen to give the average mismatch for each section. A mask was then fabricated with a few (5–10) uniform segments making up each section to obtain a step-wise change in the grating period. The chirp was selected to be a combination of a quadratically chirped gratings and uniform gratings. Segmented waveguides were then fabricated by titanium indiffusion with the engineered mask design. Uniform (not chirped) waveguides with QPM periods in the 18.5–19.5 μm region were also fabricated and their SHG response measured for comparison. They had bandwidths of ~1.3 nm and conversion efficiencies of 1.5% with a 100-W pump.

Representative low depletion SHG tuning curves for these waveguides are shown in Fig. 1 for two different wavevector distribution (inserts). A synchronously pumped mode-locked color-center laser used for scanning the fundamental wavelength. For comparison, a numerical simulation with the same parameters as the experimental ones are shown as dotted lines. We observed a broadening in the bandwidth of the SHG detuning curve relative to the uniform grating case and a complicated dependence of SHG on wavelength. Additionally, all the wave-vector distributions studied exhibited some amount of nonreciprocity. As shown previously, this is a direct consequence of using simultaneously a nonuniform and nonsymmetrical wave-vector distribution.[2]

Some important applications of controlling the SHG evolution with an arbitrary, nonuniformly chirped grating are for all-optical switching devices at room temperature based on cascading, new ways of enhancing the SHG bandwidth, etc.

Department of Electronic and Electrical Engineering, University of Glasgow, Glasgow G12 8QQ United Kingdom

1. Y. Baek, R. Schiek, G.I. Stegeman, G. Krijnen, I. Baumann, W. Sohler, Appl. Phys. Lett. **68**, 2055 (1996).
2. C.G. Treviño-Palacios, G.I. Stegeman, P. Baldi, Opt. Lett. **21**, 1442 (1996).

CTuJ3 11:00 am

Portable difference-frequency IR-spectrometer for detection of CO and other trace gases

T. Kelz, D. Rehle, H.-D. Kronfeldt, B. Sumpf,* *Optisches Institut der Technischen Universität Berlin, Sekr. PN 0-1, Hardenbergstr. 36, 10623 Berlin, Germany; E-mail: kf@mail.physik.tu-berlin.de*

Portable difference-frequency IR-spectrometers consisting of an electronic module, an infrared module, and a spectroscopic or detection module have been set up for the mid-infrared region around 4.7 μm and 7.2 μm (Fig. 1). For the 4.7-μm region single-mode diode lasers (SDL 5421-G1, 806 nm, 20 mW optical output power; TOLD 9150 (S), 690 nm, 6 mW) are used as pump sources. Applying noncritical phase-matching type I (90°) in a $AgGaS_2$ crystal of dimensions 40 × 4 × 4 mm^3 as nonlinear medium a narrow bandwidth infrared light source with sufficient power for spectroscopic use has been constructed. An infrared output power of more

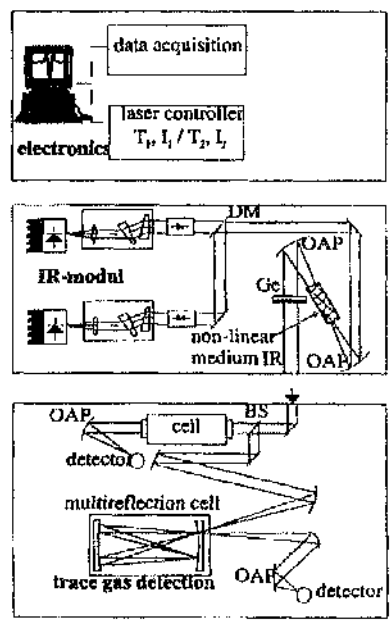

CTuJ3 Fig. 1. Setup of the portable difference frequency IR-spectrometer.

List of Publications.

- T, Piorek, J M Fatah, R G Roberts, D Ortega, A A Chesworth, P Parrison, T Stirner, W E Hagston, "Montecarlo simulation of carrier transport and relaxation in surperlattices", Superlattices and microstructures, 15, pp 209--212, (1994).

- D. Ortega, R M De La Rue, and J S Aitchison, "Cut-off wavelength of periodically segmented waveguides in Ti:$LiNbO_3$", Journal of Lightwave Technology, 16, pp. 284--191, (1998).

- D. Ortega, R M De La Rue, and J S Aitchison, "Cut-off wavelength of periodically segmented waveguides" Paper, proc. CLEO'97, Baltimore, 1997.

- D. Ortega, J M Aldariz, J M Arnold and J S Aitchison, "Quasi-modes of periodically segmented waveguides", Proc. QE 13, Cardiff, 1997.

- D. Ortega, J M Aldariz and J S Aitchison, "Mode engineering in periodically segmented waveguides", Proc. Integrated Photonics Research'98, Victoria, 1998.

- Carlos G. Trevino-Palacios, Daniel Ortega, George I Stegeman, and J. Stewart Aitchison, "Spatial Chirp of Wavevector-Mismatch in $LiNbO_3$ segmented waveguides for Engineering of Specific Second Harmonic Generation Detuning Curves for Cascading Applications", Paper, proc. CLEO'98, San Francisco, 1998.

- J Ruano, D Ortega, J R Bonar, J M Cooper, J S Aitchison, "Integrated waveguide sensors for a Biological Assays", Paper, proc. CLEO/Europe'98, Glasgow, 1998.

- Daniel Ortega, Jose M Aldariz, J. M. Arnold, and J. Stewart Aitchison, "Analysis of "Quasi-modes" in Periodic Segmented Waveguides", Journal of Lightwave technology.

- J.M.Ruano, D.Ortega, J.R. Bonar, A.J.McLaughlin, M.G.Jubber, J.M.Cooper and J.S. Aitchison, "Fabrication of Deep Holes and Channels for Biological Assays in Flame Hydrolysis Deposited Glass", Paper, proc. MNE 98, Leuven (Belgium), 1998.